Characteristics of the kinematics and geomorphology of slow-moving landslides in the Colca valley, South-Peru

R.A. Heijenk, 3471810

Utrecht University, Faculty of Geosciences, Department of Physical Geography
Université Joseph Fourier, ISTerre

Utrecht University

ISTerre
Institut des Sciences de la Terre

First supervisor: Pascual Lacroix, Université Joseph Fourier, ISTerre
Second supervisor: Denis Jongmans, Université Joseph Fourier, ISTerre
Third supervisor: Steven de Jong, Utrecht University

Abstract

Slow-moving landslides cause large amounts of damage in mountainous regions and are known to be reactivated by seasonal rainfall and seismicity, although the mechanics of reactivation associated with these 2 forcing factors is still debated. In this case study, the kinematics and geomorphology are constrained and related to possible forcing factors for a number of remote slow-moving landslides in the Colca valley (Peru), which threaten local villages and roads. To do so, the horizontal displacement of the landslides has been studied with a well-tested methodology that combines spaceborne stereo-photogrammetry, orthorectification, and sub-pixel image correlation of satellite images. A dataset of images acquired the Pléiades satellites have been used for their stereo-imagery and high resolution (0.7 m) and was complemented by one image of the SPOT6 satellite to improve temporal resolution. From this, three Digital Terrain Models (DTM) have been produced of which the quality has been determined by comparison with GPS and with the DTMs among each other, resulting in an accuracy of ±70 cm. Subsequently, ten horizontal displacement maps have been assessed by comparing with a permanent GPS installed on one of the landslides and by determining the values of a stable area, resulting in displacements with an error margin of 5-18 cm and 16-29 cm for correlation between Pléiades images and Pléiades-SPOT6 images respectively. Horizontal displacements of 1-3 meters in a period of thirteen months were constrained for the seven landslides that were identified from the displacement maps. An increase in displacement values towards the toe of the landslides suggests thinning of the landslide towards the toe or removal of material by the river. The major forcing factor for all landslides is seasonal rainfall, although two different responses have been recognized: 1) displacement due to high seasonal rainfall and 2) displacement due to both high and low seasonal rainfall. Two possible solutions can be suggested: I) sensitivity to rainfall is increased due to earthquake-related damaging on the nearest landslides so that rainwater infiltrates more easily, and II) lithological differences due to the paleo-sedimentary environment cause a higher sensitivity to rainfall in landslides containing finer material.

Contents

1. Introduction

A landslide is the movement of rock, debris or earth down a slope (Cruden 1991). In mountainous environments they pose a major threat, with over 30.000 victims in 2620 landslides triggered by rainfall and an additional 50.000 victims in landslides triggered by earthquakes that have been recorded between 2004 and 2010 (Petley, 2012). Also economic loss due to landslides, mostly as damage to infrastructure and property, is significant.

Slow-moving landslides cause large amounts of damage, while there is little knowledge of the controls on their kinematics and geomorphology. Their mechanics have been proven analogous to the behavior of creeping tectonic faults (Lacroix et al., 2014). Therefore the studying of these landslides can result in new perspectives for both landslides and active faults.

The monitoring of spatial displacement of slow moving landslides is essential for the understanding of kinematics and geomorphological processes, from which forcing factors can be deduced to make a hazard assessment. Generally known mechanics that act upon slow-moving landslides are increasing pore-pressure that is driven by seasonal rainfall (Handwerger et al., 2013; Iverson and Major, 1987). The factors that can force pore-pressure and cause displacements in landslides are e.g.: atmospheric tides that drive air pressure (Schulz et al., 2009), earthquakes (Lacroix et al., 2014) that accelerate landslide displacement, and human activity that can modify stresses by local loading or by buttress removal.

An excellent area to study slow-moving landslides is the Colca valley in southern Peru, where erosion of unconsolidated lacustrine and proluvial sediments have triggered several slow-moving landslides (Zavala et al., 2012). The best known landslide here is the Maca landslide, named for its proximity to the village of Maca, which now threatens to destroy a major touristic road, the village itself, and several irrigation channels (Zavala et al., 2012, Falconi et al., 2013). This landslide has an area of approximately 1 km^2 and a mean slope of approximately 9°. The velocities measured are ± 1 to 7 cm/year (Zerathe et al., in review). Forcing factors that are already known to act upon this landslide are seasonal rainfall and seismicitiy (Lacroix et al., 2014).

Spatial landslide displacement patterns, which are variable over a surface, are notoriously hard to acquire, as surface data are usually limited to point measurements with narrow time windows. With this and the difficulty in accessibility in mind, the easiest method is using remote sensing, which allows large areas to be monitored several times per year. Two main instruments are available for measuring displacements: Interferometric Synthetic Aperture Radar (InSAR) and the optical satellite imagery, for which the Pléiades satellites are excellent candidates with stereo-view and a 0.7 m resolution.

The advantages of InSAR are its ability to penetrate cloud cover and its independence of daylight. However, it can measure only small velocities on a centimeter scale due to the small wavelength (Fruneau et al., 1996) and at a given site an average of 15 differential interferograms per year have been used (Schmidt and Bürgmann, 2003). Another disadvantage is the dependency on slope direction and steepness along with the SAR incident angle and look direction, which can cause either radar shadow or layover. In contrast, Pléiades satellites can pick up large velocities on a scale of meters and there are no problems related to looking angle and slope steepness (Stumpf et al., 2014). Previous studies show that

displacement of more than 14 cm can be detected (Stumpf et al., 2014). However, they only acquire data during the day and when the atmosphere is clear from clouds.

Four Pléiades acquisitions over thirteen months have been acquired for the Maca site, of which three are stereo-images. An additional image from the SPOT6 satellite is available to provide a better spread of the data, which has a resolution twice that of the Pléiades image (1.5 m versus 0.7 m).

Correlations of subsequent Pléiades images were made to measure displacement, using the software COSI-CORR (Leprince et al., 2007) which is a method that has been applied successfully on landslides (Lacroix et al., 2014; Stumpf, 2014). Correlations with the SPOT6 image was made as well.

The main objective of this research is to characterize the landslides in the Colca valley in terms of kinematics and geomorphology and to reach conclusions on the forcing factors that act on each landslide. Secondary objectives are to quantify the accuracy of the Pléiades sensor to detect displacement in the 3 spatial directions.

Before correlating the images, all errors that are inherent within photography and imagery must be removed (Poli and Toutin, 2012). The satellite imagery were orthorectified as precisely as possible. To be more specific, the uncertainties of the orthoimages need to be smaller than the displacement of the surface for the measured movement to be significant (Leprince et al., 2007). Accurate orthorectification was realized by applying Digital Terrain Models (DTMs) and Ground Control Points (GCPs) that were as accurate as possible on the raw imagery.

The main results are maps with one to thirteen months of displacement and three DTMs. The characterizing aspects of the geomorphology were determined using the DTM of March 2013 and its derivatives. The shape of landslides is determined with the DTM and cross-sections were made to look at the displacement field in comparison with the elevation of each landslide. The kinematics were characterized using the temporal and spatial pattern of displacement of each landslide by considering both the displacement field and the displacement of a point on the landslide. The displacement of each landslide was compared with both cumulative rainfall and earthquake events.

In this research the correlation of Pléiades images was found to be a suitable method to constrain displacement rates. Even more, the displacement history combined with rainfall data clearly suggest seasonal forcing. Some landslides however evade the general trend, possibly due to another forcing factor such as lithological differences or seismic influence.

This document will first give a geological history on the Maca landslide. The methods that have been used to correlate the images and evaluate the quality of the displacement rates are discussed. Then the results of computation of horizontal displacement will be provided and the correlation with potential triggering factors will be discussed. Finally the quality of the results and the forcing factors will be discussed.

2. Site of Study

The Colca valley, Peru, lies in an area dominated by active volcanoes, such as the Bombaya, Hualca Hualca, and Mismi volcanoes, and deeply incised valleys with elevation differences of 3700 m (Figure 1). This area is part of the Western Cordillera, which lies in the Central Volcanic Zone of South America. The Central Volcanic zone has formed due to subduction of the Nazca plate under Western South America. Several sources of seismicity are present (Figure 2); earthquakes due to the subduction (up to M_w 9.0), due to regional tectonic faults (up to M_w 6.5), and due to activity of the nearby Hualca-Hualca volcano (up to M_w 3.0).

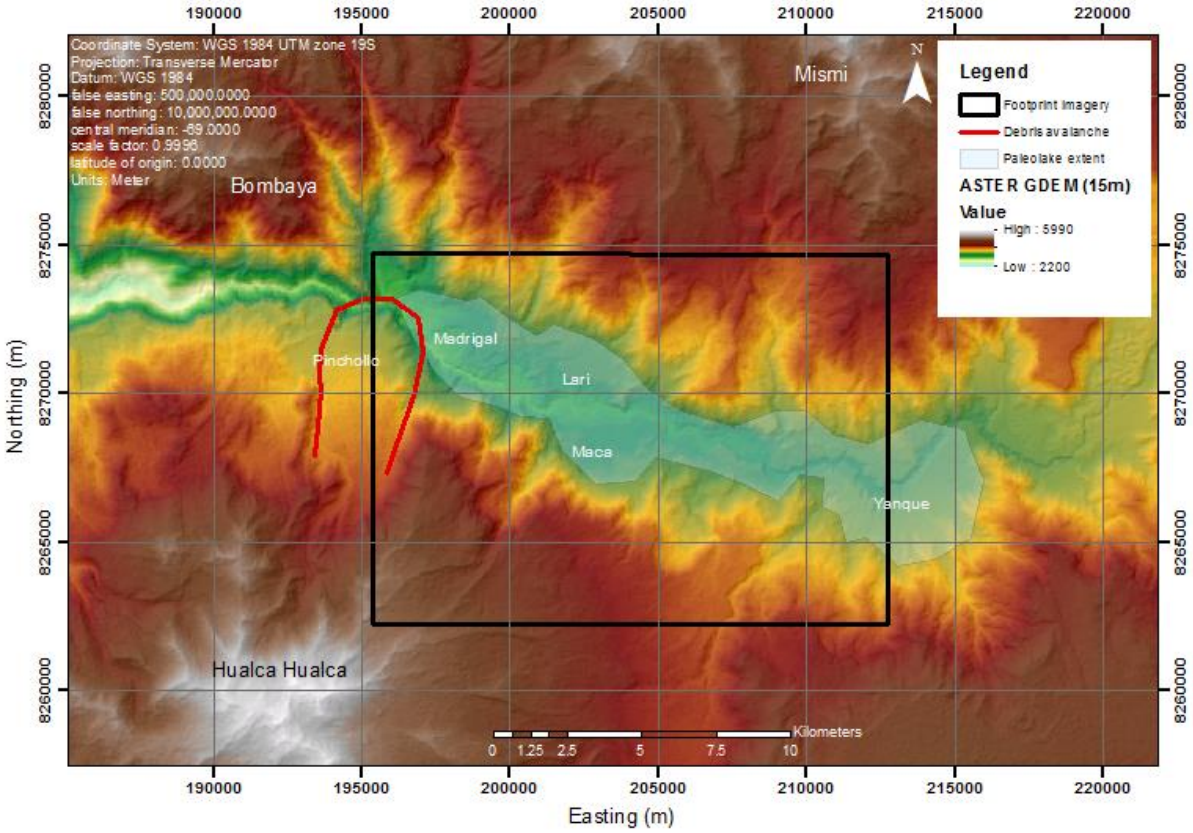

Figure 1: The Colca valley (black outline) with three stratovolcanoes (Hualca Hualca, Mismi and Bombaya) surrounding it. Ancient debris avalanche outlined in red, forming a dam for the blue extent of the paleolake.

The incision by the Colca river created one of the deepest canyons of the Andes, together with the Cotahuasi and Ocoña river canyons (Thouret et al. 2007). The geology of the site is characterized by a sequence of volcanic, lacustrine, and alluvial deposits. At the base of the succession lie ignimbrites, which have been deposited by volcanoes between ~25 and ~13 Ma (Thouret et al. 2007).

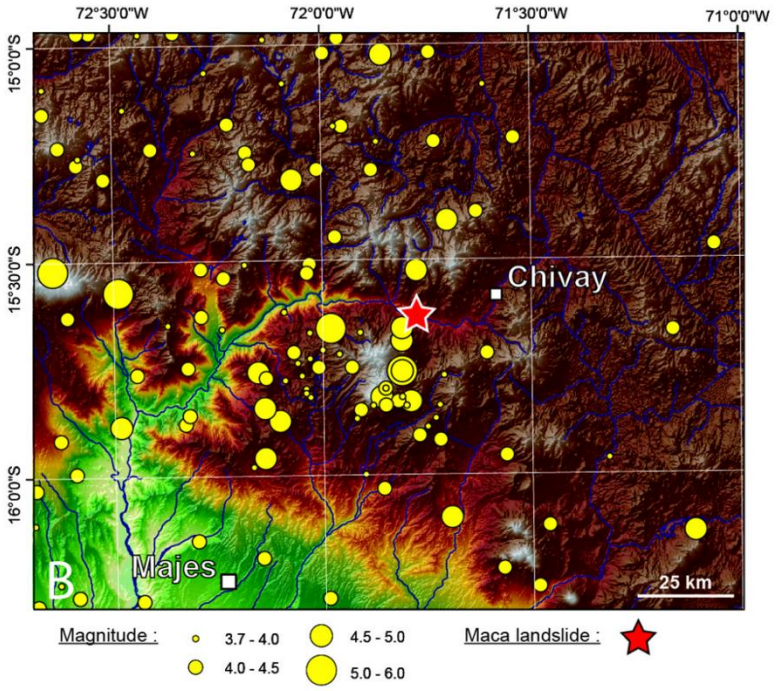

Figure 2: Seismicity in the region of the Colca valley.

Incision of the Rio Colca probably started ~9 Ma, but this is not well constrained due to a cover of 6-4 Ma-old lava flows (Thouret et al. 2007). More recent incision history has a better documentation. The first incision phase occurred before 1.06 Ma (Thouret et al. 2007), after which at least one large debris avalanche occurred near the town of Pinchollo (Figure 1) due to the collapse of the northern flank of the Hualca Hualca volcano. The avalanche deposits may have reached as far as the village of Madrigal. The deposits of the debris avalanche dammed the valley near Pinchollo and caused the formation of a paleolake, with a length of 25 km until the town of Yanque (Figure 1). In the paleolake lacustrine sediments have been deposited until 0.61 Ma (Thouret et al. 2007), resulting in a thickness of approximately 200 m. The sediments have formed a more or less flat valley floor, which has been incised by the river Colca, which is the origin of the landslides in the valley. At Maca, a small debris avalanche has been deposited on top of the lacustrine sediments (thickness of ~30m, Zerathe et al., in prep).

The lacustrine and proluvial material that forms the valley floor has remained unconsolidated until the present. Together with the incision of the Rio Colca and the shallow groundwater that causes ponds and wetlands in the area, the lacustrine material has become incompetent of supporting weight (Zavala et al. 2012). In recent history, villages have been built on the terraces next to the river, such as the village of Maca and Lari on both sides of the river (Figure 3). Fifty years ago a landslide occurred near the town of Lari, which has pushed the river towards the side of Maca (Figure 3) (Zavala et al. 2012). This increased the erosion rate at the toe of Maca and reduced the factor of safety of the slope. A busy touristic road crosses the scarps of the landslide (Figure 3), which has been damaged by the landsliding. The village of Maca is situated right next to the headscarp and is threatened (Figure 3).

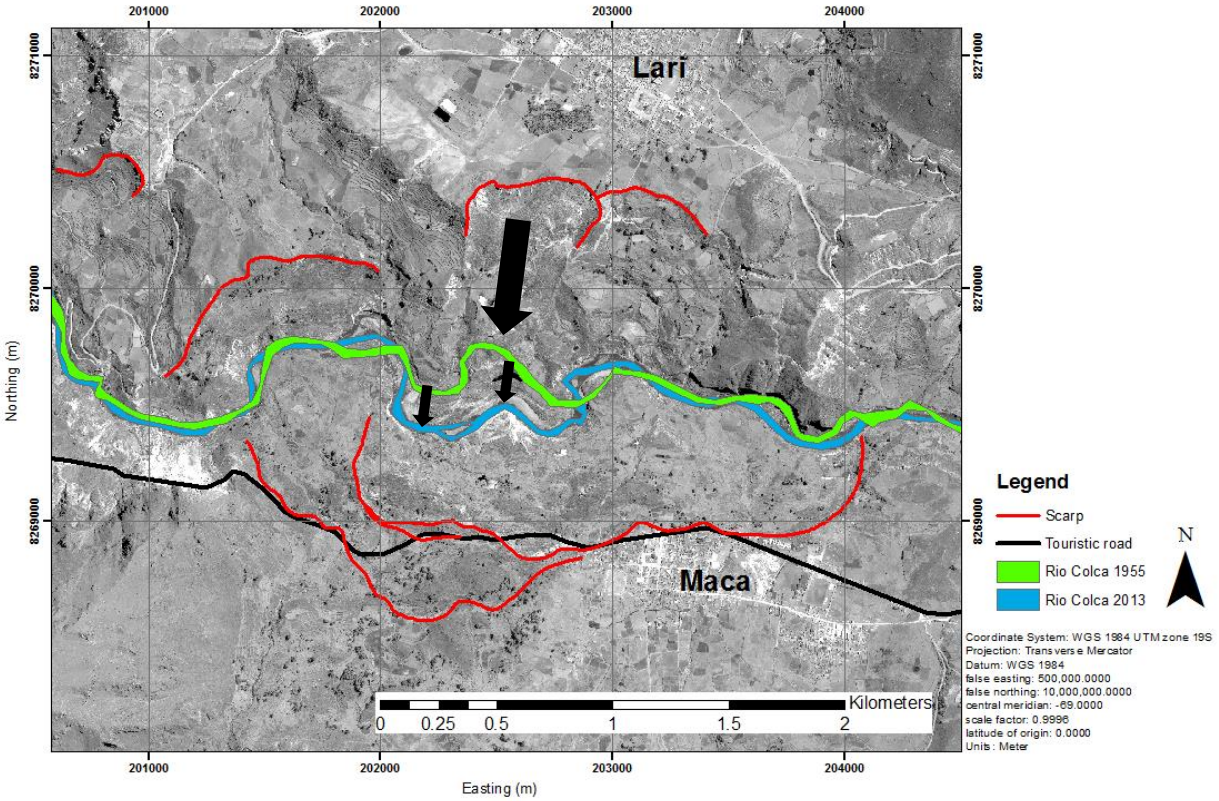

Figure 3: Zoom on the Maca/Lari area. The difference between the Rio Colca in 1955 (green, extracted from an aerial photograph) and the Rio Colca in 2013 (blue, extracted from a Pléiades image), with the main scarps of the area as red lines. A road can be seen crossing the scarp of the Maca landslide. The arrows denote the movement of the Lari landslide, which has pushed the river towards the south.

The landslide near Maca has an approximate area of 1 km2 and a mean slope of 5°. The landslide has three separate forcing factors. The initiating trigger is probably the landslide that has occurred near Lari, which forces the river to erode its banks near Maca (Figure 3). Furthermore the seasonally high rainfall triggers landsliding and the seismicity that is prominent in the area accelerates landsliding (Zavala et al. 2012; Lacroix et al. 2014). The speeds associated with the landslide range from 1.3 m/month to millimeters per year. As the whole mass slides cracks appear at the top of the slide, at which water can infiltrate more easily.

3. Materials and methods

Table 1: Satellite images that have been used in this research.

Date (dd/mm/yyyy)	Satellite type	Stereo or mono	Images	Across/along track viewing angle	B/H	Incidence angle from nadir (°)	Resolution (m)
21/03/2013	Pléiades 1A	Stereo	1 2	0.9/-6.48 -1.5/5.57	0.21		0.7
15/04/2013	Pléiades 1B	Stereo	1 2	-16.2/-8.7 -18.4/3.1	0.21		0.7
29/07/2013	Pléiades 1A	Mono	1	2.9/-14.1	-		0.7
05/02/2014	SPOT	Mono	1		-	1.92	1.5
21/04/2014	Pléiades 1B	Stereo	1 2	-11/10.7 -5.6/-15.2	0.45		0.7

3.1 Satellite data

For this study five acquisitions of Pléiades and SPOT6 images spanning thirteen months of time have been used.

The Pléiades satellites consist of two satellites, Pléiades A and B, which are capable of recording stereo pairs within a few tens of seconds due to the high agility of the satellites. This accommodates the use of its images for stereoscopy (Jacobsen 2011). The Pléiades satellites are pushbroom satellites with a sun-synchronous, phased and near-circular orbit at a mean altitude of 694 km. They have five spectral bands available; one panchromatic band at a resolution of 0.7 m that is resampled to a resolution of 0.5 m and four multispectral bands (B, G, R, and IR) at 2.8 m that are resampled to 2 m. The panchromatic bands of three stereo images and one mono image have been used (Table 1).

The information on the stereo images can be expanded with the B/H ratio (Figure 4). This ratio describes the angle between the positions of the satellite during the two acquisitions by dividing the length of the baseline of the satellites by the height of this baseline. The result demonstrates the degree of stereoscopy.

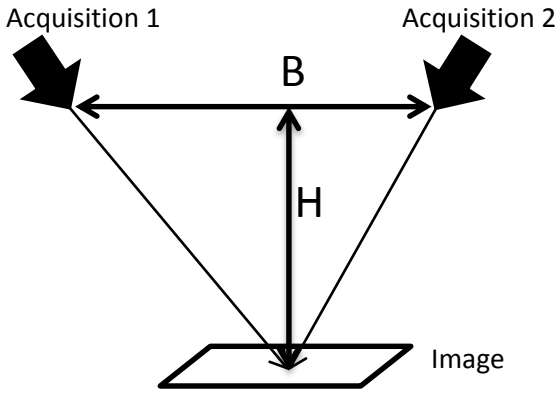

Figure 4: Representation of the two satellite acquisitions of the image, of which a B/H ratio can be calculated.

The SPOT6 satellite is similar to the Pléiades satellites, with a similar orbit at the same altitude. It has four bands; panchromatic at a resolution of 1.5 m. and 3 multispectral bands (B, G, R, IR) at a resolution of 6 m. The panchromatic band of one mono image will be used (Table 1).

3.2 Meteorological data

Rainfall records recorded in Madrigal (Figure 5) are available from the first of November, 2011, up until the end of August, 2014. The measurements are twice daily. The dynamic between dry and rainy seasons in shows a binary rhythm, with high amounts of rainfall during the months December to April and little in the remaining months. From 2012 to 2014 the cumulative rainfall of each rainy season has decreased, with the rainy season of 2014 having half the rainfall amounts of the season of 2012.

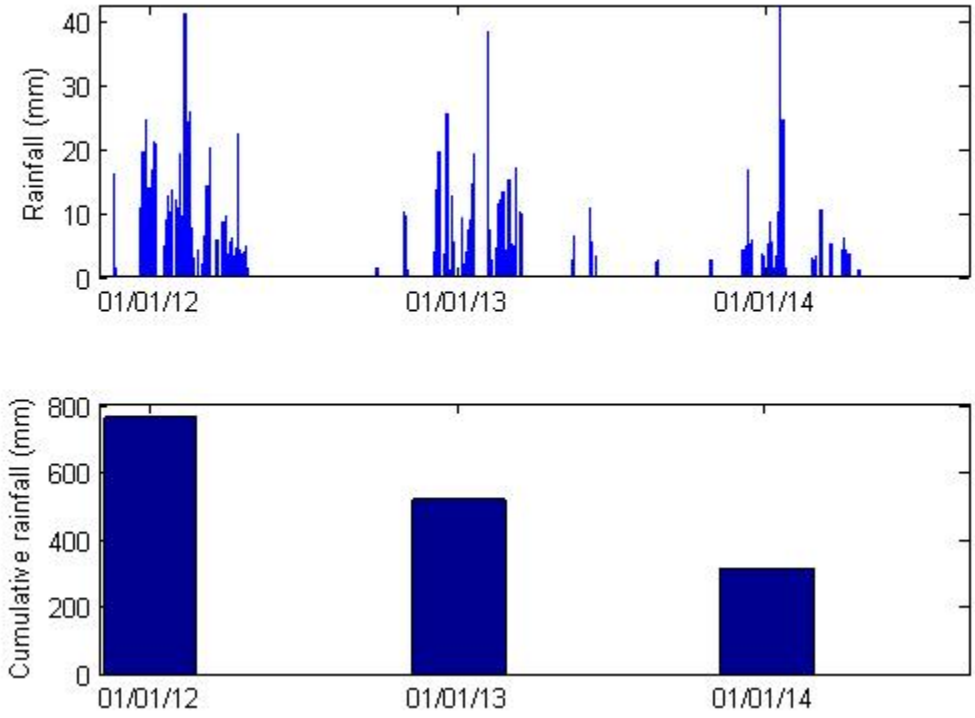

Figure 5: a) Daily amount of rainfall measured in Madrigal. b) Cumulative amount of rainfall measured in Madrigal over one year, from June to June.

3.3 GPS data

A Ground Control Point (GCP) was recorded in the village Achoma in August of 2014. It is very well visible on the satellite imagery due to its placement (Figure 6). It has an accuracy of 4.5 cm in EW direction, 2.7 cm in NS direction, and 59 cm in vertical direction.

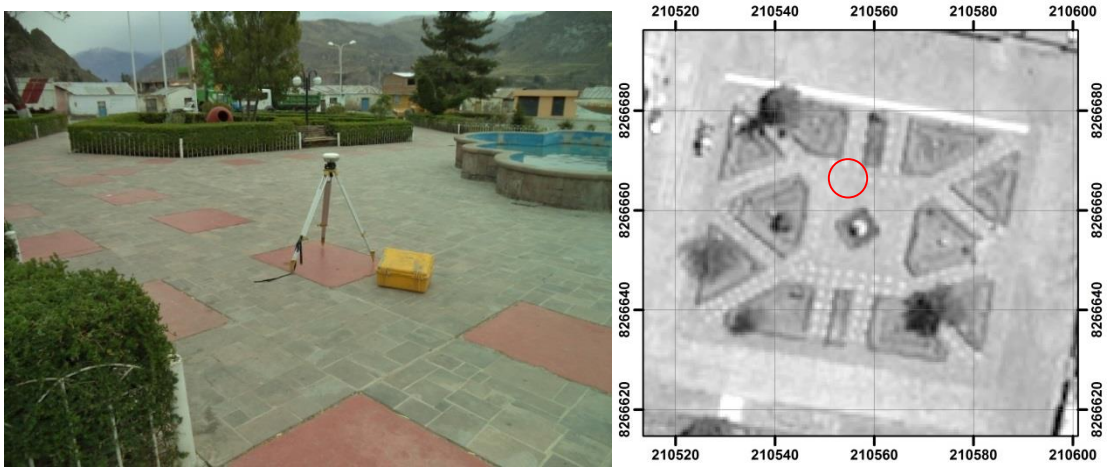

Figure 6: GCP in the village Achoma. Left its position in the village and right its visibility on the satellite imagery.

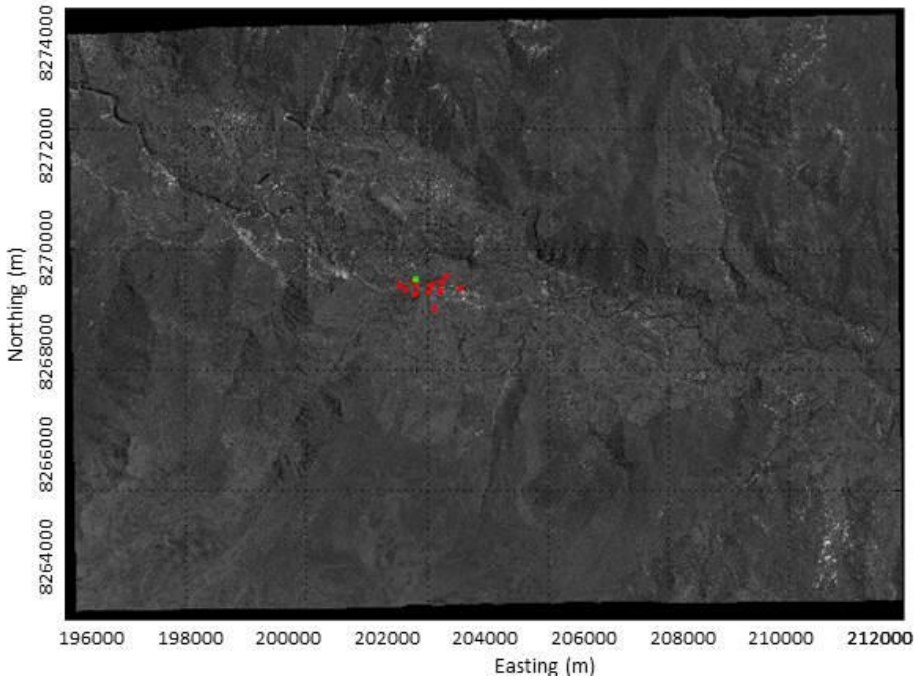

Figure 7: GPS points (red) and permanent GPS (green) positioned in the Colca valley, on an orthoimage of March 2013.

On the Maca landslide 12 markers are present since November 2011 (Figure 7). Their positions have been recorded in February 2013 and in September 2013, using a static base installed during 48h and mobile GPS stations measuring markers on sessions of 2 hours. The baseline between the static base and the mobile stations is less than 1 km.

A permanent GPS has been installed in December 2012 (Figure 7) that provides a daily velocity measurement of the landslide movement (Figure 8). The GPS data have been processed using the GAMIT/GLOBK software (Herring et al. 2010), that provides positions with uncertainties of 2 mm in horizontal and 5 mm in the vertical (Lacroix et al. 2014).

The displacement measured by the GPS shows high displacement rates from December 2012 to June 2013, which occur during and after the rainy season. On the 17th of July a small increase in the displacement is visible, due to an earthquake that occurred that day (Lacroix et al. 2014). The earthquake was at a distance of 20 km of Maca and had a magnitude of 6.0 M_w.

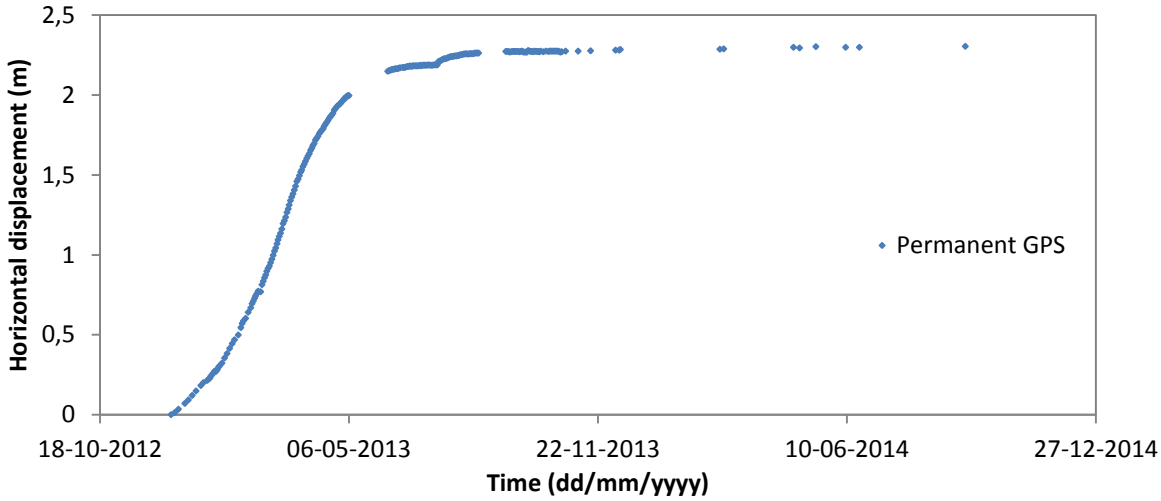

Figure 8: Cumulative horizontal displacement of permanent GPS located on the Maca landslide.

3.4 Method

To measure horizontal displacement a classical scheme was followed (Leprince et al. 2007; Stumpf et al. 2014):

1) DTM generation
2) Orthorectification
3) Correlation

After which the quality of the DTMs and displacement maps has been evaluated.

3.4.1 DTM construction

All DTMs were constructed with the Orthoengine module of PCI Geomatica 2013 using an ASTER GDEM, with a resolution of 15 m, to acquire a regular distribution of tie points over the terrain. Several processing parameter settings are available in the creation of the DTM; the DTM detail was set as 'High', the terrain type was set as 'Hilly', because there is a mix of terrain types present in the area. DTMs of which the holes were filled using a low smoothing filter were constructed and DTMs without filling of the holes. A Wallis filter was applied, due to the fact that shadows are created by the high cliffs present in the images. The output resolution of the DTMs is 2 meters.

To create Digital Terrain Models from stereo images it is common to have several GCPs. However, for the imaged area only one accurate GCP is available (Figure 6). Here the added benefit of the Pléiades imagery is relevant; the orientation of the sensor during acquisition is recorded and with the use of rational polynomial functions (Fraser et al. 2006; Poli & Toutin 2012)it is possible to use 5-10 GCPs for an

accurate orthorectification (Stumpf et al. 2014), but even one accurate GCP is sufficient to remove most vertical bias (Berthier et al. 2014; Lacroix & Berthier, in review).

Three DTMs have been constructed from the three Pléiades stereo pairs, one for March 2013, one for April 2013, and one in April 2014. Also, three DTMs without filling of the holes were constructed, to check the effect of satellite looking angle on the DTM. Georeferencement shifts were detected in the DTMs relative to each other (Figure 9). Each DTM was shifted to be georeferenced (Nuth & Kääb 2011), with the March 2013 DTM as reference. The shift was quantified as 60 to 180 cm of horizontal shift between DTMs.

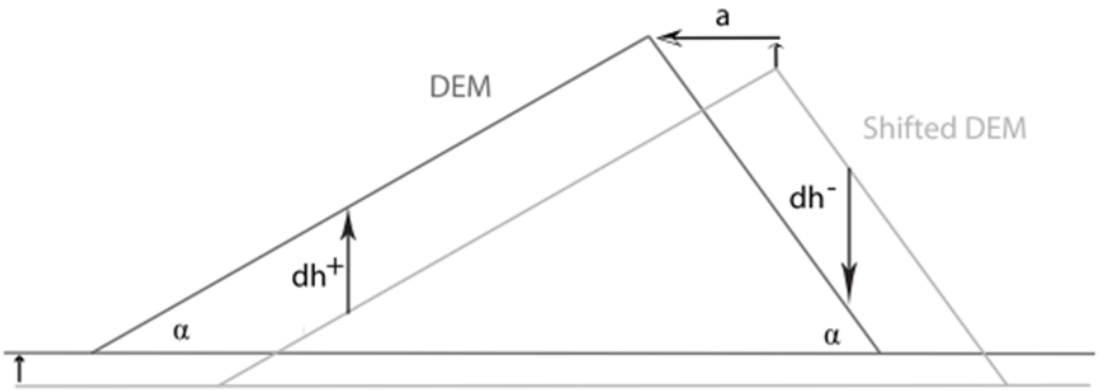

Figure 9: Effects of a shifting in georeferencement of DTMs on the subtraction of the DTMs. (Nuth and Kääb, 2011)

3.4.2 Geometric modelling and orthorectification

The aim of geometric modelling is to describe the relationship between image and ground coordinates for a given sensor and correct for the bias created by the sensor. Geometric modeling was done according to the Rational Function Model (RFM) (Fraser & Hanley 2005). RFM is a bundle adjustment that makes use of rational polynomial coefficients (RPCs), which are orientation parameters derived from satellite ephemeris and attitude. The bundle adjustment has been performed with one GCP.

Orthorectification was done with the Orthoengine module of PCI Geomatica 2013. Of the stereo-pairs the image with the lowest angle from nadir has been selected for orthorectification (Table 2). The images from the stereo-pairs have been orthorectified with the DTM that was produced from the same pair. The mono image of July 2013 has been orthorectified with the DTM from March 2013 and the mono image of February 2014 has been orthorectified with the DTM from April 2014, due to the fact that there are clouds present in both images.

Table 2: Images that have been orthorectified, with a number denoting the image of the stereo-pair that has been used, and the DTMs that were used, with their resulting accuracies.

Date (dd/mm/yyyy)	Image orthorectified	DTM	Resolution (m)
21/03/2013	Pléiades 1A - 2	21/03/2013	0.7
21/04/2013	Pléiades 1B - 2	21/04/2013	0.7
29/07/2013	Pléiades 1A	21/03/2013	0.7
15/02/2014	SPOT6	25/04/2014	1.5
25/04/2014	Pléiades 1B - 2	25/04/2014	0.7

3.4.3 Displacement estimation

The orthoimages have been correlated by means of the module COSI-CORR (Leprince et al. 2007). COSI-CORR achieves image correlation based on frequency-domain correlation. The relative displacement is estimated with an iterative unbiased processor that estimates the phase difference in the Fourier domain. The process consists of two steps. The first step computes the pixel displacement between two windows and relocates the windows to compensate for the relative displacement. Then a correlation is performed on the relocated windows to determine the subpixel displacement. The method has a theoretical accuracy of 1/50 of the image resolution. That is an accuracy of 0.014 m for correlated Pléiades imagery and 0.03 m for correlated SPOT6 imagery. The maximum displacement that is expected is approximately 5 meters, which corresponds to 10 pixels; therefore a local window of 32 pixels width and a step of 16 pixels were used.

The time-period over which images can be correlated depends on the change present in the area that is being imaged, which can depend on vegetation, construction works, river erosion and sedimentation, earthquakes, and of course landsliding. Too much change between correlation images can lead to decorrelation (Leprince et al. 2007). Other sources of decorrelation include differences in shadow length of high objects and topography, when images have been recorded on different times of day or year (Leprince et al. 2007; Lucieer et al. 2013), and translationally invariant objects, such as roads and canals (Leprince et al. 2007). The area of Maca has relatively little vegetation in the form of agriculture on terraces and over the course of one year the changes caused by construction works and the river are negligible. It is expected that the correlation of images spanning one year will not be problematic.

The correlation produces 3 output maps; movement from East to West, movement from North to South, and the Signal to Noise Ratio (SNR). The resolution for these outputs is 8 meters for the correlations between Pléiades images and 24 meters for the correlations with the SPOT6 image. Correlations have been done for all the SPOT6 and Pléiades images, resulting in ten ground-movement maps (Figure 10).

The separate East-West and North-South maps have been integrated to total displacement maps using the following formula:

$$d_{tot} = \sqrt{(d_{EW} - m_{EW})^2 + (d_{NS} - m_{NS})^2} \qquad (2)$$

Where d_{tot} is total displacement, d_{EW} is displacement in East-West direction and m_{EW} the median of displacement in East-West direction. The median has been subtracted to correct remaining shifts that are the result of the shift in georeferencing of the raw imagery and it has been chosen instead of the mean to exclude noisy outliers in the general shift (Höhle & Höhle 2009). As the shift in georeferencing for the images may not be homogeneous for the images, an area is chosen around each of the recognized landslide and inside this area a stable area is selected. The median of the stable area is subtracted from the area of the landslide in question.

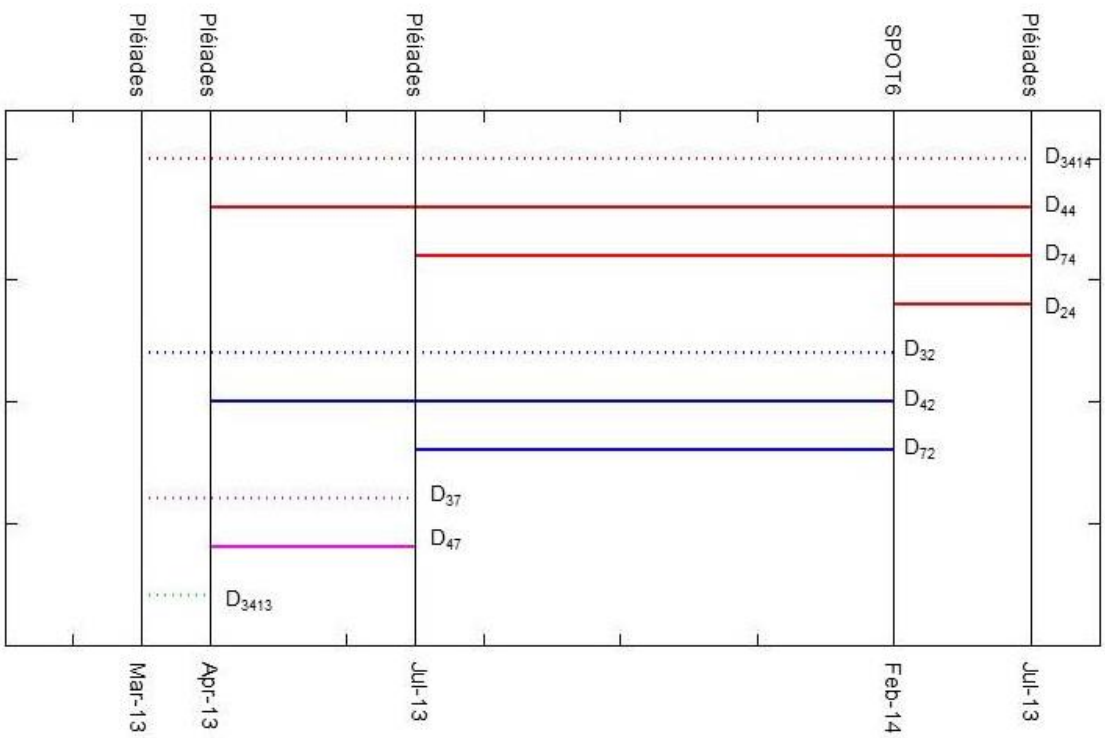

Figure 10: Correlations made between the five available orthoimages. The black vertical lines represent the acquisition times of the satellite images. Time is in months and satellite type is indicated on top. The simple method of computing cumulative movement is represented by the dotted lines. The weighted method is represented by the colored correlations, e.g. the cumulative movement of July, 2013, is calculated by using the weighted movements found in the green and magenta correlations.

The resulting maps have been filtered according to several methods:

- The SNR; any pixel that has an SNR lower than 0.95 has been removed.
- A second filter has been applied by removing all pixels at the location of interpolated areas of the DTMs, because at the location of the holes the DTM, and thus the orthoimage and displacement map as well, is deemed unreliable.
- A final filtering has been applied using the difference between the zonal median and the displacement of a pixel, with the following boundary condition:

  $$\left|D_{ij} - m\right| < 1$$

  Where D_{ij} is the displacement of the pixel of row i and column j, and m is the median in a kernel around this pixel. The kernel for the median is 5 by 5 pixels around each pixel, which after trial-and-error was found to be the optimal value to include relevant displacements for each pixel. When the boundary condition is exceeded the pixel is removed.

3.4.4 DTM quality evaluation

The areas on the DTM that are interpolated are deemed to be inaccurate, as no real information is present in them. Therefore the accuracy of the DTMs will be determined on the DTMs without interpolation, according to two methods. First the uncertainties were estimated by comparing the GPS points with the DTMs. Then the uncertainties were determined based on the differences between the three DTMs. As clouds are present in the stereo-images of April 2014 the DTMs have been cropped to exclude the anomalies caused by them (Figure 11) and statistics of these cropped images were computed with the following scheme:

1) The difference between the DTMs is taken, resulting in three difference-maps;
2) The average value and standard deviations of each difference map have been computed: (μ_{12}, σ_{12}), (μ_{13}, σ_{13}), (μ_{23}, σ_{23});
3) Assuming that each distribution of the errors are Gaussian, the individual standard deviations of the DTMs can be computed by solving the following system of equations:

$$\begin{cases} \sigma_{12}^2 = \sigma_1^2 + \sigma_2^2 \\ \sigma_{13}^2 = \sigma_1^2 + \sigma_3^2 \\ \sigma_{23}^2 = \sigma_2^2 + \sigma_3^2 \end{cases} \quad (1)$$

The operations to determine the statistics for the DTMs have been done both for all the DTMs as a whole and for each slope class every five degrees on all the DTMs.

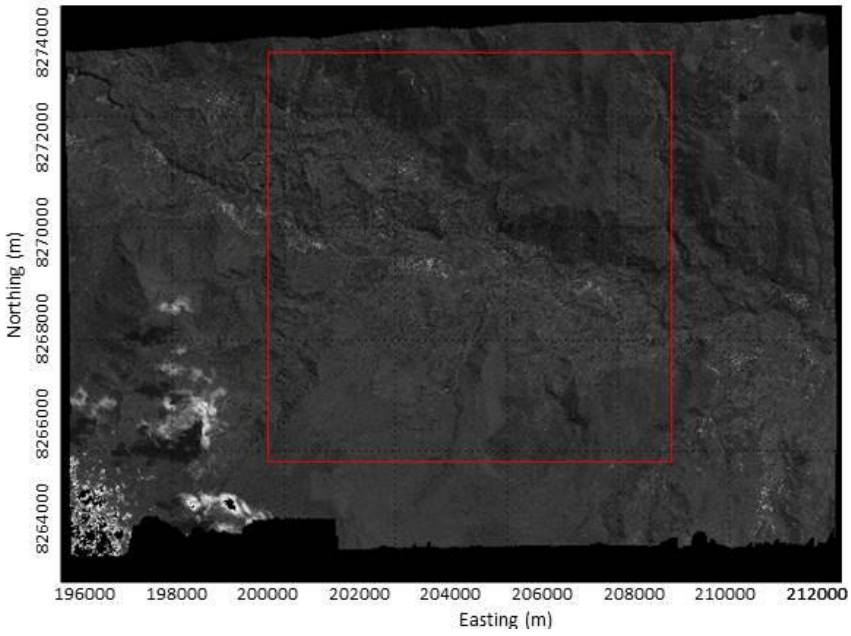

Figure 11: Orthoimage of April 2014 with clouds in the southwestern corner and the crop made to exclude clouds as a red rectangle.

3.4.5 Displacement quality evaluation

Two approaches have been taken to evaluate the quality of the displacement maps. Firstly the statistics of an area that is stable have been calculated. Secondly the displacement of the Maca landslide computed by the correlation has been compared with the displacement detected by the GPS present on the landslide (Figure 8).

Around each landslide the same stable area that has been used to correct the shift in georeferencing is selected to determine the deviation from zero. In addition to the median and standard deviation, also the Normalized Median Absolute Deviation (NMAD) is calculated (Höhle & Höhle 2009). The NMAD describes the dispersion of data at a confidence level of one sigma, while ignoring the outliers in a dataset:

$$NMAD = 1.4826 \cdot \text{median}(|\Delta h_j - m_{\Delta h}|) \qquad (3)$$

Where Δh_j denotes the individual errors and $m_{\Delta h}$ is the median of these errors.

The displacement fields have also been evaluated by comparison with the displacement recorded by the permanent GPS that is present on the Maca landslide (Lacroix et al. 2014). The cumulative movement resulting from the satellite imagery has been computed in two different manners. The simplest method is taking the cumulative movement from March, 2013, to a point in time (the dotted lines in Figure 10). The second method takes the mean of all correlations up to a point in time and gives each one a weight according to the standard deviation that was found in the unmoving area. For example, there are two ways to obtain the cumulative displacement at July, 2013. First simply the displacement map between March and July, 2013, can be used, but the displacement maps between March and April, and April and July are also relevant to this movement. Thus both displacements have been weighted with their standard deviation, ensuring that the most accurate displacement accounts for the most displacement:

$$D_{37} = \frac{\frac{1}{\sigma_{37}} D_{37} + \frac{1}{\sigma_{34+47}} (D_{34} + D_{47})}{\frac{1}{\sigma_{37}} + \frac{1}{\sigma_{34+47}}} \qquad (3)$$

Where D_{37} is displacement between March and July, σ_{37} is the standard deviation of the displacement between March and July, and σ_{34+47} is the combined standard deviation of the displacement maps between March and April, and April and July, which is calculated as:

$$\sigma_{34+47} = \sqrt{\sigma_{34}^2 + \sigma_{47}^2} \qquad (4)$$

This calculation gets more complicated as time advances, because more combinations are possible, for example by calculating the displacement between March 2013 and February 2014:

$$D_{32} = \frac{\frac{1}{\sigma_{32}} D_{32} + \frac{1}{\sigma_{34+42}} (D_{34} + D_{42}) + \frac{1}{\sigma_{37+72}} (D_{37} + D_{72}) + \frac{1}{\sigma_{34+47+72}} (D_{34} + D_{47} + D_{72})}{\frac{1}{\sigma_{37}} + \frac{1}{\sigma_{34+42}} + \frac{1}{\sigma_{37+72}} + \frac{1}{\sigma_{34+47+72}}}$$

The calculation for a composite standard deviations for than two correlations gets more complicated as well, as a different method must be applied, using the sum of squares of the error and deviation from

the total mean. First the Error Sum of Squares (ESS) for each correlation is calculated by multiplying the variance with degrees of freedom:

$$ESS = V(n-1) \quad (5)$$

Where V is the variance of the correlation and n the number of pixels used to calculate the variance. Then all ESS's of the correlations are summed to form an overall ESS for all correlations. The deviation of the mean of each correlation from the mean of all correlations together, or the Sum of Squares (SS), is calculated:

$$SS = n(\overline{X_{cor}} - \overline{X_{all}})^2 \quad (6)$$

Where X_{cor} is the mean of one correlation and X_{all} is the mean of all correlations. The SS's of all correlations are summed to form an overall SS. By adding the overall ESS and the overall SS the Total Sum of Squares (TSS) is computed, which is divided by the degrees of freedom to obtain a variance of all correlations:

$$V_{all} = \frac{(ESS_{all}+SS_{all})}{(N-1)} \quad (7)$$

Where V_{all} is the variance of all correlations involved and N is the total amount of pixels of all correlations involved. Taking the square root of this variance produces a standard deviation that is applicable to the addition of multiple correlations.

The error of each cumulative displacement in the weighed method is computed using the same method as computing the cumulative displacement itself; weighting all standard deviations with the standard deviation and averaging them.

Unfortunately due to the calculation of the composite standard deviation it is impossible to apply the NMAD to these weights. This may result in an error for the displacements comparing with GPS that is not only reflecting the accuracy of the data, but also the amount of noise present. Therefore the errors that will be determined using Equation 7 do not apply to the accuracy of the displacement maps, but rather offer a way of comparison between the first simple method and the second weighted method.

4. Results

4.1 DTM

The precision of the DTMs of 2013 at a 66% confidence level (1 standard deviation) is ±80 cm for comparison with GPS and ±70 cm for the differences between DTMs (Table 3). The statistics have been computed over $2.1*10^7$ points for the differences between DTMs and for 12 points for the comparison with GPS. Therefore, the statistics from the differences between DTMs are thought to be more accurate. The accuracy of ±70 cm is better than the accuracies found in Berthier et al. (2014), for a region without vegetation and low slopes.

The result of DTM construction is visible in Figure 12. The DTM of April 2014 has the highest accuracy of 62 cm, due to the high B/H ratio (Table 3). The high angle between both looking angles of the satellite acquisitions allow for a better stereo view. However, together with a better stereo view the data that is below steep cliffs is not acquired and 11.7% of the DTM lacks data (Figure 12c). To have a complete DTM these areas need to be interpolated, but this data is often inaccurate.

The DTMs of March and April 2013 have lower accuracies of 71 and 78 cm, due to their smaller B/H ratios that allow for a poorer stereo view. However, this also means that the amount of areas lacking data is five times smaller than for the April 2014 DTM, with ±2.1% (Figure 12a and b).

Standard deviations for both the interpolated and non-interpolated DTMs have been calculated for each slope class every 5 degrees, to see the influence of slope on accuracy of interpolation. This has been done for the DTMs of March 2013 and April 2014. The accuracies decrease with steepness of slope for both interpolated and non-interpolated areas (Figure 13). The standard deviations of the non-interpolated areas are comparable for both DTMs. However, the interpolated areas show standard deviations that are ± three times as high for the March 2013 DTM (14 m) and ± five times as high for the April 2014 (26 m) than the areas that are not interpolated (5 m and 6 m). This shows the influence of B/H on the accuracy of interpolated slopes. For further results any interpolated areas have been removed.

Table 3: Statistics for DTM without interpolation, which have been cropped to exclude areas obscured by clouds.

DTM	B/H	Interpolated areas (%)	Standard deviation (m)	Standard deviation of error with GPS (m)	RMSE (m)
3/13	0.21	2.2	0.71	0.98	0.66 m
4/13	0.21	2.0	0.78	0.90	0.93 m
4/14	0.45	11.7	0.62	0.62	1.15 m

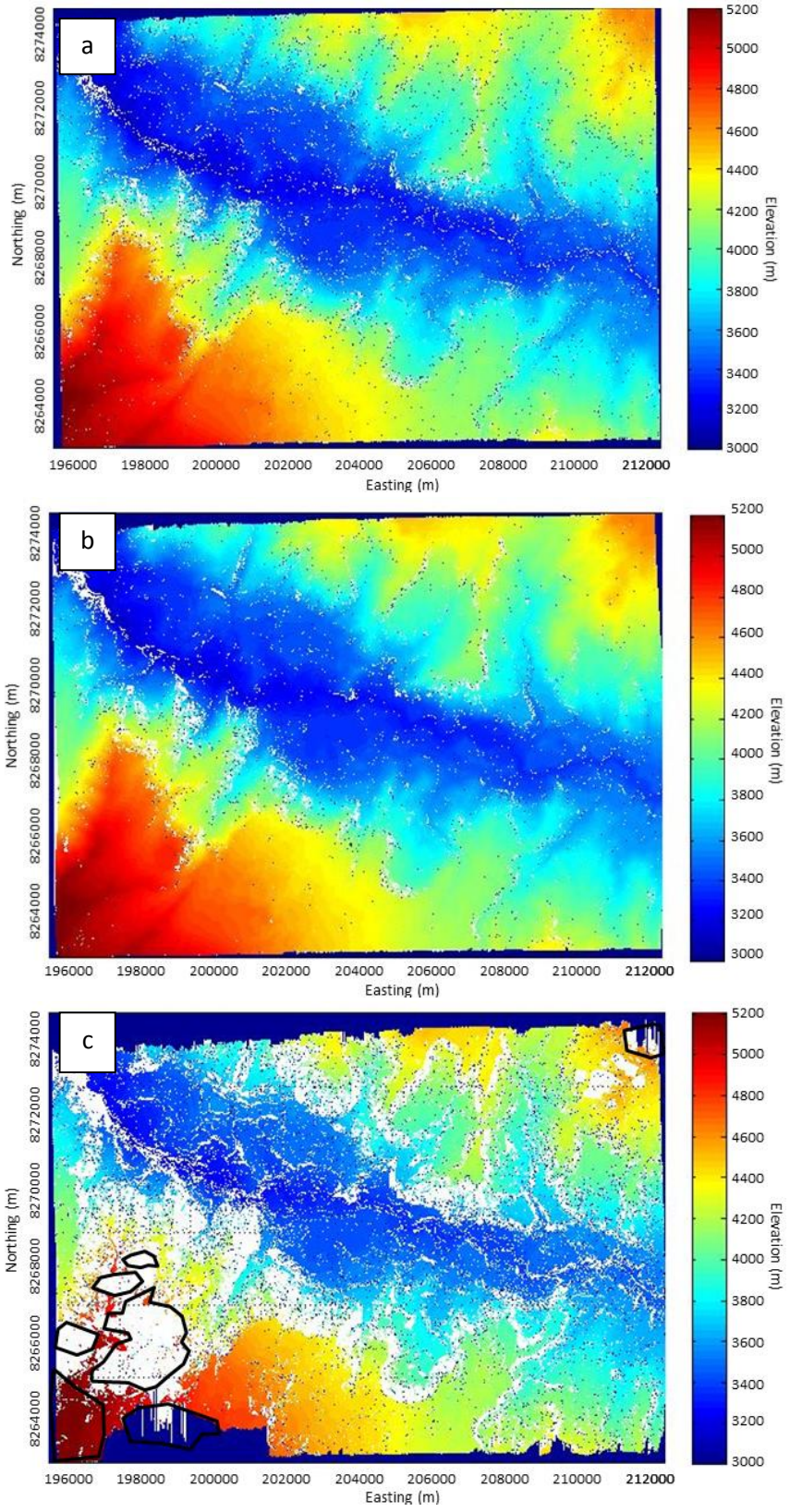

Figure 12: DTMs with interpolated areas indicated with white color. a) DTM March 2013, b) DTM April 2013, c) DTM April 2014. On the April 2014 DTM clouds and their shadows are outlined with black.

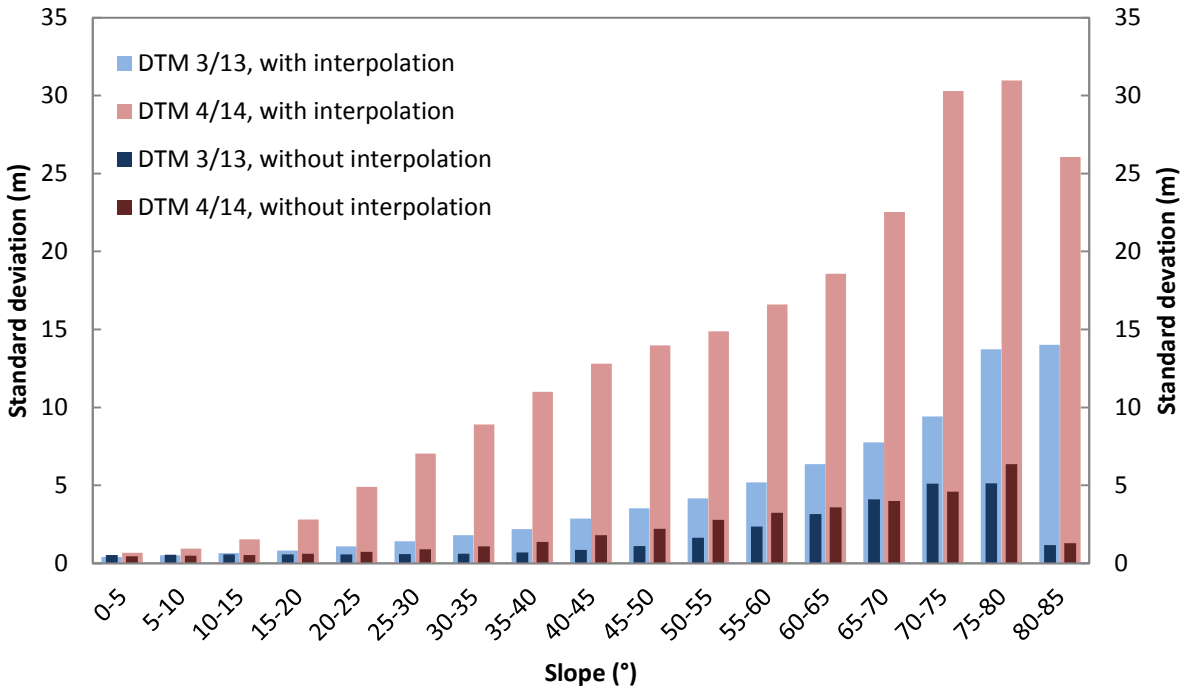

Figure 13: Comparison between standard deviations of each slope class on the DTM of March 2013 and April 2014, either with interpolation or without.

The accuracy of the April DTM is the lowest with ±80 cm, which can be explained by an artifact that has been uncovered by subtracting the April DTM from the other DTMs (Figure 14). The artifact is present as an along-track undulation in the DTM and has an amplitude of approximately 60 cm. It is probably caused by an instrumental problem during acquisition. Other artifacts that have been discovered are several across-track stripes (Figure 12), which are due to errors of cartography of the focal plane. Especially the across-track stripes are visible in further results and may cause errors in the data.

To provide a better DTM of April 2014 it has been attempted to filter the undulated DTM using a Fourier transform (Figure 15). After a 2D Fast Fourier Transform had been made (Figure 15a), the center of the transform, which represents the lowest frequencies that near zero Hertz, has been removed using a Gaussian filter (Figure 15c). When the image was transformed back into the difference between DTMs the undulation has been removed, but edge effects have been created surrounding the holes in the DTMs causing new inaccuracies. Therefore the undulation is considered within the error that has been established earlier and will remain in the DTM.

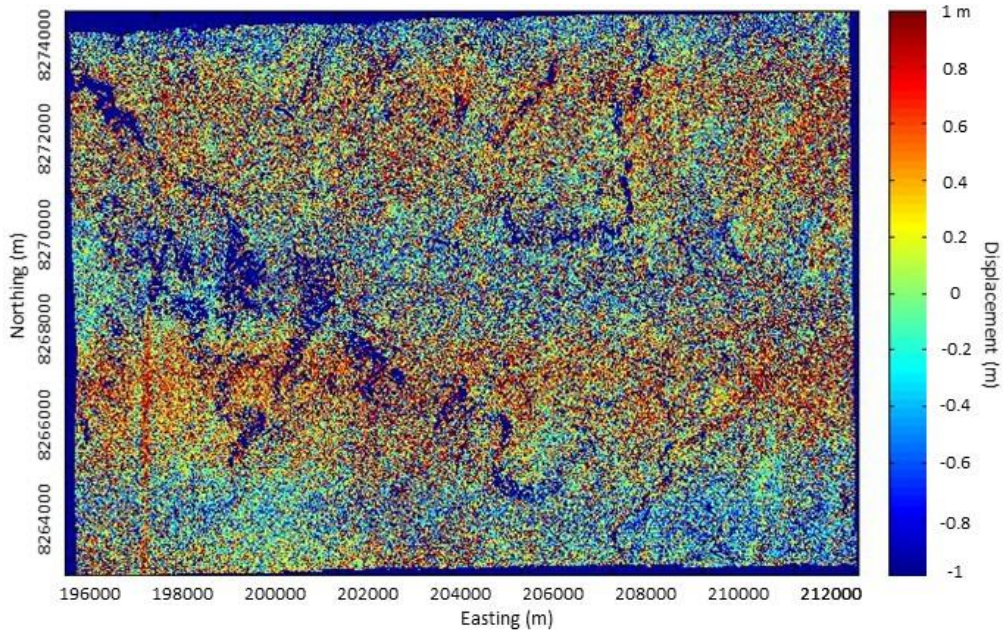

Figure 14: Subtraction of the DTM of March 2013 by the DTM of April 2013, in a range of 1 to -1 meters. The along-track undulation is visible as two horizontal ridges and one horizontal trench. The across-track stripes are visible as vertical lines.

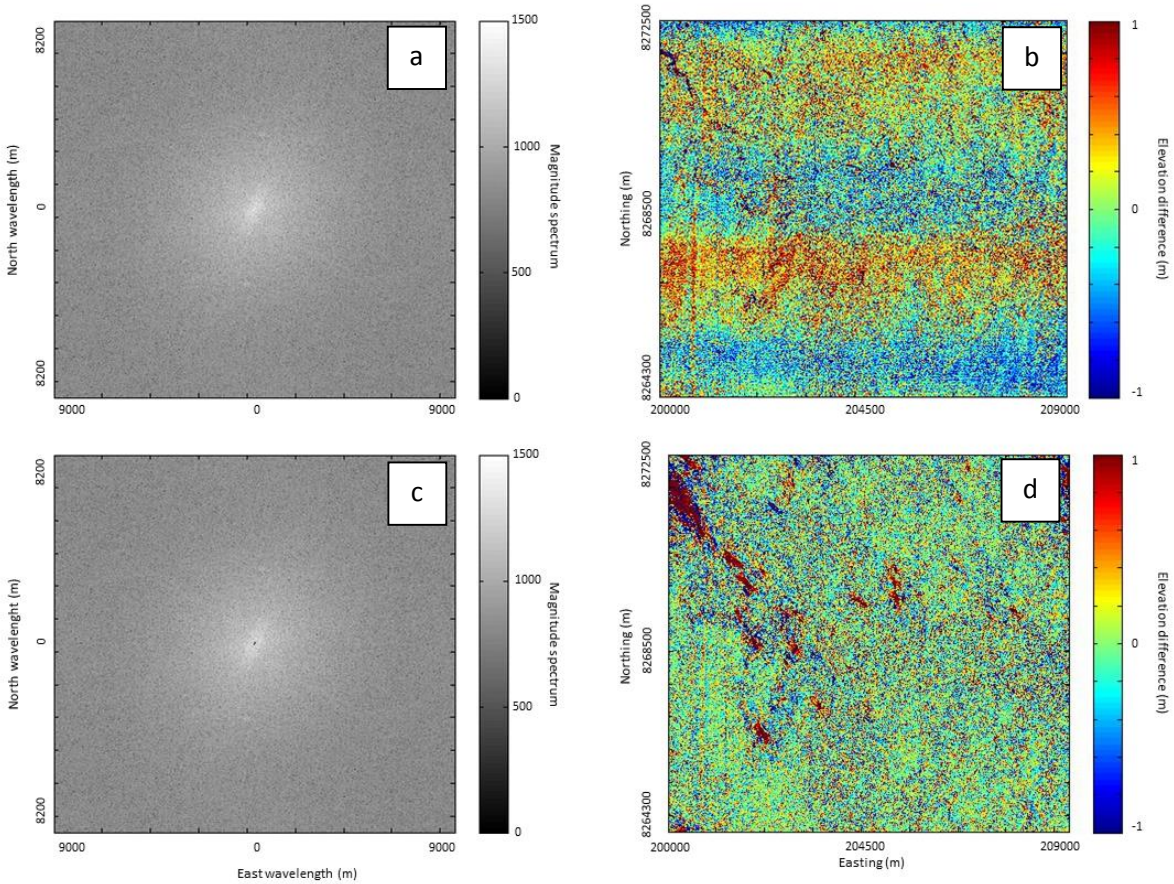

Figure 15: a) 2D Fast Fourier transform of the difference between the DTMs of March 2013 and April 2013, b) unfiltered difference between DTMs, c) the filtered transform, d) end-result of the filtered difference between DTMs.

4.2 Correlation results and validation

Three output maps (Figure 16) have been produced for each correlation (Figure 10, Appendix 1): an East-West displacement map, a North-South displacement map, and a Signal to Noise Ratio (SNR). Several areas of displacement are visible on the partial displacement maps of Figures 16a and b, which coincide with known landslides. Areas of decorrelation are present in the South-West and in the North-East areas of the image, where clouds are present.

The SNR (Figure 16c) of the correlations is overall quite high with an average of 0.97. A band of lower SNR values is present, which coincides with the low elevation part of the Colca valley. The higher elevation areas have relatively high SNR values. In the valley agriculture is practiced, which can cause the vegetation of the valley to change over the year and decorrelation to occur. The slopes of the valley have very little vegetation and no agriculture is practiced here, thus these areas experience a lower level of noise after correlation.

The partial displacement maps are combined into the horizontal displacement map in Figure 17, which shows the masking that has been performed to remove most of the noise. The percentage of noise removed (Table 4) is dependent on three factors: the time-span between images, the image resolution, and B/H ratio. Its dependence on the time-span between the correlated orthoimages is most visible for correlations between Pléiades images (Figure 18a). The relationship is less clear for SPOT6 imagery, because of an additional dependence on resolution of the correlated orthoimages (Figure 18a). Displacement maps of all resolutions show a dependence on B/H ratio (Figure 18b), but again this is more distinct for the Pléiades imagery.

There is a warping effect visible in the partial and total displacement, that is seen best in the Eastern part of the North-South displacement image. This is an effect of the errors of the DTM, where the cartography of the focal plane has not been produced correctly. Therefore, it is necessary to correct the warp in georeferencing for each landslide individually instead of for the whole image. This has been corrected by subtracting the median of a stable area around each landslide from the area of that landslide (Appendix 2).

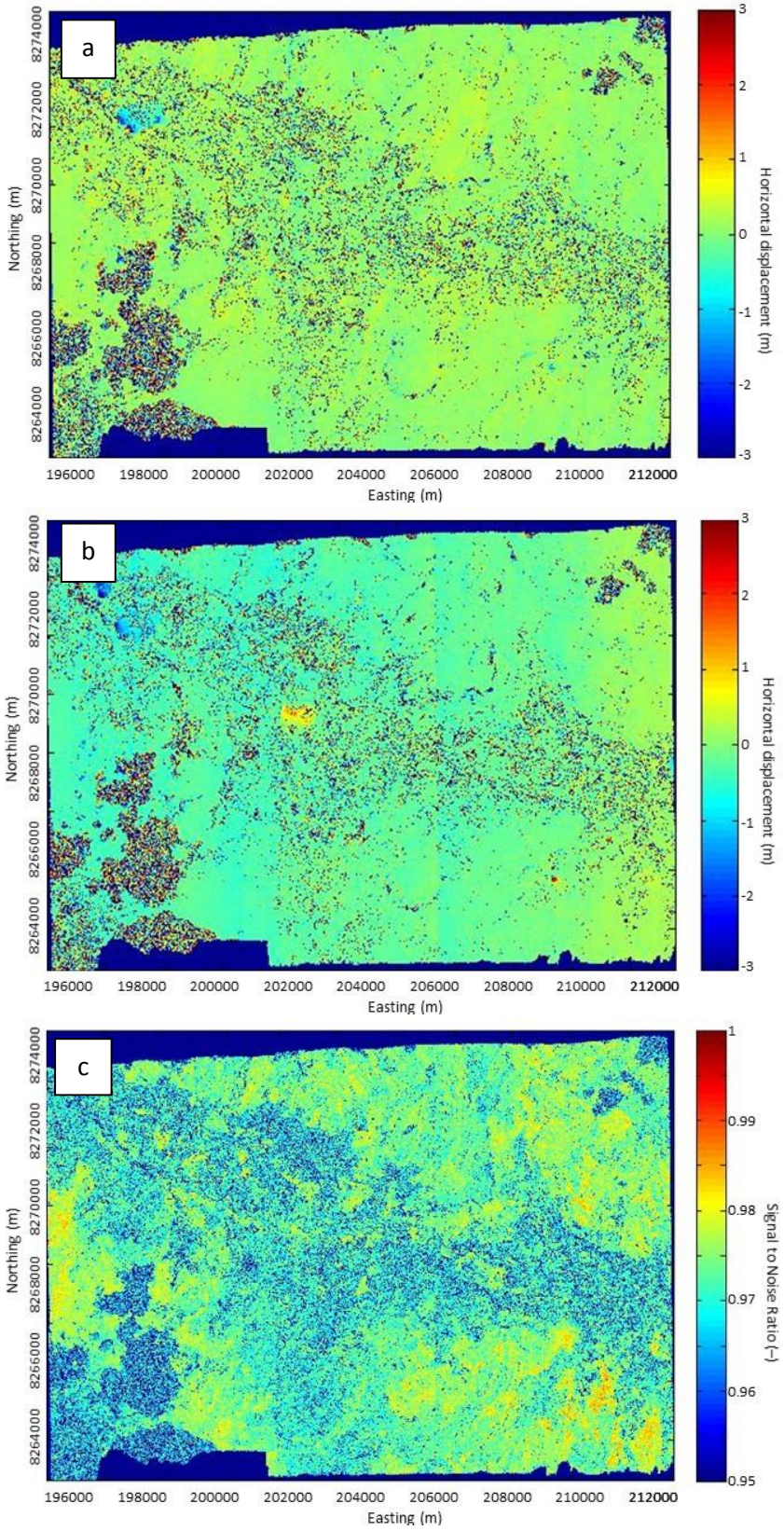

Figure 16: Output maps of COSI-Corr: a) East-West displacement in meters, b) North-South displacement, and c) Signal to Noise ratio, for the period March 2013 to April 2014.

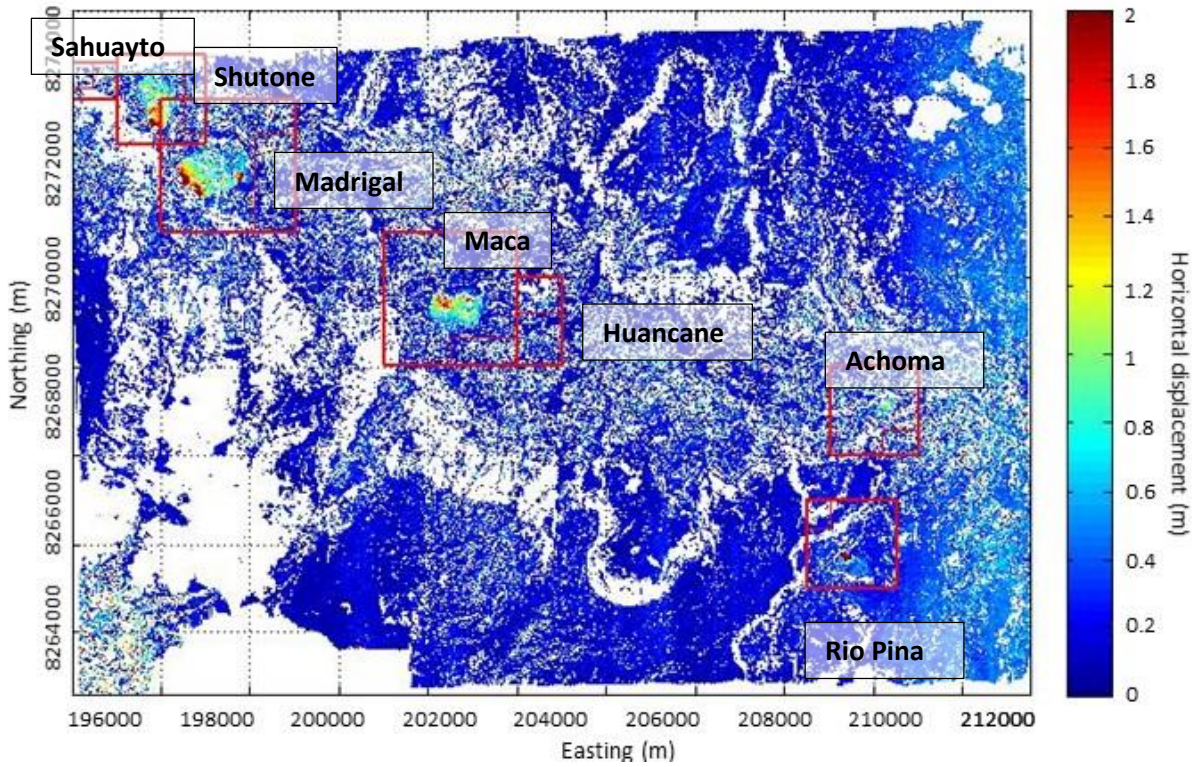

Figure 17: Map of horizontal displacement between March 2013 and April 2014, with all masks implemented. The cut-outs of the landslides are imaged as red squares with thick lines, with their stable areas as red squares with thin lines. From the upper left to the lower right the recognized landslides are: Sahuayto, Shutone, Madrigal, Maca, Huancane, Achoma, and Rio Pina.

Table 4: Percentage of masked areas for each correlation, with time-span in between and resolution of source images.

Correlation	Areas masked (%)	B/H (-)
3/13 – 4/13	8.7	0.21
3/13 – 7/13	16.6	0.21
3/13 – 2/14	34.9	0.33
3/13 – 4/14	37.4	0.33
4/13 – 7/13	13.8	0.21
4/13 – 2/14	15.3	0.33
4/13 – 4/14	34.2	0.33
7/13 – 2/14	19.9	0.33
7/13 – 4/14	37.1	0.33
2/14 – 4/14	32.8	0.45

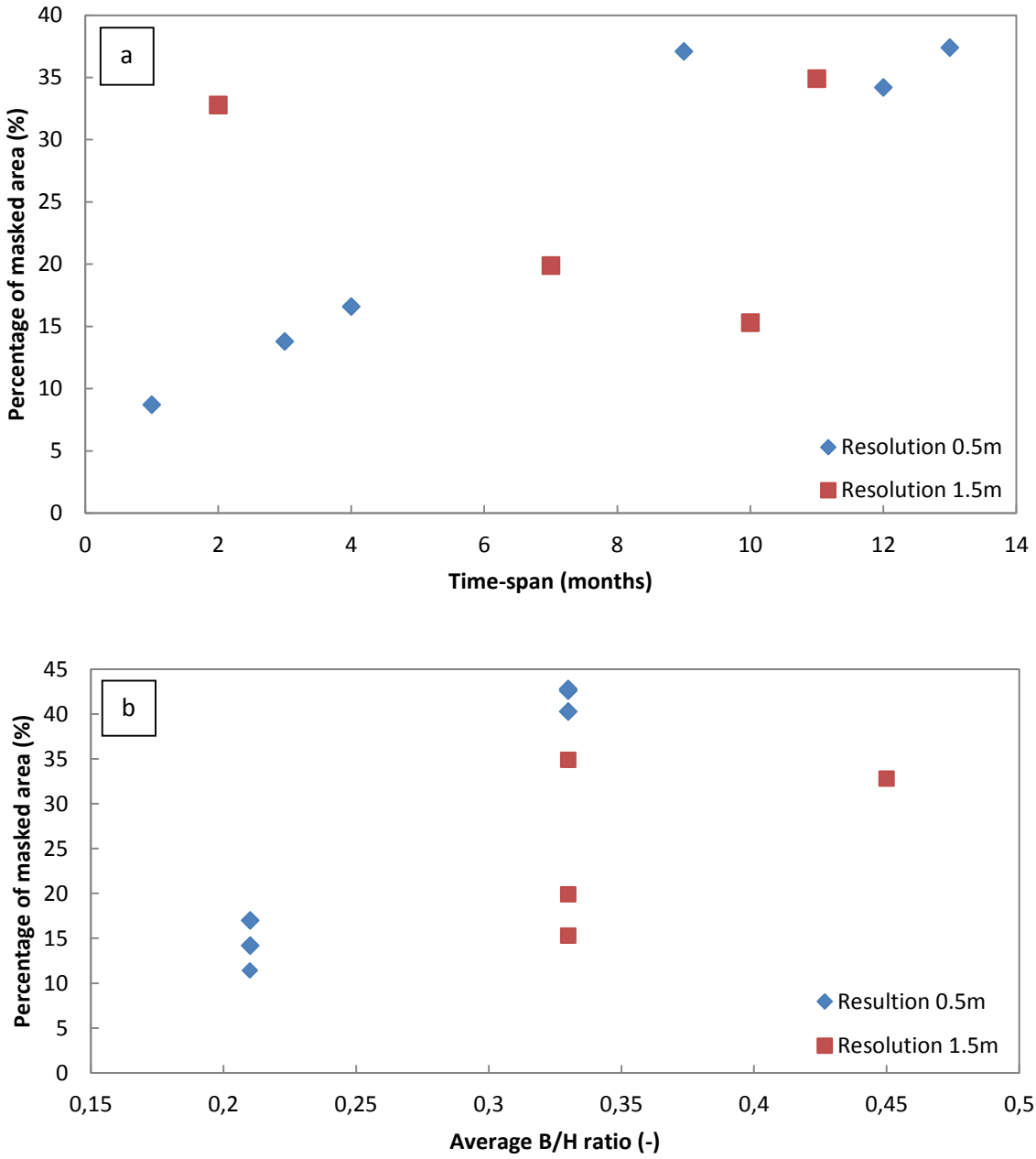

Figure 18: a) Relationship between time-span between correlated images, resolution of the correlated images, and percentage of area masked. b) Relation between the average B/H ratio of the DTMs with which the correlated orthoimages have been orthorectified and percentage of masked area.

The result of the correlations gives a clear image of the areas with active displacement in the Colca valley (Appendix 3). Seven landslides have been visually identified: Achoma, Huancane, Maca, Madrigal, Rio Pina, Sahuayto, and Shutone (Figure 17). Several other areas that are known to be landslide prone are only visible on displacement maps of shorter timespans and disappear into noise caused by decorrelation (Figure 19). These areas are not taken into account. Other decorrelated parts on the landslides are visible near the toe of the landslides where soil is removed or reworked due to high

displacement rates, so that recognition is impossible. One of these parts is seen at the eastern part of the Maca landslides (Figure 20). The denudated edges and the vegetated central area have changed too much. Therefore, any displacement detected in this part of the landslide is unreliable.

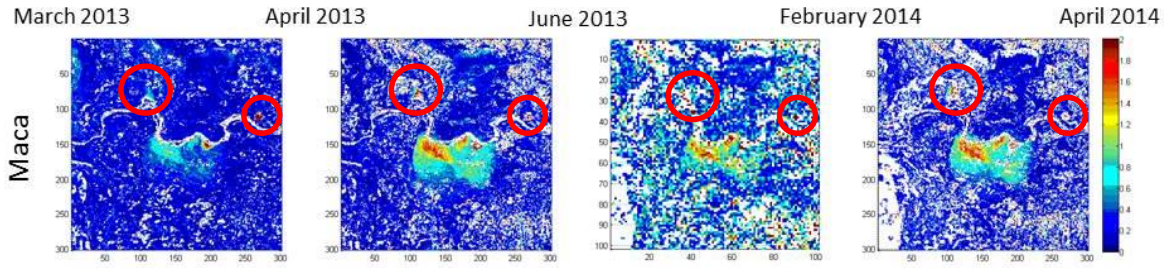

Figure 19: Time-series of cumulative displacement at the Maca landslide. Small landslides that decorrelate over time are indicated with red circles.

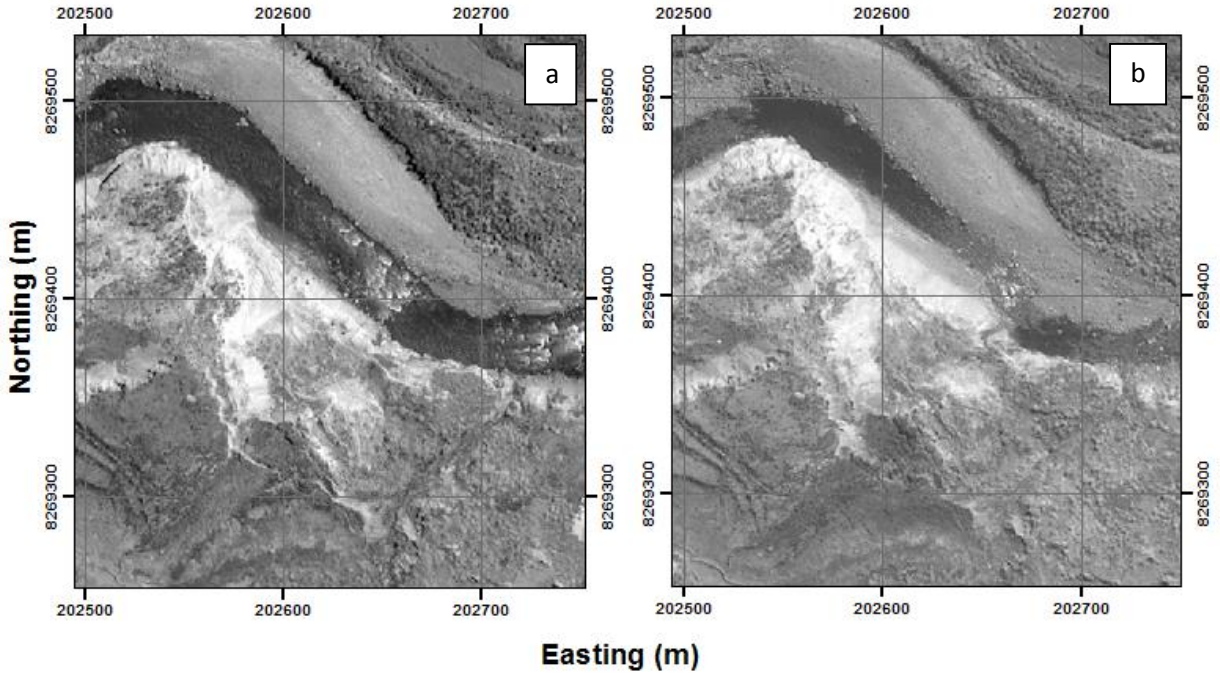

Figure 20: Comparison of the orthoimages of March 2013 (a) and April 2014 (b) for the part of the Maca landslide that has decorrelated. The April 2014 image has more blurry parts and reworked parts that are unrecognizable.

The accuracy of the correlations differs by source image. For all correlations of Pléiades images is between 0.05 and 0.18 meters (Appendix 4, Table 5). For correlations with the SPOT6 image the accuracy is not as good, with an NMAD that is between 0.16 and 0.29 meters (Appendix 4, Table 6). To illustrate the difference between Pléiades and SPOT6 images as a source for correlation the statistics of the displacement field between March 2013 and April 2014 and of the field between March 2013 and February 2014 are shown in Table 5 and 6.

Remarkably, for both the Pléiades and SPOT6 source images the statistics for the Rio Pina landslide are consistently lower than for the other landslides (Table 5 and 6). This coincides with the fact that the Rio

Pina landslide is the only landslide located higher on the slopes of the valley and thus has less vegetation in the area, signifying the importance of little vegetation to reduce noise and increase accuracy.

Table 5: Statistics of the displacement field between March 2013 and April 2014 per landslide.

Landslide	Median (m)	NMAD (m)
Achoma	0.23	0.15
Huancane	0.17	0.13
Maca	0.22	0.16
Madrigal	0.20	0.15
Rio Pina	0.08	0.05
Sahuayto	0.25	0.18
Shutone	0.20	0.15

Table 6: Statistics of the displacement field between March 2013 and February 2014 per landslide.

Landslide	Median (m)	NMAD (m)
Achoma	0.45	0.29
Huancane	0.54	0.29
Maca	0.56	0.39
Madrigal	0.40	0.29
Rio Pina	0.27	0.16
Sahuayto	0.35	0.22
Shutone	0.42	0.28

When comparing the displacement detected by COSI-CORR with the displacement detected by the permanent GPS on the Maca landslide, two methods are used; the simple method and the weighted method (Figure 21). The simple method compares very well with the GPS measurements, with a maximum deviation of 2 cm from the displacement, which is within the error margin. However, the weighted method is considerably worse than the simple method and deviates from the GPS displacements with a maximum of 65 cm. This large deviation is accompanied by equal or slightly higher standard deviations compared with the simple method; 0.49 cm compared to 0.56 cm. For the continued results the simple method has been used as most representative for landslide displacement.

To sum up the validation of the correlation maps, the accuracy of the displacement maps is 6-15 cm for Pléiades imagery and 20-44 cm for SPOT6 imagery, which means that displacement must be higher than these accuracies to be detected.

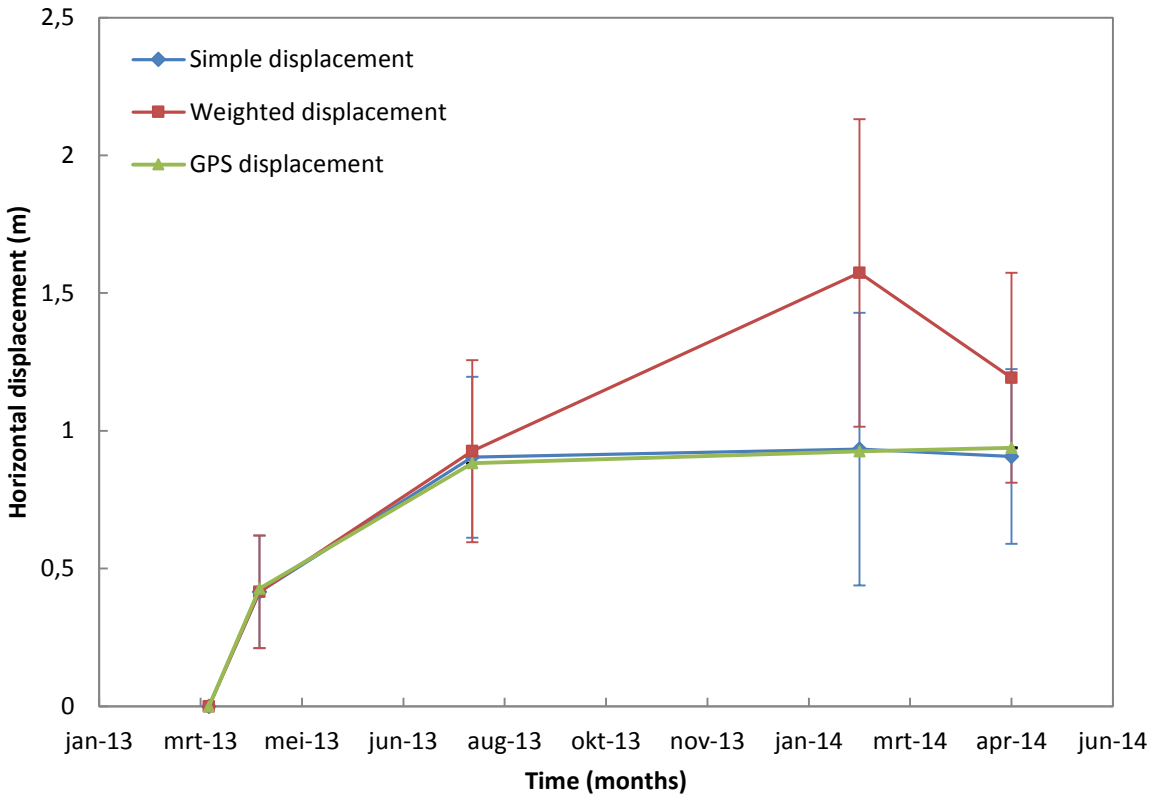

Figure 21: Comparison of the displacement measured by the permanent GPS on the Maca landslide and displacement detected by correlation of the orthoimages. Two methods are applied on the correlated displacement; a simple method (also depicted by the dotted lines in Figure 6) and a weighted method (described in equation 3). The error bars depict the accuracy, which is described by the NMAD.

4.3 Landslide detection

To further quantify the physical characteristics of the landslides four parameters have been chosen: area, mean slope, maximum displacement, and mean displacement (Table 7). The area has been calculated following the scarps and toes of the landslides.

The landslides with the largest areas are found in the northwestern corner of the image (Figure 17): Sahuayto, Shutone, and Madrigal. Sahuayto is a landslide that lies on a side river of the Rio Colca, it has an area of 0.08 km^2 (Table 7) and the area is missing a lot of information due to noise (Figure 22). Sahuayto's maximum displacement is one of the highest found in the area with 0.82 ±0.09 m/month and its mean displacement over a period of thirteen months is the highest with 0.22 ±0.01 m/month. Shutone lies next to it on a side river and it has an area of 0.58 km^2. Its displacement is quite constant, with a mean displacement of 0.17 ±0.01m/month. Madrigal is the largest landslide in the area, with an area of 1.2 km^2, and it lies directly at the Rio Colca. Madrigal's displacement is in the top segment with a maximum displacement of 0.38 ±0.07 m/month and an average displacement of 0.20 ±0.01 m/month.

The four landslides identified on the southern bank of the Rio Colca are Maca, Huancane, Achoma, and Rio Pina. Maca is very similar to the Madrigal landslide, with a large area of 0.73 km^2 and placement directly at the Rio Colca. The landslide features the highest maximum displacement found in the area of 0.91 ±0.11 m/month and an average displacement of 0.14 ±0.01 m/month. Huancane and Achoma are both small landslides at the Rio Colca with areas of 0.02 and 0.12 km^2 and low average displacement rates of 0.06 ±0.01 and 0.08 ±0.01 m/month. Rio Pina is the only landslide that lies in rocky deposits higher on the slopes of the valley at a side river of the Rio Colca. It has an area of 0.35 km^2, a maximum displacement of 0.77 ±0.06 m/month and an average displacement of 0.22 ±0.01 m/month, making it one of the fastest moving landslides together with Sahuayto.

Table 7: Physical characteristics of the seven landslides; landslide area from toe to scarp, mean slope from toe to scarp, maximum displacement measured on the landslide, and mean velocity of point with maximum displacement.

Landslide	Area (m^2)	Mean slope (°)	Maximum displacement (m/month)	Mean displacement (m/month)
Achoma	116413	14	0.29 ±0.04	0.08 ±0.01
Huancane	15850	15	0.19 ±0.09	0.06 ±0.01
Maca	730651	12	0.91 ±0.11	0.14 ±0.01
Madrigal	1210355	10	0.38 ±0.07	0.20 ±0.01
Rio Pina	349020	15	0.77 ±0.06	0.22 ±0.01
Sahuayto	84390	18	0.82 ±0.09	0.22 ±0.01
Shutone	577691	18	0.24 ±0.06	0.17 ±0.01

Cross-sections were made for each landslide (Figure 23), on which a mean slope has been calculated (Table 7). The cross-sections show that every landslide has an irregular surface on a scale of tens of meters. Most landslides show low average slopes from 10 to 15, with two outliers at the Sahuayto and Shutone landslides.

In the following results and discussion emphasis will be placed upon two of the seven landslides; the Maca landslide and the Madrigal landslide. This is due to the importance of the road placed on the Maca

landslide and the fact that useful data has been recorded on this landslide. The Madrigal landslide is very similar to Maca in size, displacement, and placement, and will thus be compared with the Maca landslide.

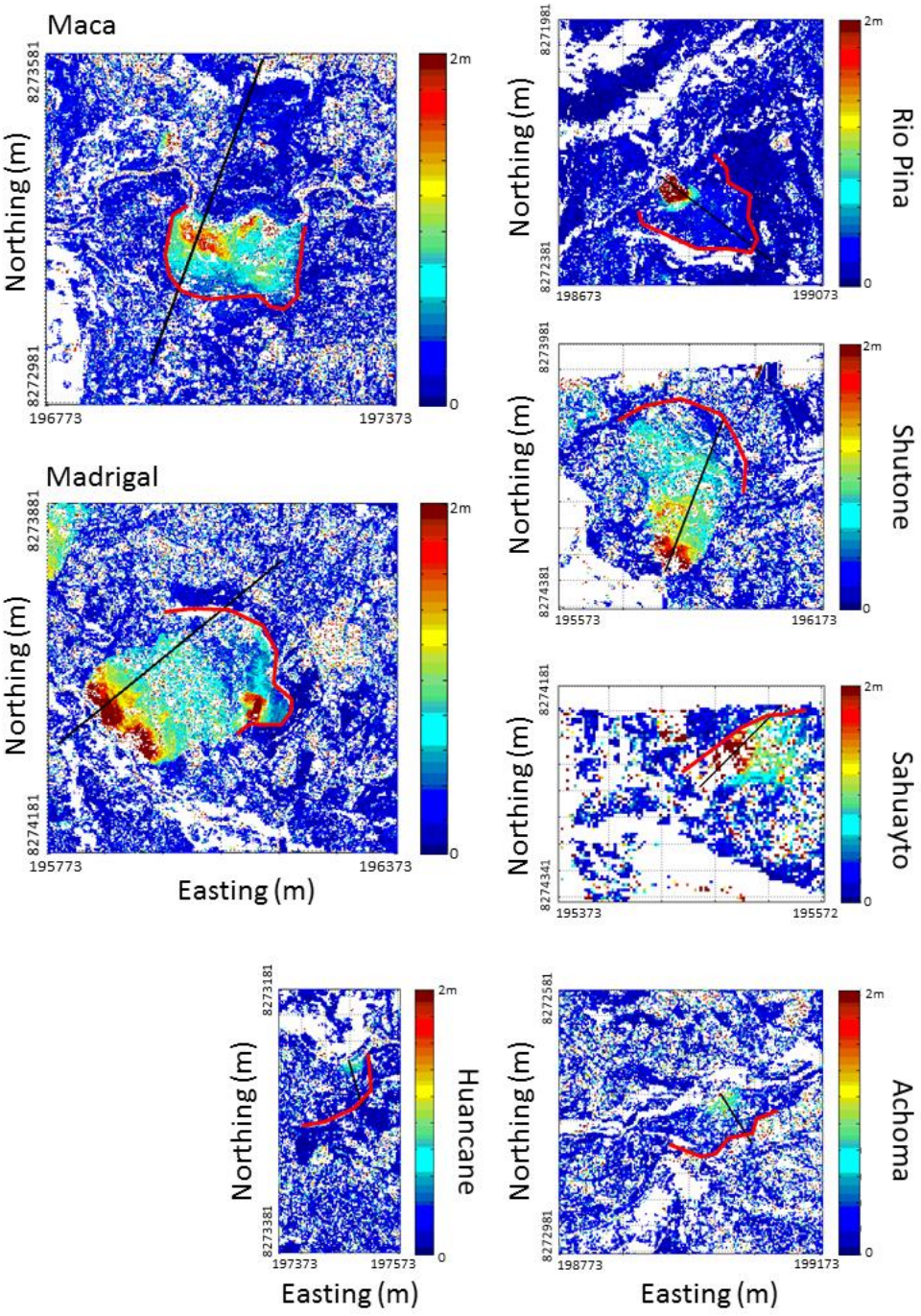

Figure 22: Overview of the landslides found in the Colca valley, with the cumulative displacement from March 2013 to April 2014 in meter. The black lines represent the cross-sections that have been drawn on the DTM of March 2013. The red lines denote the headscarps of the landslides.

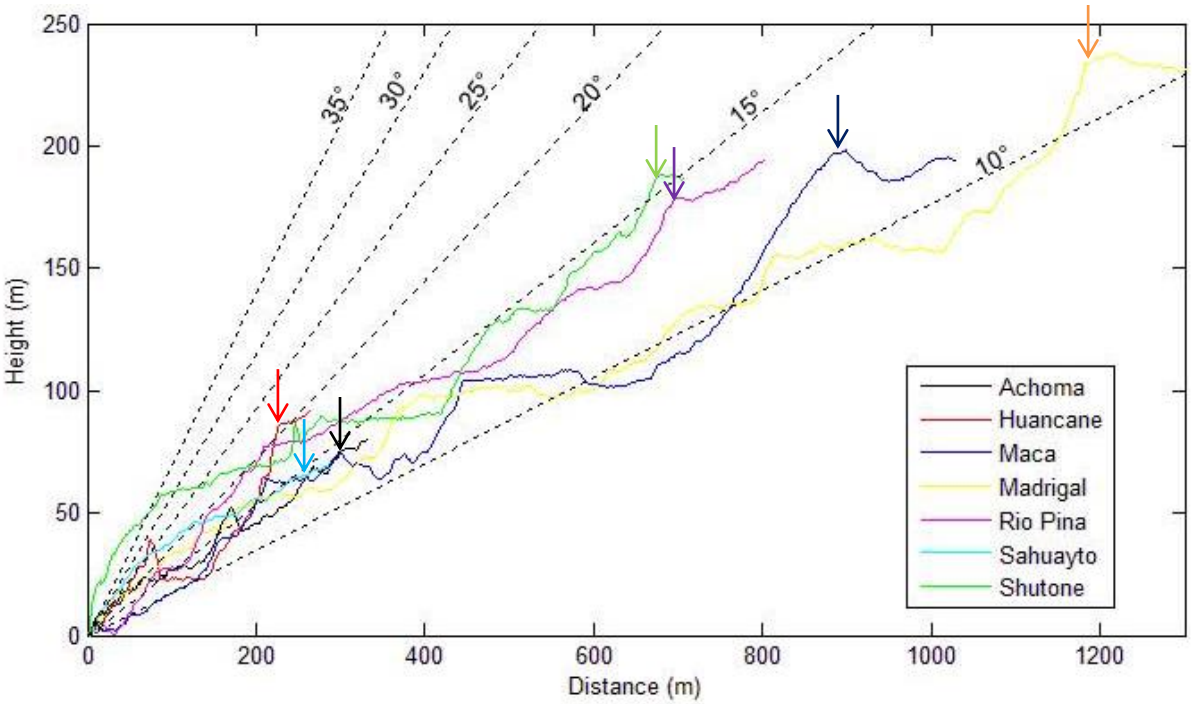

Figure 23: Cross-sections of all landslides in the Colca valley, with in dashed lines slope envelopes. The arrows denote the headscarps of each landslide.

4.3.1 Horizontal displacement

The temporal pattern of displacement of all landslides shows that sliding reactivates nearest to the river and then spreads to the main scarp of the landslide (Figure 24 and 25). To a lesser extent this is true for the Rio Pina, which shows less variability in its main active landslide body.

The landslides Achoma, Maca, and Rio Pina show maximum cumulative displacement from March to July 2013, with little extra displacement afterwards. The other landslides show little displacement from March to April 2013, and then primary displacement until July 2013. Maximum cumulative displacement is reached in February 2014.

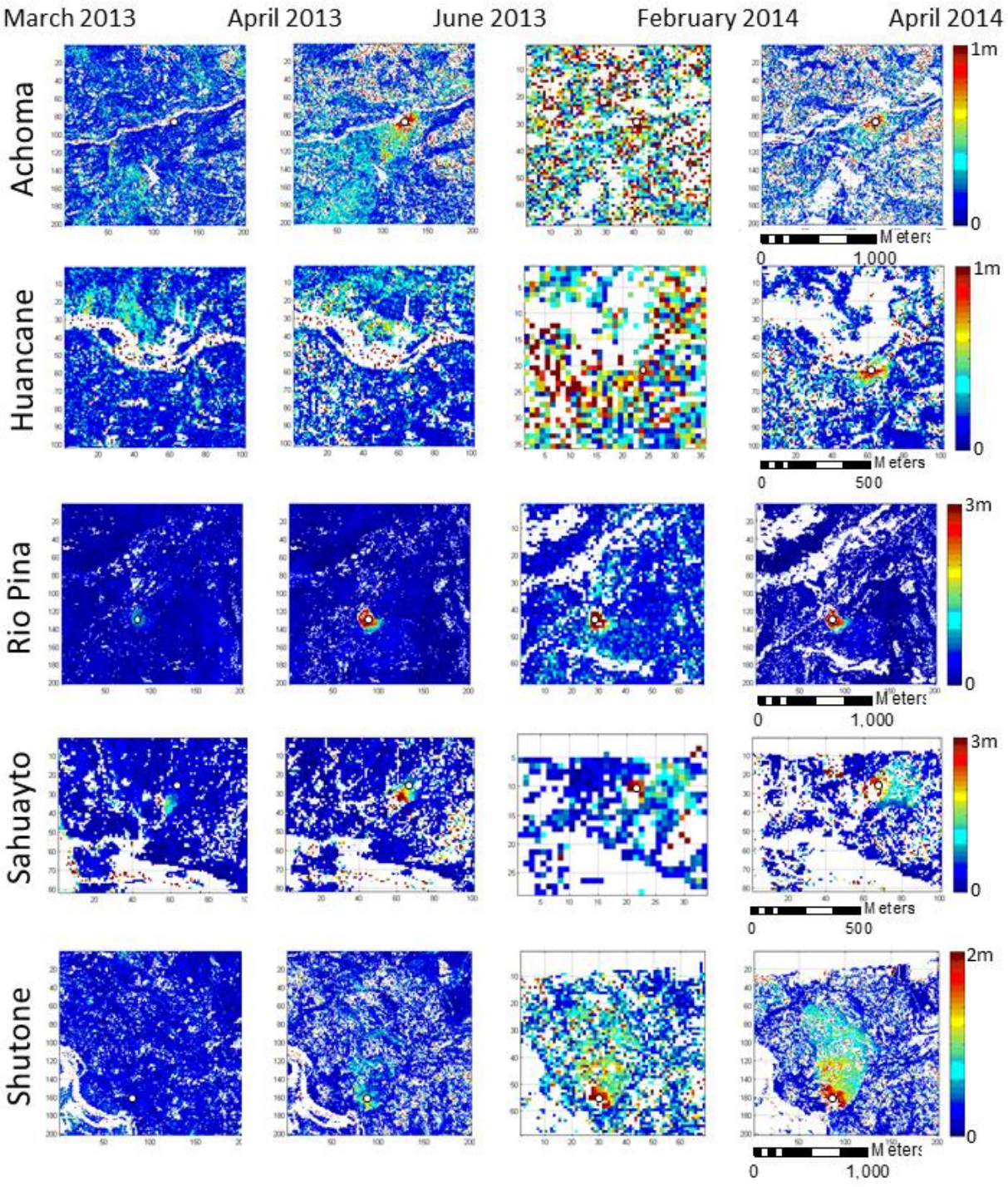

Figure 24: Time series of cumulative horizontal displacement from March 2013 to April 2013, July 2013, February 2014, and April 2014. A white point is on each landslide representing the point of horizontal displacement extracted from the landslide.

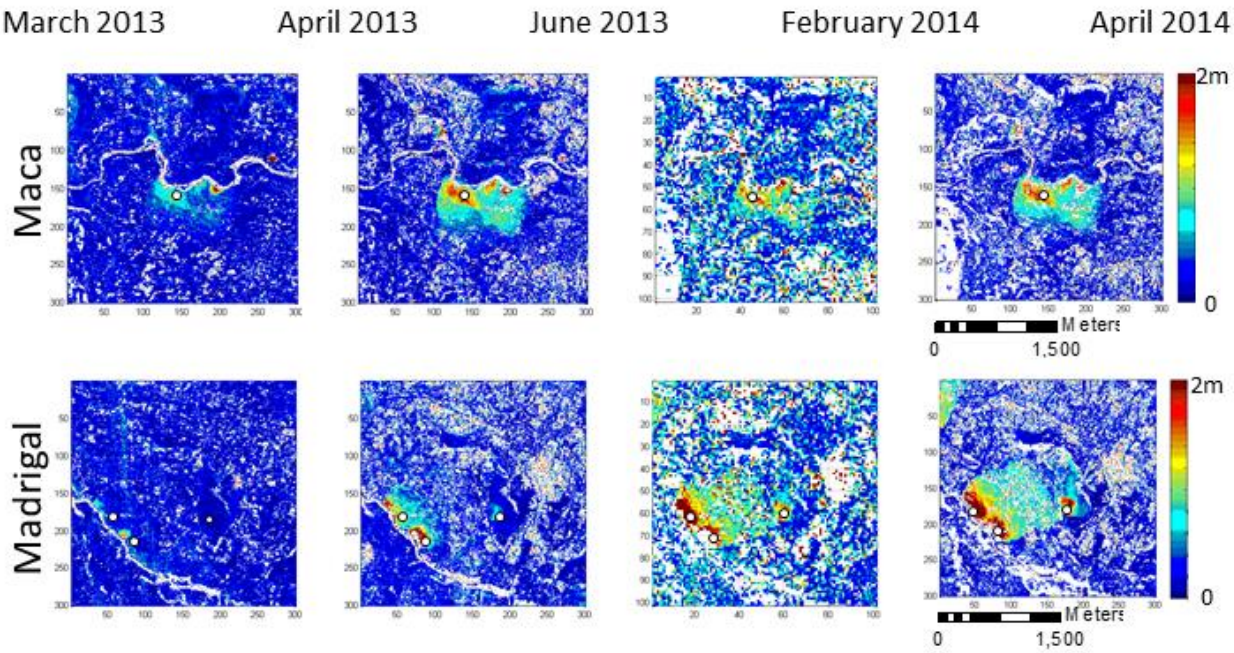

Figure 25: Time series of cumulative horizontal displacement of Maca and Madrigal from March 2013 to April 2013, July 2013, February 2014, and April 2014. A white point is on each landslide representing the point of horizontal displacement extracted from the landslide.

4.3.2 Characterization and classification of Maca and Madrigal

The landslides of Maca and Madrigal will be discussed in detail, concerning geomorphology and pattern of displacement.

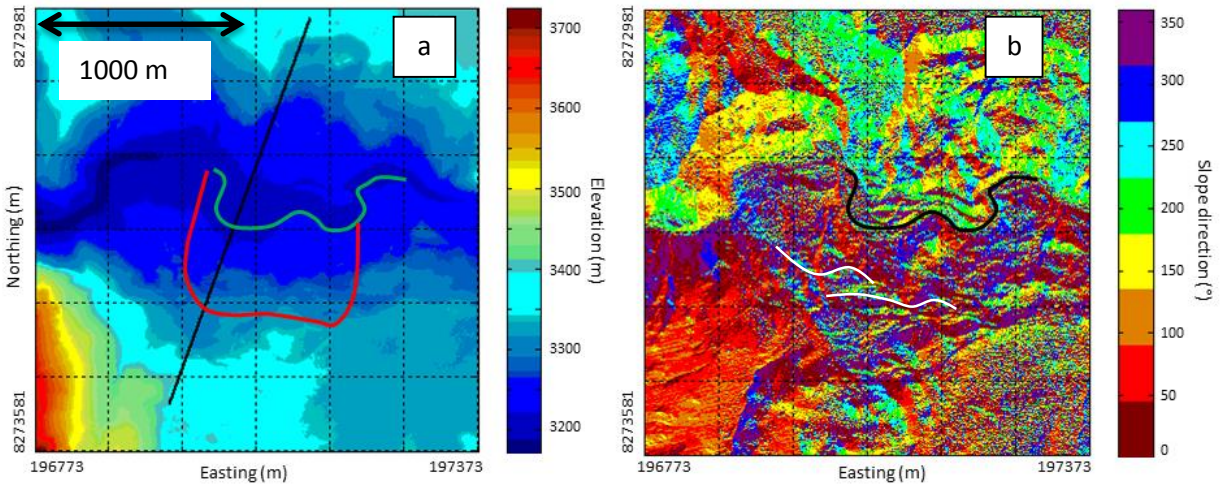

Figure 26: DTM of March 2013 of the Maca landslide (a), with the location of the cross-section as a black line and the headscarp as a red line, and the aspect of the slope of the DTM (b), with 0° and 360° located north. Examples of counterslopes accentuated with white lines, river indicated with a blue and a black line.

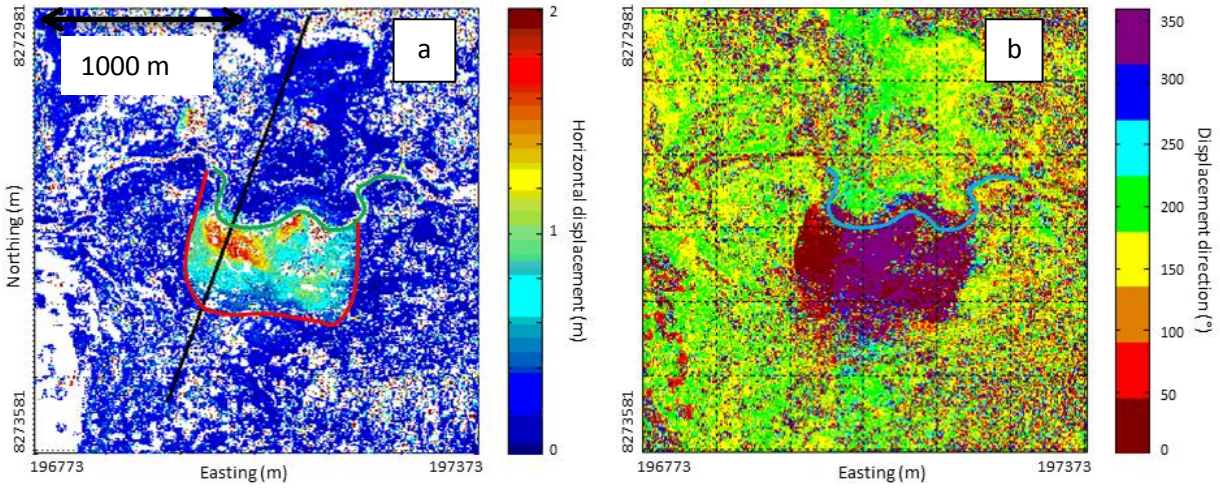

Figure 27: Displacement field (m) of Maca from March 2013 to April 2014 (a), with the location of the cross-section as a black line and the headscarp as a red line. The azimuth of displacement (°) of the Maca landslide (b), with 0° and 360° located north.

4.3.2.1 Maca

The aspect map of Maca (Figure 26b) shows large counterscarps, which have an aspect opposite to the main aspect of the landslide, but show the same direction of movement as the landslide. Several counterscarps are present on the cross-section on the landslide (Figure 28a), which shows something very similar to a horst and graben structure. A different kind of counterscarp has been observed in the field, displaying rotational features. The cross-section of Maca shows a highly irregular surface with height differences of approximately 10 m on a distance of approximately 200 m.

On the opposite bank of the river at the village of Lari a fifty years old landslide is present of which the shape is still clearly distinguishable in both the DTM and the aspect map (Figure 26). The Lari landslide has not shown any activity during the satellite acquisition, except for small areas that have decorrelated and are not visible on the displacement map.

Due to the shape of the landslide and the horst and graben structures found on the Maca landslide, this landslide is classified as mainly a soil spread with rotational parts.

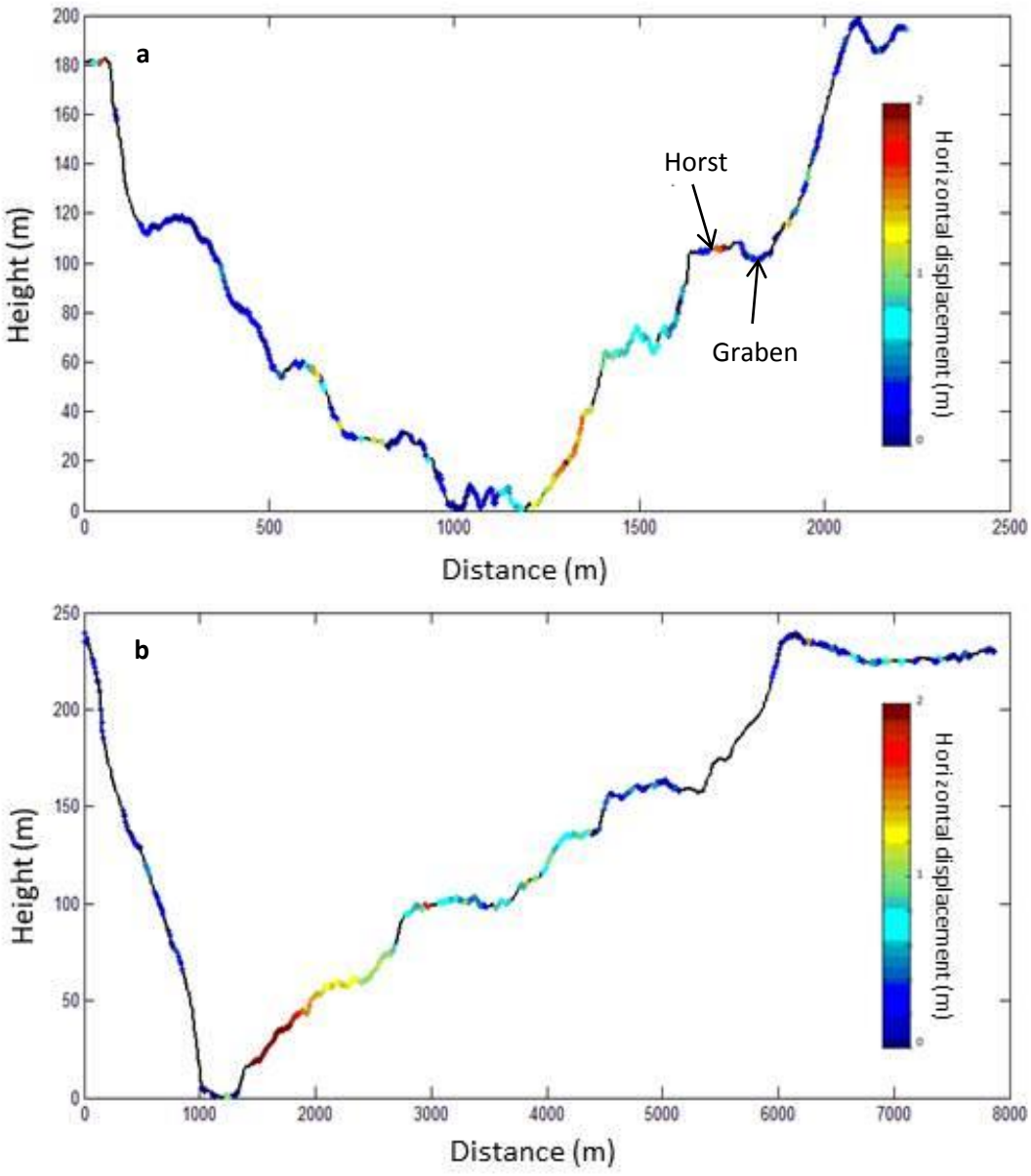

Figure 28: Cross-sections of the Maca (a) and Madrigal (b) landslides, with horizontal displacement plotted on top of the elevation data.

Something peculiar is the matter with the displacement pattern at the Maca landslide. The displacement of this landslide is not just on the southern bank of the river, but has spread to the northern bank of the river as well (Figure 27a). The direction of displacement on the northern bank of the river is the same as on the southern bank of the river (Figure 27b), suggesting that the displacement is part of the Maca landslide, although being on the opposite side of the river. This expanding of displacement to across the river is not found in any of the other landslides and is significant when compared to the accuracy.

4.3.2.2 Madrigal

The main landslide body of Madrigal shows some counterscarps, which are less pronounced than those of the Maca landslide (Figure 29b). At the main scarp of the landslide a smaller landslide block is

present, which has the largest counterscarp in the Madrigal landslide. The roughness of the landslide (Figure 28b) is similar to that of the Maca landslide. There is no expanding of the landslide across the river, because the opposite bank is very steep and likely of a more competent geology (Figure 28).

The Madrigal landslide shows similar displacement patterns as the Maca landslide (Figure 30a), with the highest displacements nearest to the river. The smaller landslide body shows a different direction of movement, which is nearly perpendicular to the main landslide body. As this movement is still downslope and into the main body of the landslide the smaller landslide is considered a part of the Madrigal landslide.

The detailed geology of the Madrigal landslide is unknown and its geomorphology is very similar to the Maca landslide. Therefore it is classified as a soil spread with rotational parts as well, of which the dominant mechanism is unknown.

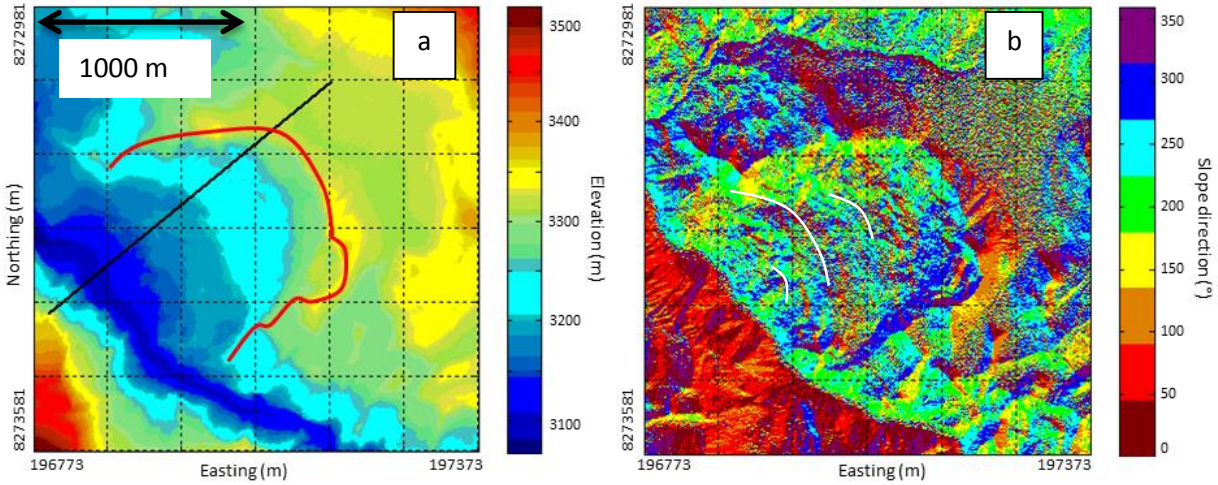

Figure 29: DTM of March 2013 of the Madrigal landslide (a), with the location of the cross-section as a black line and the headscarp as a red line, and the aspect of the slope of the DTM (b), with 0° and 360° located north. Examples of counterscarps indicated with white lines.

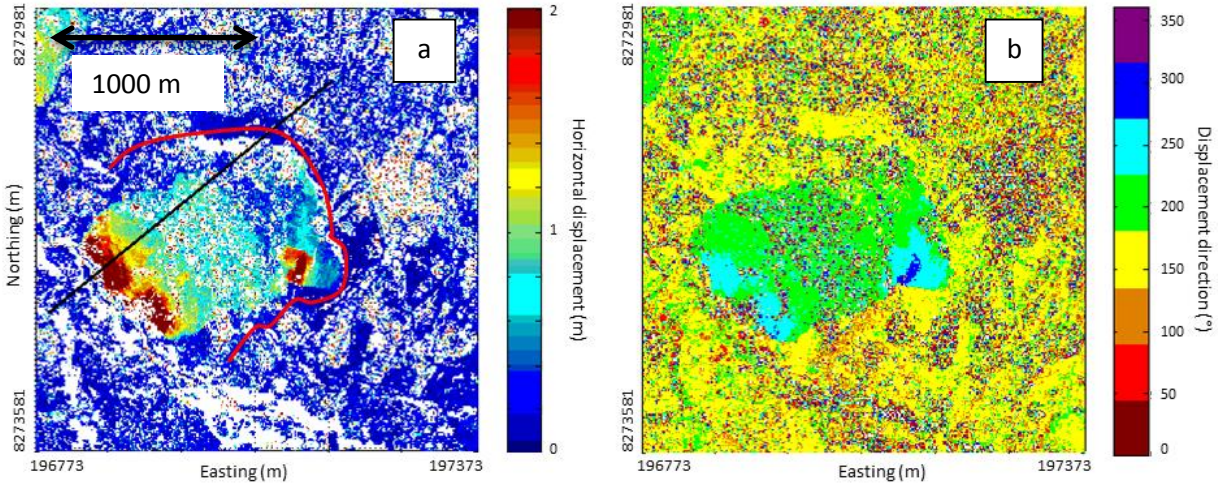

Figure 30: Displacement field (m) of Madrigal from March 2013 to April 2014 (a), with the location of the cross-section as a black line and the headscarp as a red line. The azimuth of displacement (°) of the Madrigal landslide (b), with 0° and 360° located north. The pixels are 8m.

5. Discussion

5.1 DTM

An accuracy of ±60 – 80 cm is better than the accuracies found for the Pléiades DEMs in Berthier et al. (2014), for a region without vegetation and with low slopes. Whether this accuracy is sufficient to remove all topographic and sensor distortions before correlation will be determined by the accuracy of the displacement maps.

Unfortunately the DTM of April 2013 includes an undulation in its elevation data, of which the removal was unsuccessful. For continued research it would be beneficial to remove the error to further improve results achieved with this DTM.

The accuracy of DTMs improves with a higher B/H ratio (Bernard et al. 2012; Poli et al. 2013). However, in the Colca valley several steep cliffs are present in the transition of terraces, which cause problems in the DTMs. The steeper the slope of the DTM is, the more inaccurate the result of interpolation becomes, which is more true for higher B/H ratios that lower. Therefore, in all the results that have been produced using interpolated DTMs the inaccurate areas of interpolation have been masked, to avoid values that are not based on reality. A downside of this procedure is that the elevation changes under steep slopes cannot be accounted for. This means that any valuable information on the changes in elevation near the scarps of landslides is lost.

5.2 Correlation

The displacement measured by correlation satellite imagery has resulted in both significant displacement for correlations between Pléiades images and for correlations between a Pléiades image and SPOT6 image. Also, the displacement compares very well with the displacements measured by GPS, with deviations of 2 cm from the simple method. However, while the weighted method shows displacement that do not compare as well with GPS displacement, its errors are only slightly higher (±6 cm) than those of the simple method. Combinations of multiple deformation maps have been demonstrated to work for large InSAR data-sets (Schmidt & Bürgmann 2003; Doin et al. 2012), with a result that smooths the time-series and reduces errors. Thus, the weighted method needs more research to make the displacements yielded by it more representative of real displacements and include more information into the deformation fields.

Displacement computed from Pléiades imagery has accuracies of approximately 15 cm (~1/5 of a pixel). Correlations between Pléiades imagery and imagery of the SPOT6 satellite results in displacement accuracies of approximately 30 cm (~1/5 of a pixel). These displacements are significant for all landslides. However the Huancane landslide has displacements that are so low that the errors in displacement obscure its pattern of displacement (Figure 31), although the displacement itself is significant.

In addition to the lower accuracy of correlations with the SPOT6 image, there are other drawbacks to the displacement maps sourced by the SPOT6 image. There is a lower resolution available, which yields less details to study the landslides, and there is more noise present, that causes more information to be

lost. But the advantage of having an extra point in time to enhance the detail of temporal displacement and the fact that the displacements computed are still significant outweighs these drawbacks.

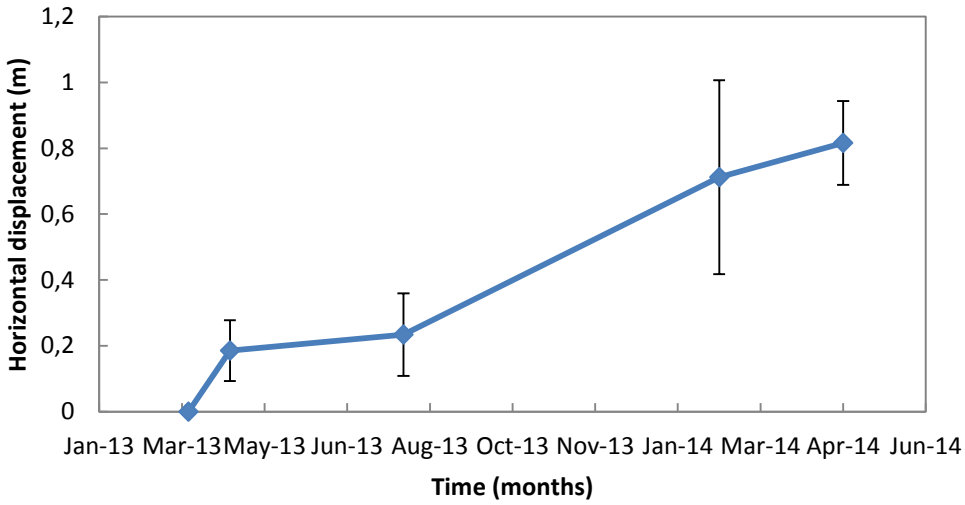

Figure 31: Cumulative displacement of the Huancane landslide, with the NMAD of each displacement map as error bars.

Orthoimages spanning 13 months have been correlated. Accuracies seem to diminish slightly with time, but this relationship is not clear for every landslide and the lower accuracy of the SPOT6 displacement maps obscures the relationship (Figure 24 and 25). Moreover, these diminishments are sufficiently small that all displacements can be considered highly significant.

For all images little noise is present on the slopes of the valley. However, substantial amounts of noise are present at the flat parts of the valley due to vegetation, as there is agriculture practiced at the flat areas and not on the slopes. For correlations of the Pléiades imagery this noise increases from the correlation of imagery spanning one month to that spanning thirteen months, as the vegetation changes more over time (Figure 16c). Correlations with the SPOT6 do not show this trend for reasons discussed above. In future research such a trend could be extracted.

5.3 Characterization

5.3.1 Geomorphology

Most of the landslides show the highest displacement near the bottom of the slope. This behavior has also been observed in other landslides that occur in lacustrine sediments (Jongmans et al. 2009; Handwerger et al. 2013). In the case of the landslide described in Jongmans et al. (2009) it was found that the increased velocities at the bottom of the landslides were the cause of a forced thinning of the landslide, due to a paleotopographic ridge (Bièvre et al. 2011). It is suspected that the landslides in the Colca valley that occur in lacustrine deposits, also experience thinning of the landslides bodies, which causes the velocity to increase in order to maintain the volume of material that is transported downslope. A possible explanation is that the material at the bottom of the slope is being eroded by the river.

An attempt has been made to find a relationship between the slope or the area of a landslide and the mean or maximum displacement of that landslide (Figure 32). However, clear trends are not discernible and it seems that the magnitude of displacement of landslides is not dependent on either slope or area.

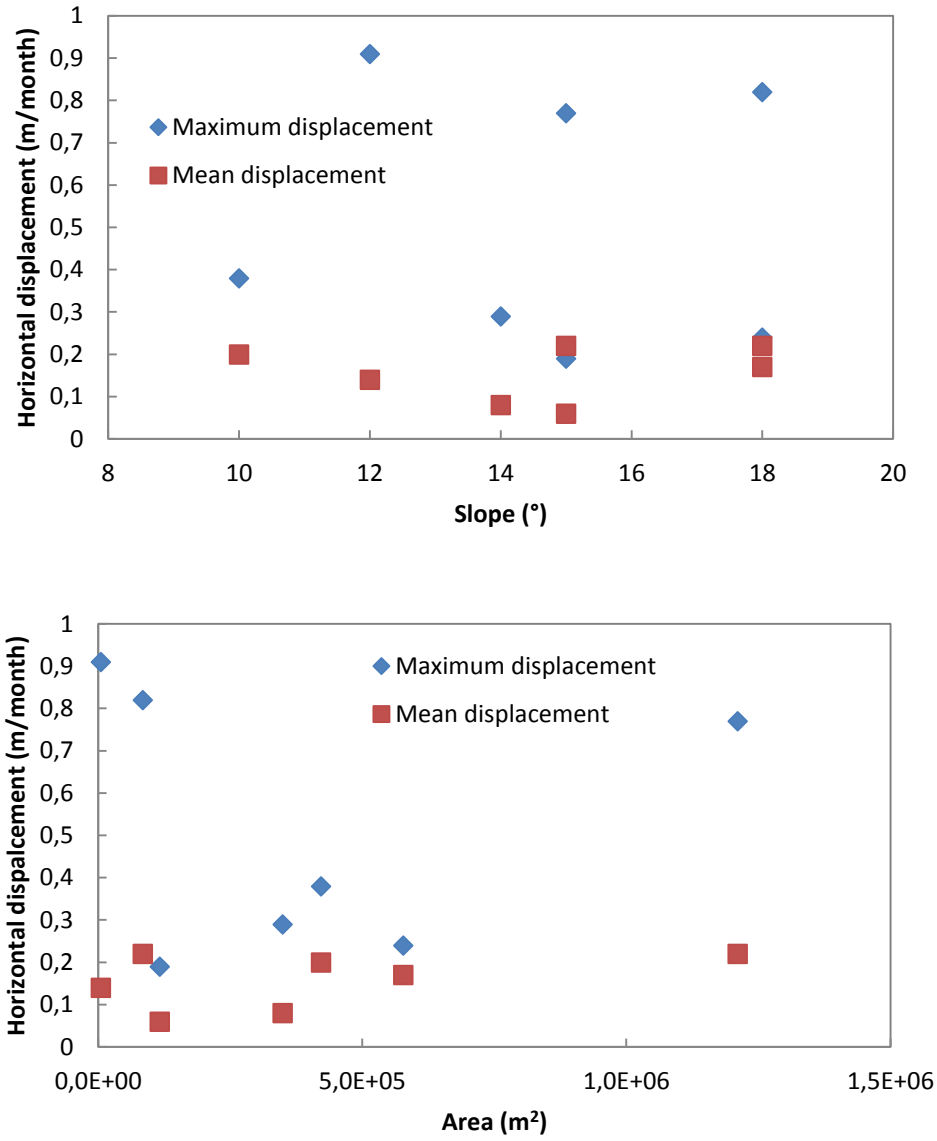

Figure 32: Horizontal displacement versus slope (a) and area (b), for all the landslides.

The Rio Pina landslide shows the highest displacement near the bottom of the slope not in a spectrum of displacement rates but rather as a homogeneous block. This difference is may have been caused by the different geology present at the Rio Pina landslide, that lies in volcanic ignimbrites.

The Maca landslide shows an irregular surface with counterscarps and blocks that suggest a horst and graben structure. This structure has also been observed in the field. Horst and graben structures are part of a feature that is spreading, usually caused by a competent layer overlaying a weak layer (Hungr 1995;

Cruden & Varnes 1996). In the case of Maca there is a competent alluvial conglomerate layer overlaying unconsolidated lacustrine sediments. Therefore it is thought that the mechanism most important for landsliding at the Maca landslides is lateral spreading (Cruden and Varnes, 1996). However, due to the shape of parts of the landslide (Figure 20) it is probable there are also rotationally moving parts present.

The sliding surface of the Maca landslide extends to the northern bank of the river, which is visible in the displacement map (Figure 33b). Four additional cross-sections have been made on the landslide to study the displacement on the northern riverbank further (Figure 34). The first observation that will be made is geomorphological. Outlined in blue in Figure 35 is the northern riverbank that has a low elevation, low mean slope, and on which several channels are visible with elevation differences of 5-7 meters (Figure 34), that are probably a result of high water in the river that overflows this part of the bank. Outlined in red are the parts of the northern riverbank that are displaced from March 2013 to April 2014. The western displaced part is well delimitated with a scarp-like feature, suggesting that this part is separate from the rest of the northern riverbank.

The phenomenon may be a consequence of the Lari landslide opposite from the Maca landslide, which has forced the river to flow closer to the Maca landslide approximately fifty years ago. A plausible theory is that a slip surface of the Maca landslide is deeper than the river and surfaces on the northern bank (Figure 35a).

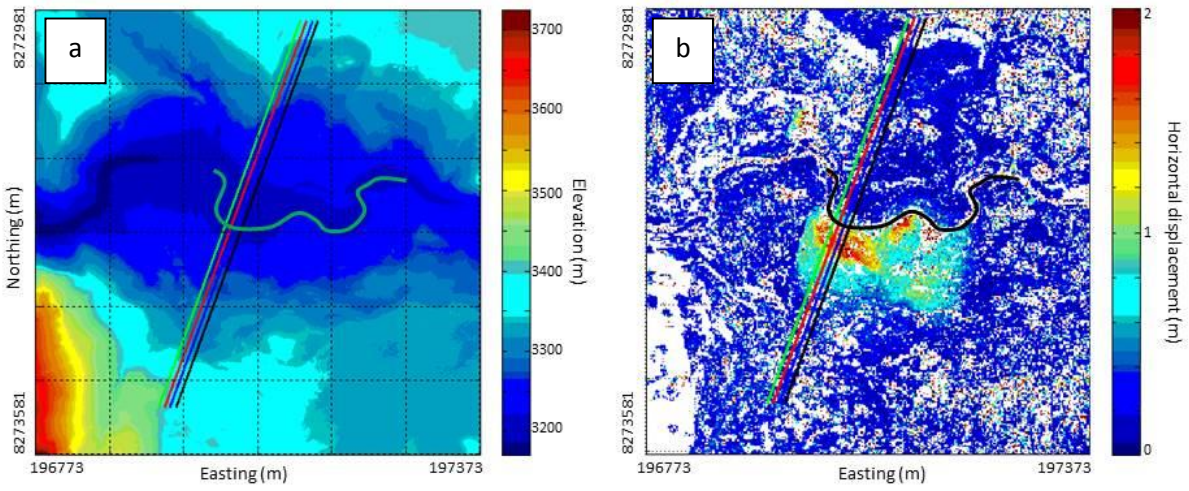

Figure 33: a) DTM of March 2013, and b) the displacement map of March 2013 to April 2014 of the Maca landslide. Four additional cross-sections have been indicated on the part of the landslide that extends across the river.

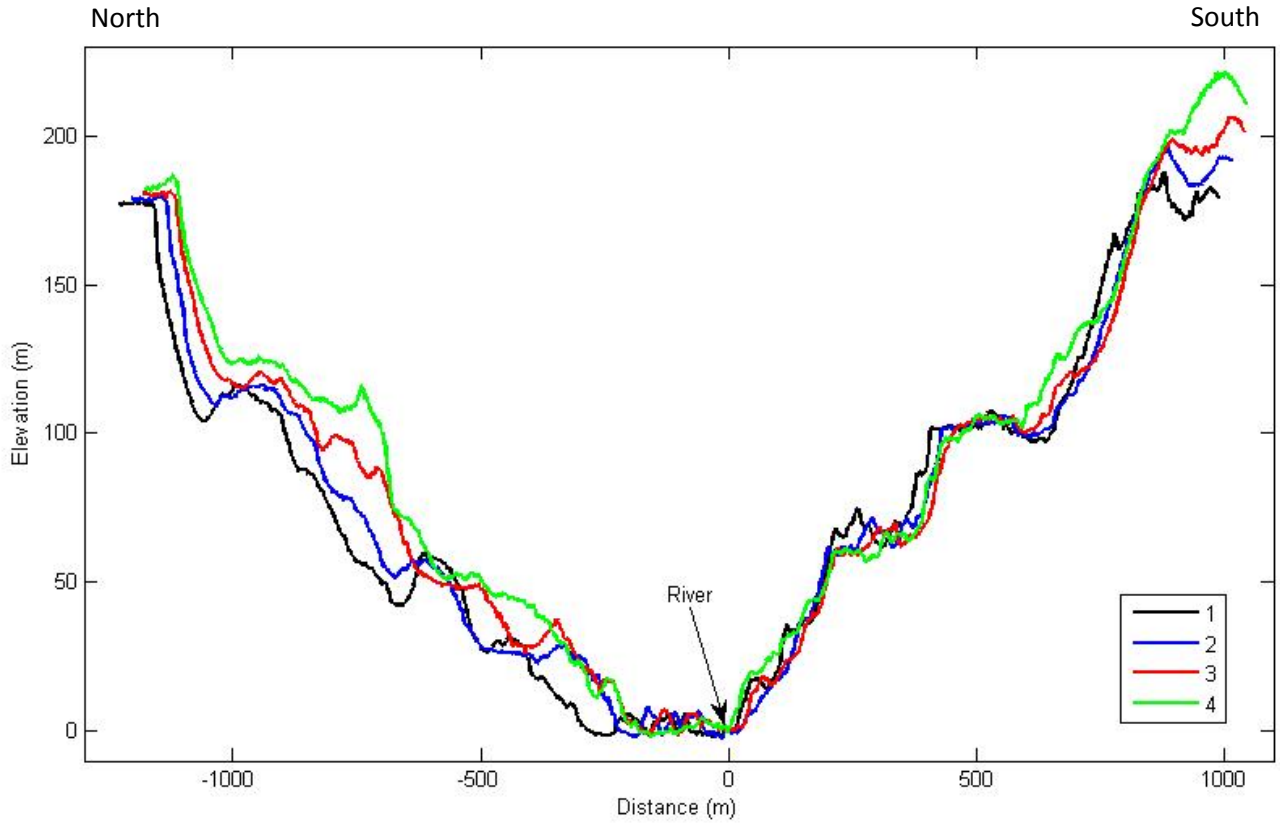

Figure 34: Additional four cross-sections of the March 2013 DTM of the Maca landslide. The colors correspond to the cross-sections visible in Figure 33.

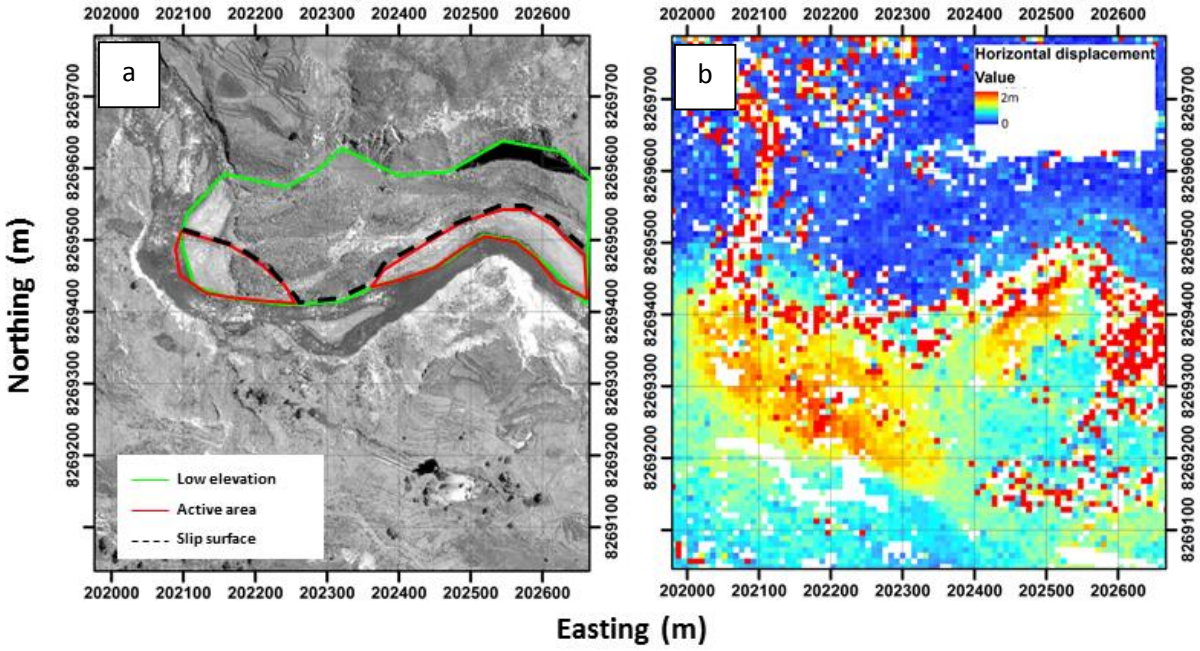

Figure 35: Comparison between the orthoimage (a) and displacement map of March 2013 to April 2014 (b).

The Madrigal landslide has a more regular round shape than the Maca landslide, except for the smaller landslide at the side of the scarp. The round shape of the headscarp of the Madrigal landslide suggests a rotational slide. However, the counterscarps and pattern of displacement are identical to those of the Maca landslide, which indicated spreading there.

5.3.2 Kinematics

On each landslide one point with little vegetation and high displacement has been selected (Figure 24 and 25) and three points on the landslide of Madrigal because three main areas of movement are present. The displacement of these pixels has been plotted (Figure 36). Most of the curves display realistic displacements in the sense that the cumulative motion is always increasing with time. On the contrary, the Achoma, Rio Pina, and Maca landslides show retractive displacements (Figure 36). These retractive movements are fictional results, as no such movements have been reported in the area and are unlikely to occur there. The retractions mostly occur around the February 2014 acquisition by SPOT6 and could therefore be a result of the inaccuracies found in the displacement map produced by the correlation with a lower resolution. In able to analyze the displacement rates of those landslides that show retractive movements, the SPOT6 data of these landslides have been removed (Figure 37).

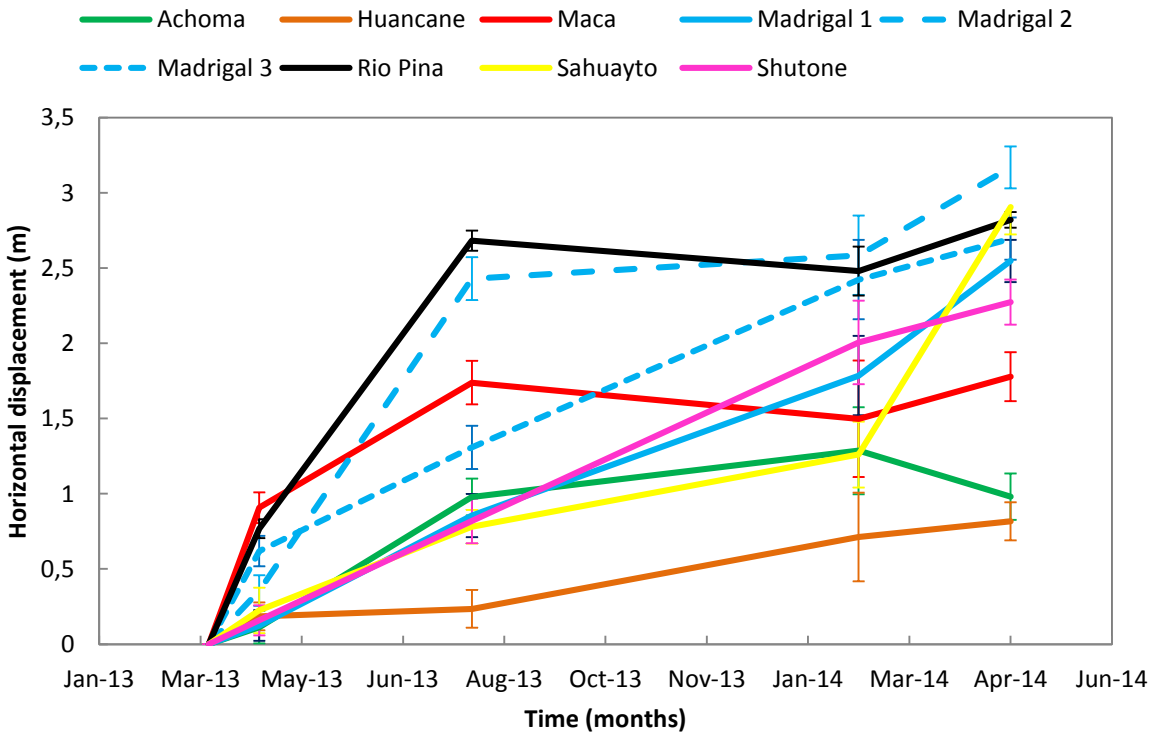

Figure 36: Horizontal displacements for all landslides, with the landslides of Achoma, Maca, and Rio Pina showing retractive movements.

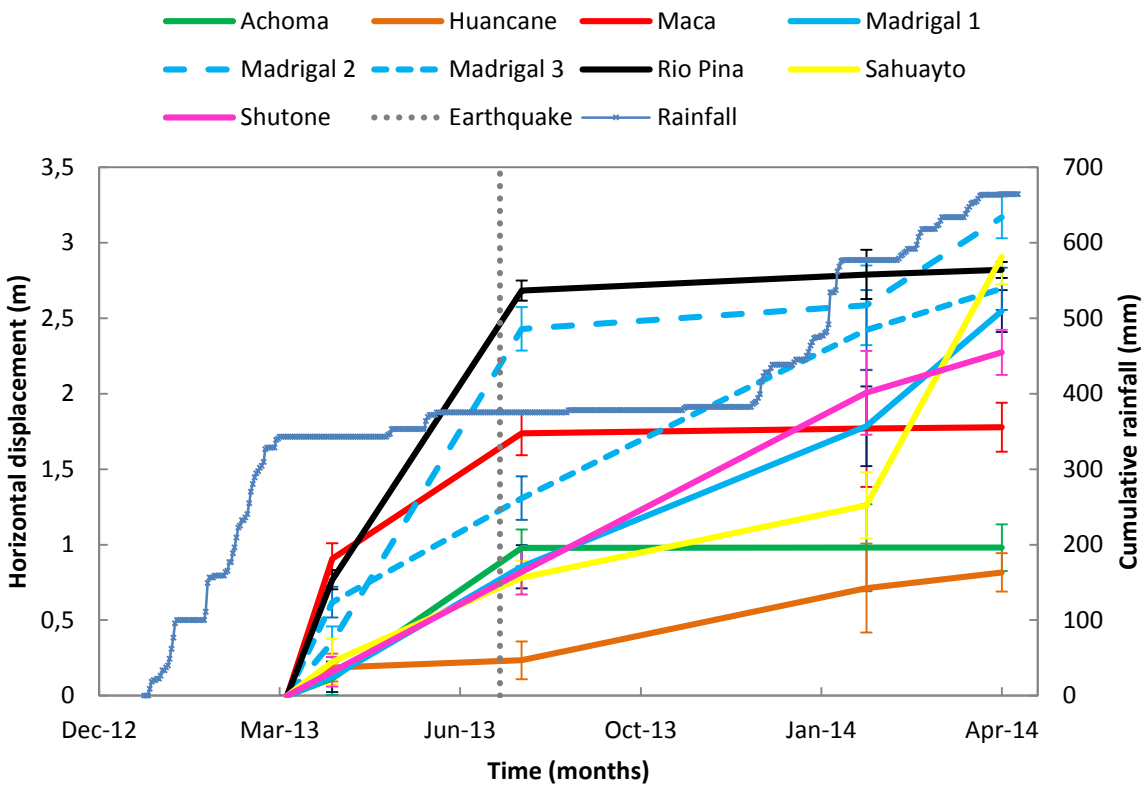

Figure 37: Horizontal displacement of a pixel on each landslide, and three on the Madrigal slide. The pixels have been selected where little vegetation and maximum displacement is present. The error bars represent the NMAD of each displacement field. SPOT6 data of the Achoma, Rio Pina, and Maca landslides has been removed.

Figure 37 shows that all landslides have displacement during and after the first rainy season. The landslides of Achoma, Maca, and Rio Pina move very little after July 2013 and do not react to the second rainy season. The other landslides either continue moving during the dry season or reactivate in the second rainy season, even though there is less rainfall. Therefore two groups of landslides have been distinguished when comparing the displacements of all landslides together:

1) The first group exhibits high displacement values (1-2.5 m) during and after the first rainy season, but has come to a standstill from July 2013 until the last measurement. The landslides belonging to this group are Achoma, Maca, and Rio Pina.

2) The other group shows displacement due to both rainy seasons, with high displacement (max. 2.5 m) in the rainy season of 2012-2013 and lower displacement (max. 2 m) in the rainy season of 2013-2014. The three landslides classified to this group are the landslides of Shutone, Sahuayto, and Madrigal.

The landslide of Huancane is not assigned to a group, as the error margins are quite large compared to the movement.

Visual inspection of Figure 37 indicates that all landslides move due to rainfall, because the cumulative displacement of the landslides mirrors the increase in cumulative rainfall with a delay of several weeks

to months. To make a connection that is sound it has been attempted to correlate cumulative landslide displacements (X) and cumulative rainfall (Y) 0-5 months prior to the acquisition date (Figure 38). The correlation coefficient has been calculated with the following equation:

$$C(X,Y) = \frac{\sum(x-\bar{x})(y-\bar{y})}{\sqrt{\sum(x-\bar{x})^2 \sum(y-\bar{y})^2}}$$

Again the landslides are divided into two groups; one with a high correlation with monthly cumulative rainfall of 4 months before and one with a high correlation with monthly cumulative rainfall of 1 month before. Once more, the landslides that belong to the second group are mostly found in the northwestern corner; Huancane, Madrigal, Sahuayto and Shutone. However, especially the second group shows high correlation values with rainfall of any time period, which makes the significance of all correlations questionable.

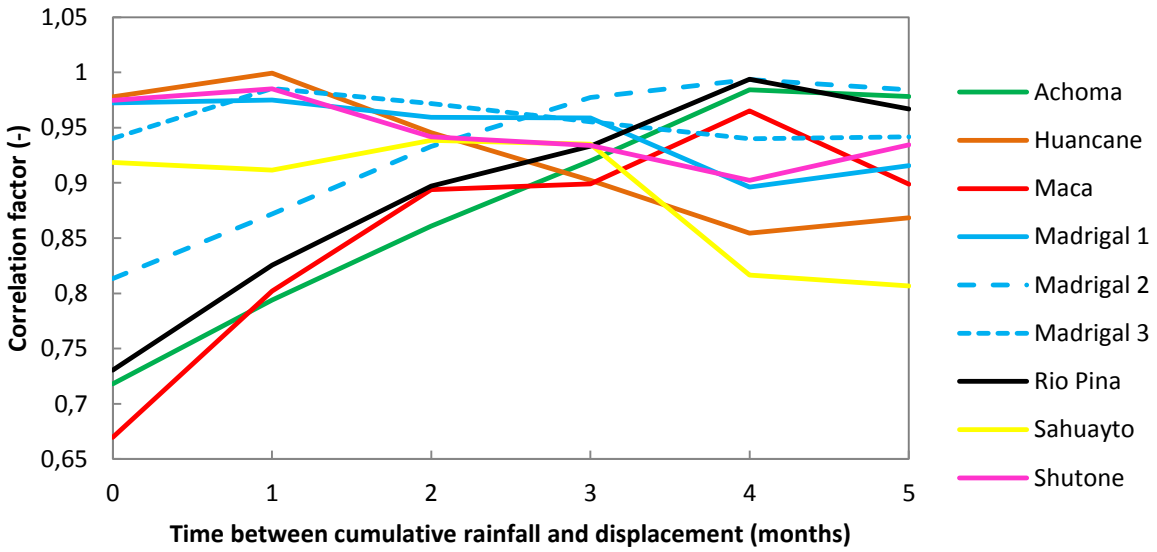

Figure 38: Correlation factors of the correlations between displacements of all landslides and cumulative rainfall of 0-5 months prior.

Whether or not the landslides can be correlated to very recent or older amounts of rainfall, the fact that they are forced by rainfall is clear. All landslides show high displacement due to the rainy season of 2012-2013, while only three landslides show the same behavior due to the rainy season of 2013-2014. The division of the landslides into two groups is caused by a difference in sensitivity to rainfall. The consequence of a low sensitivity to rainfall is little displacement due to the low rainfall amounts in the rainy season of 2013-2014, which has 300 mm of rainfall compared to 500 mm of rainfall in the rainy season of 2012-2013. Landslides that are more sensitive to rainfall display displacement in both rainy seasons, with lower displacements in the second rainy season compared to the first due to lower rainfall amounts.

Several reasons can be offered to explain the difference in sensitivity to rainfall in the two landslide groups. Firstly an observation will be made; all landslides that show increased sensitivity to rainfall are

placed in the northwestern region of the studied area (Figure 17). With this observation two theories on the cause of sensitivity variability can be argued.

On the 17th of July 2013 a shallow earthquake occurred to the south-west of the village of Maca at approximately 21 km distance (Figure 39 and 38), with a magnitude of M_w 6.0. The earthquake occurred closest to the landslides in the northwestern area of the image and farther away from the other landslides (Table 8). Earthquake waves affect landslides that are closer more strongly, because they attenuate away from their source (Meunier et al. 2013). It is assumed that the earthquake reactivated landslides at least until the Maca landslide, as displacement has been measured here (Lacroix et al., 2014) and co-seismic slip is observed on the Maca landslide (Figure 39), where 2 cm of earthquake induced slip occurred (Lacroix et al., 2014). For landslides closer to the earthquake the displacement could have caused cracks to form in the landslide body, through which rainwater could infiltrate and destabilize landslides more easily. The Maca landslide did not experience the forming of cracks, but rather than destabilization there may have even been a stabilization of landslides, because the small displacement expelled excess moisture.

A shortcoming of this theory is the lack of data. There is no data available on the displacement triggered by the earthquake that occurred on the landslides other than the Maca landslide. There is only speculation on the response that may have happened.

Another explanation of the variability in sensitivity can be found in the geology of the lacustrine sediments of the Colca valley. The paleolake that existed until 0.61 Ma stretched from the town of Pinchollo, where the valley was dammed, to the town of Yanque, where the lake was fed by the Rio Colca (Figure 40). Sediment was transported by the river and deposited in the low energy environment of the lake. Close to Yanque this sediment is courser than close to Pinchollo, as the water near Yanque had residual energy from the Rio Colca to carry the finer sediments further into the lake (Figure 40). It follows that the landslides that show increased sensitivity to rainfall might be in finer sediments than the landslides with decreased sensitivity. As grain-size has a great impact on the mobility of landslides (Wang & Sassa 2003) it can be assumed that the finer grain-size of lacustrine sediment near Pinchollo has greater sensitivity to rainfall.

Again, the shortcoming of this theory is the lack of data, as the exact differences in grain-size throughout the valley are unknown and other phenomena (side-rivers and thalwegs) could influence the grain-size distribution of lacustrine sediments.

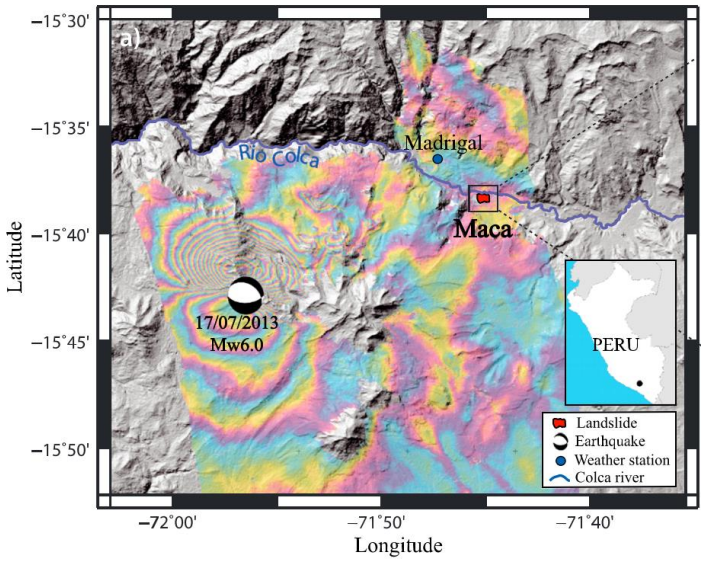

Figure 39: Map of the Colca valley, with the deformation field produced by the 17 July 2013 earthquake represented in color levels based on an InSAR of TerraSAR-X data (Copyright Deutches Zentrum für Luft-und Raumfahrt 2013). Each color fringe circle represents 1.6 cm change in the line of sight between the satellite and the surface. After Lacroix et al. (2014).

Table 8: Distance from the earthquake on July 17th, 2013, for the point on each landslide on which displacements have been calculated. The landslide highlighted in green have a high sensitivity to rainfall, the landslides highlighted in red have a lower sensitivity, and the Huancane landslide does not display a pattern that is distinct enough.

Landslide	Distance from earthquake (m)
Shutone	17520
Madrigal	17387
Sahuayto	17373
Maca	20521
Huancane	22270
Achoma	27755
Rio Pina	26619

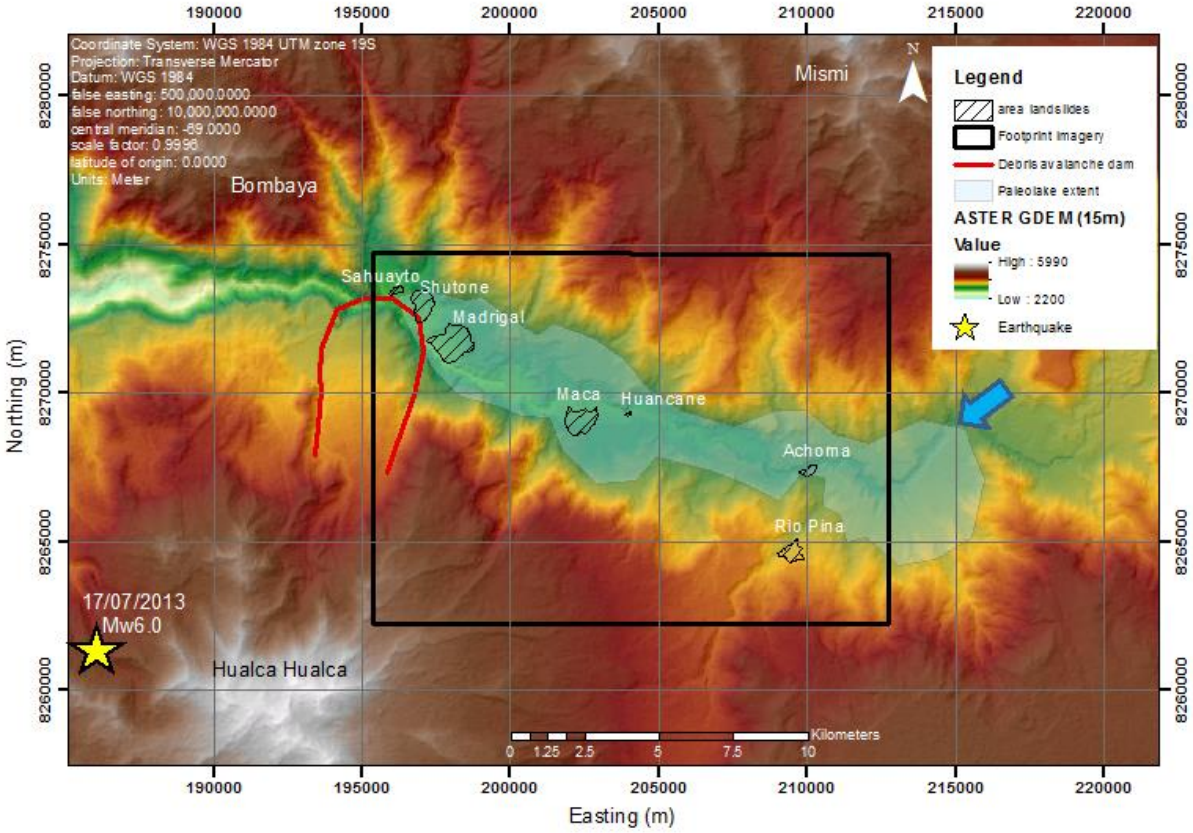

Figure 40: Overview of the Colca valley with the paleolake that drained in 0.61 Ma in the Colca valley, the river mouth in the East and the dam in the West.

To improve the displacement computed by the correlation of orthoimages the time-resolution of acquisitions must be improved. As it is now, the first rainy season (December-March, 2012-2013) is badly separated from the earthquake that takes place in the dry season (July 17th, 2013), while it should be possible to eliminate all rainfall effects because the earthquake took place in the dry season. The second rainy season is badly separated from the dry season, which distorts displacements that could have taken place in the dry season. A weighted method of all ten displacement maps could provide improvement here as well.

6. Conclusions

First conclusions of the methodology will be given, then conclusions of the main research question.

The methodology is well-suited to manage this problem. The DTMs have accuracies of ±70 cm, while 2-11.7% of the data is lacking, depending on the B/H ratio. Also, an undulation is present in one of these DTMs, which is the result of instrumental problems during acquisition. This is probably a singular incident, but when such errors are encountered they should preferably be removed before attempting further research.

The displacement maps show that the most noise is found at the places that have variable vegetation, such as agriculture. Also errors caused by the cartography of the focal plane are visible in the displacement maps, which signifies the importance of having accurate DTMs with the least amount of errors possible. Otherwise, the accuracy of the displacements is very good, with NMADs between 0.06 and 0.15 m for correlations between Pléiades images and 0.20 to 0.44 m for correlations with the SPOT6 image. This shows that correlating with imagery that has a different source is viable, although the lower resolution will yield lower accuracies in displacement. Also, the comparison with the permanent GPS shows that the displacement calculated by correlation is representative of the displacement found on at least one landslide.

All landslides in lacustrine sediments show increasingly high displacement rates near the toe of the landslide. This may be an effect of thinning of the landslide body towards the bottom of the slope, with the cause of this removal of material by the river. The Rio Pina landslide, which lies in ignimbrites, shows this pattern to a lesser extent, having a more homogeneous displacement rate in the main landslide body.

The areas of all the landslides range from 0.02-1.2 km^2, with the largest areas found in the northwestern part of the Colca valley. Otherwise all the landslides share slopes that range from 10° to 15°.

The Maca and Madrigal landslides have been studied in detail. The Maca landslide has been classified as a soil spread with rotational features. Even more, there is displacement of the landslide visible on the northern bank of the river. This could be an effect of a boundary between the Lari and Maca landslides that is not defined by the river, but by a fault between the two landslides, while the river has moved on top of the Maca landslide. The Madrigal landslide may be classified as a soil spread with rotational features as well, but more data should be collected on this landslide before a more definitive classification can be made.

In all the landslide two different sensitivities to rainfall have been observed. The landslides that appear less sensitive to rainfall react to the rainy season of 2013-2013, but not to the next rainy season that has a lower amount of cumulative rainfall. The landslides that appear more sensitive react to both rainy seasons. All landslides that have a higher sensitivity are found in the northwestern part of the Colca valley. Two explanations have been offered:

- Seismicity. On the 17th of July there was an earthquake with a magnitude of 6.0 M_w that was closer to the northwestern landslides than to the other ones. This could have caused cracks in

the northwestern landslides that would have made them more susceptible to rainfall. The other landslides may have been stabilized by expelling water from the landslide bodies.

- Lithology. The northwestern landslides all lie in sediments that were deposited near the dam of the paleolake that existed until 0.61 Ma, where theoretically the finest sediments should have been deposited. Consequently the other landslides lie in courser sediments. This difference in lithology could cause differences in sensitivity to rainfall.

References

Bernard, M., Decluseau, D., Gabet, L., and Nonin, P. (2013). 3D capabilities of the Pleiades satellite. ISPRS – International Archives of the Photogrammetry, Remote Sensing and Spatial Information Sciences, XXXIX-B3 (September), pp.553-557.

Berthier, E., Vincent, C., Magnússon, E., Gunnlaugsson, Á.Þ., Pitte, P., Le Meur, E., Masiokas, M., Ruiz, L., Pálsson, F., Belart, J.M.C., and Wagnon, P. (2014). Glacier topography and elevation changes from Pléiades very high resolution stereo images. The Cryosphere Discussions, 8(5), pp.4849-4883.

Bièvre, G., Kniess, U., Jongmans, D., Pathier, E., Schwartz, S., van Westen, C.J., Villemin, T., Zumbo, V. (2011). Paleotopographic control of landslides in lacustrine deposits (Trièves plateau, French Western Alps). Geomorphology, 125(1), pp. 214-224.

Cruden, D.M. (1991). A simple definition of a landslide. Bulletin of the International Association of Engineering Geology, 43, pp. 27-29.

Cruden, D.M. and Varnes, D.L. (1996). Landslide types and processes. Special Report – National Research Council, Transportation Research Board, 247, pp. 36-75.

Doin, M., Guillaso, S., and Jolivet, R. (2012). Presentation of the small baseline NSBAS processing chain on a case example: the Etna deformation monitoring from 2003 to 2010 using Envisat data. Proceedings of the ESA “Fringe 2011 Workshop”, Frascati, Italy, 19-23 September 2011, pp. 19-23.

Falconi, L., Leoni, G., Arestegui, P.M. Puglisi, C., and Savini, S. (2013). Geomorphological processes and cultural heritages of Maca and Lari villages: an opportunity for sustainable tourism development in the Colca Valley, Province of Caylloma, Arequipa, South Peru. Landslide Science and Practice, 6, pp. 459-465.

Fraser, C.S. and Hanley, H.B. (2005). Bias-compensated RPCs for sensor orientation of high-resolution satellite imagery. Photogrammetric Engineering and Remote Sensing, 71(8), pp. 909-915.

Fraser, C.S., Dial, G., and Grodecki, J. (2006). Sensor orientation via RPCs. ISPRS Journal of Photogrammetry and Remote Sensing, 60(3), pp. 182-194.

Fruneau, B., Achache, J., and Delacourt, C. (1996). Observation and modelling of the Saint-Étienne-de-Tinée landslide using SAR interferometry. Tectonophysics, 265, pp. 181-190.

Handwerger, A.L., Roering, J.J., and Schmidt, D.A. (2013). Controls on the seasonal deformation of slow-moving landslides. Earth and Planetary Science Letters, 3377-378, pp. 239-247.

Herring T., King, R., and McClusky, S. (2010). GAMIT reference manual: GPS analysis and MIT, release 10.4.

Höhle, J. and Höhle, M. (2009). Accuracy assessment of digital elevation models by means of robust statistical methods. ISPRS Journal of Photogrammetry and Remote Sensing, 64(4), pp. 398-406.

Hungr, O. (1995). A model for the runout analysis of rapid flow slides, debris flows, and avalanches. Canadian Geotechnical Journal, 32(4), pp. 610-623.

Iverson, R. and Major, J. (1987). Rainfall, ground-water flow, and seasonal movement at Minor Creek landslide northwestern California: Physical interpretation of empirical relations. Geological Society of America Bulletin, 99, pp. 579-594.

Jacobsen, K. (2011). Characteristics of very high resolution optical satellites for topographic mapping. International Archives of the Photogrammetry, Remote Sensing and Spatial Information Sciences, 38(4), pp. 137-142.

Jongmans, D., Bièvre, G., Renalier, F., Schwartz, S., Beaurez, N., and Orengo, Y. (2009). Geophysical investigation of a large landslide in glaciolacustrine clays in the Trièves area (French Alps). Engineering Geology, 109(1-2), pp. 45-56.

Lacroix P., E. Berthier, E. Taipe, (in review), Seismic reactivation of landslides in the Colca valley, Peru, detected using Pléiades images. Remote Sensing Environment.

Lacroix, P., Perfettini, H., Taipe, E., and Guillier B. (2014). Coseismic and postseismic motion of a landslide: Observations, modeling, and analogy with tectonic faults. Geophysical Research Letters, 41, pp. 1-5.

Leprince, S., Barbot, S., Ayoub, F., and Avouac, J.P. (2007). Automatic and precise orthorectification, coregistration, and subpixel correlation of satellite images, application to ground deformation measurements. IEEE Transactions of Geoscience and Remote Sensing, 45(6), pp. 1529-1558.

Lucieer, A., Jong, S.M.D., and Turner, D. (2013). Mapping landslide displacements using Structure from Motion (SfM) and image correlation of multi-temporal UAV photography. Progress in Physical Geography, 38(1), pp. 97-116.

Meunier, P., Uchida, T., and Hovius, N. (2013). Landslide patterns reveal the sources of large earthquakes. Earth and Planetary Science letters, 363, pp. 27-33.

Nuth, C. and Kääb, A. (2011). Co-registration and bias corrections of satellite elevation data sets for quantifying glacier thickness change. The Cryosphere, 5(1), pp. 271-290.

Petley, D. (2012). Global patterns of loss of life from landslides. Geology, 40(10), pp. 927-930.

Poli, D. and Toutin, T. (2012). Review of developments in geometric modelling for high resolution satellite pushbroom sensors. The Photogrammetric Record, 27(137), pp. 58-73.

Poli, D., Remondino, F., Angiuli, E., and Agugiaro, G. (2013). Evaluation of Pleiades-1A triplet on Trento testfield. International Archives of the Photogrammetry, Remote Sensing and Spatial Information Sciences, XL-1/W1, pp. 21-24.

Schmidt, D.A. and Bürgmann, R. (2003). Time-dependent land uplift and subsidence in the Santa Clara valley, California, from a large interferometric synthetic aperture radar data set. Journal of Geophysical Research, 108, pp. 1-13.

Schulz, W.H., McKenna, J.P., Kibler, J.D. and Biavati, G. (2009). Relations between hydrology and velocity of a continuously moving landslide – evidence of pore-pressure feedback regulating landslide motion? Landslides, 6(3), pp. 181-190.

Stumpf, A., Malet, J.P., Allemand, P., and Ulrich, P. (2014). Surface reconstruction and landslide displacement measurements with Pléiades satellite image. ISPRS Journal of Photogrammetry and Remote Sensing, 95, pp. 1-12.

Thouret, J.C., Wörner, G., Gunnell, Y., Singer, B., Zhang, X., and Souriot, T. (2007). Geochronologic and stratigraphic constraints on canyon incision and Miocene uplift of the Central Andes in Peru. Earth and Planetary Science Letters, 263(3-4), pp. 151-166

Wang, G. and Sassa, K. (2003). Pore-pressure generation and movement of rainfall-induced landslides: Effects of grain size and fine-particle content. Engineering Geology, 69(1-2), pp. 109-125.

Zavala, B., Mariño, J., Lacroix, P., Taipe, E., Tatard, L., Benavente, C., Pari, W., Macedo, L., Peña, F., Fídel, L., Vilchez, M., Villacorta, S., Luque, G., Rosado, M., Antayhua, Y., Wathelet, M., Guillier, B., Bondoux, F., Norabuena, E., and Gomez, J. C. (2012). Evaluación de la seguridad física del distrito de Maca (p. 160).

Zerathe et al., (in review)

Appendix 1. Raw displacement maps

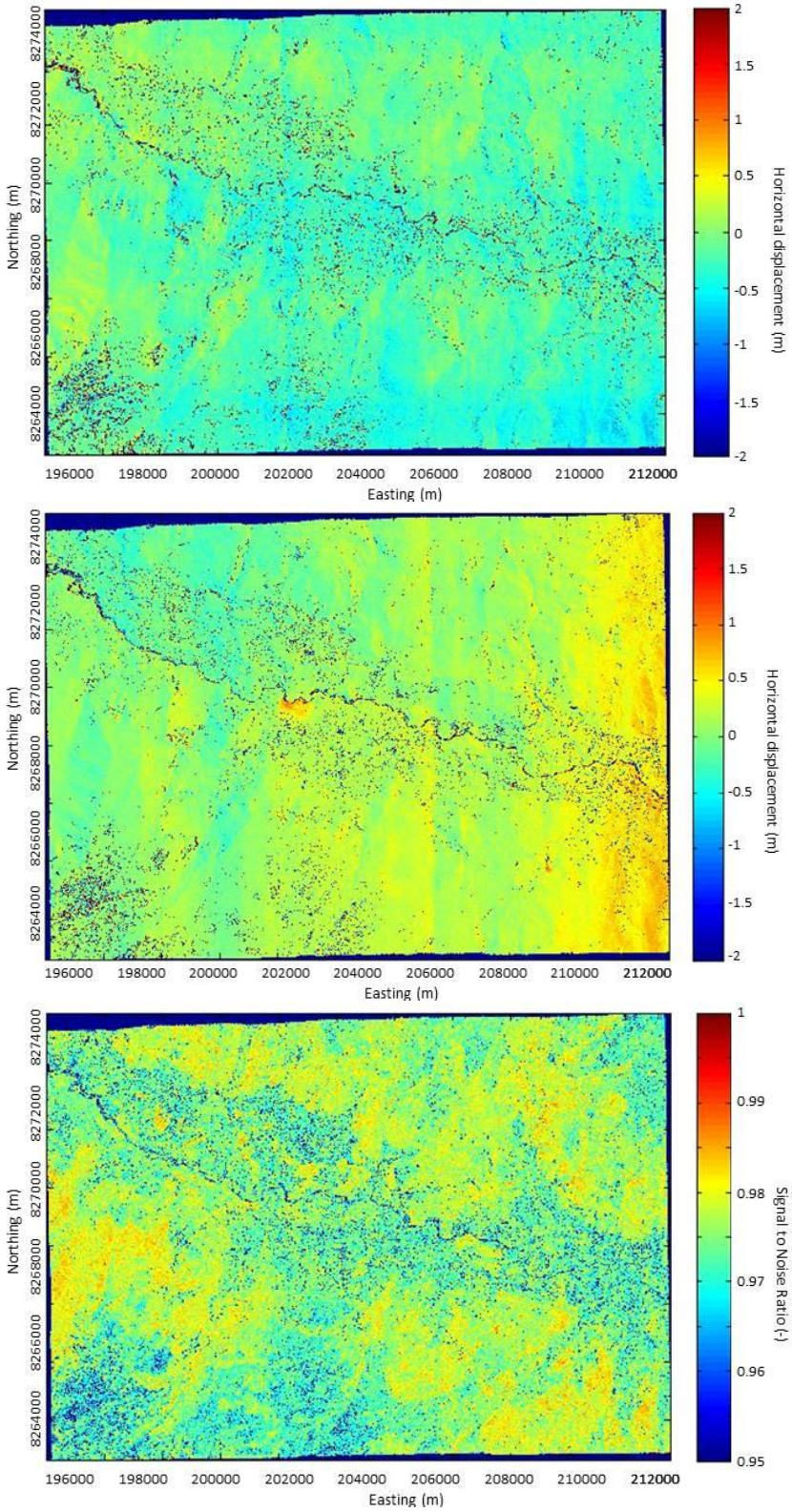

Figure A1.1: a) East-West displacement from March 2013 to April 2013, b) North-South displacement from March 2013 to April 2013, c) Signal to Noise Ratio of the displacement from March 2013 to April 2013.

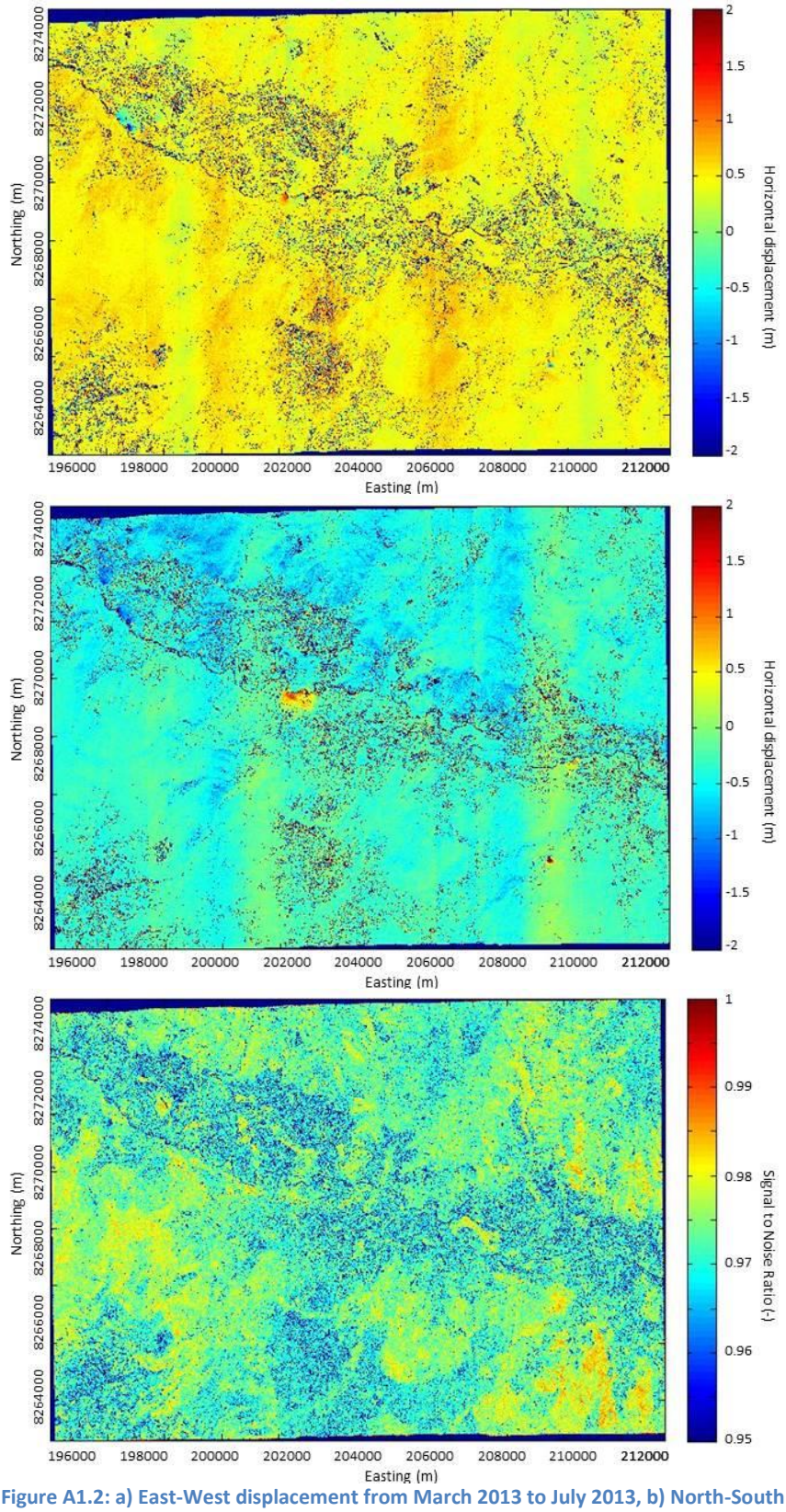

Figure A1.2: a) East-West displacement from March 2013 to July 2013, b) North-South displacement from March 2013 to July 2013, c) Signal to Noise Ratio of the displacement from March 2013 to July 2013.

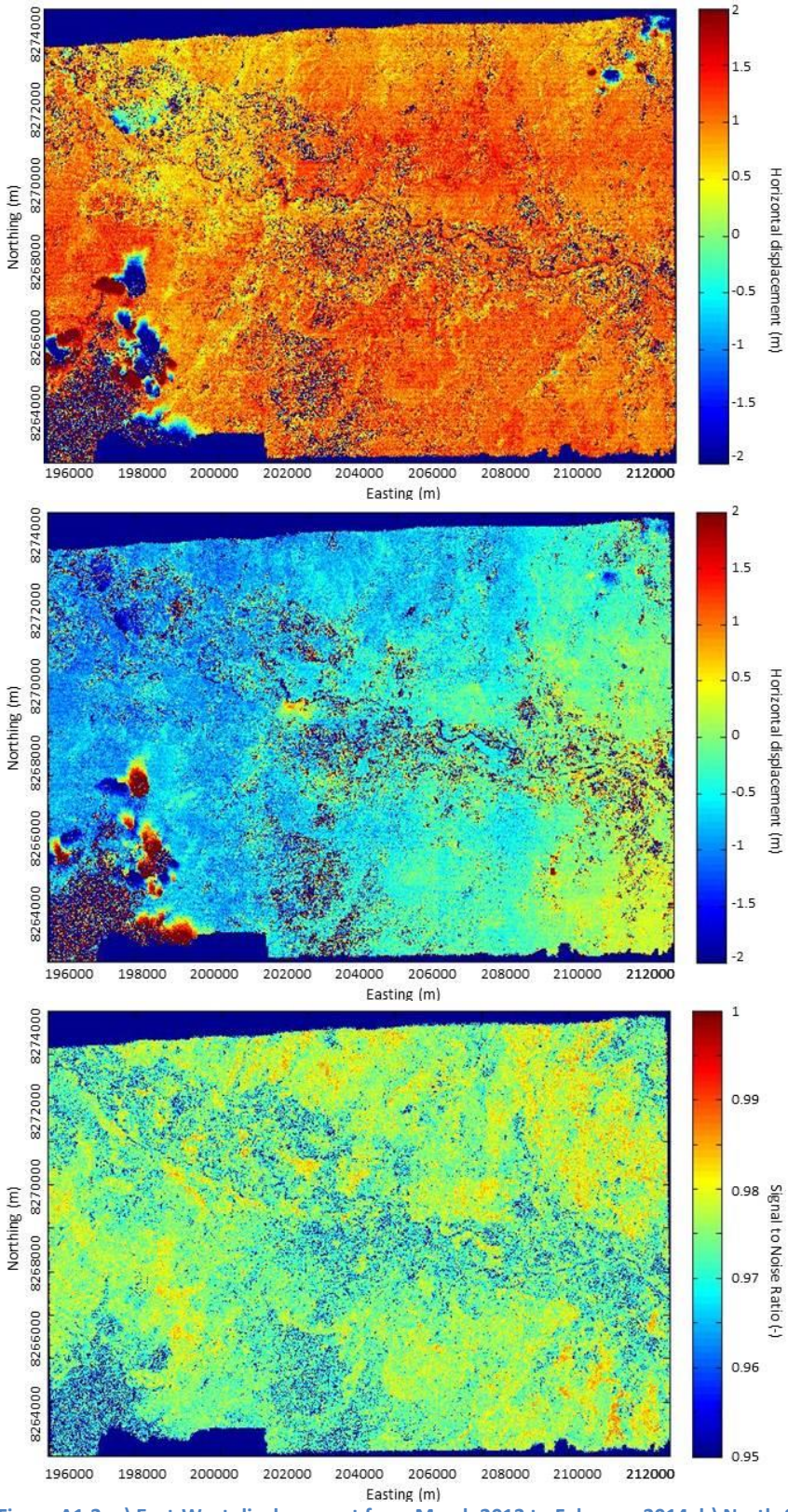

Figure A1.3: a) East-West displacement from March 2013 to February 2014, b) North-South displacement from March 2013 to February 2014, c) Signal to Noise Ratio of the displacement from March 2013 to February 2014.

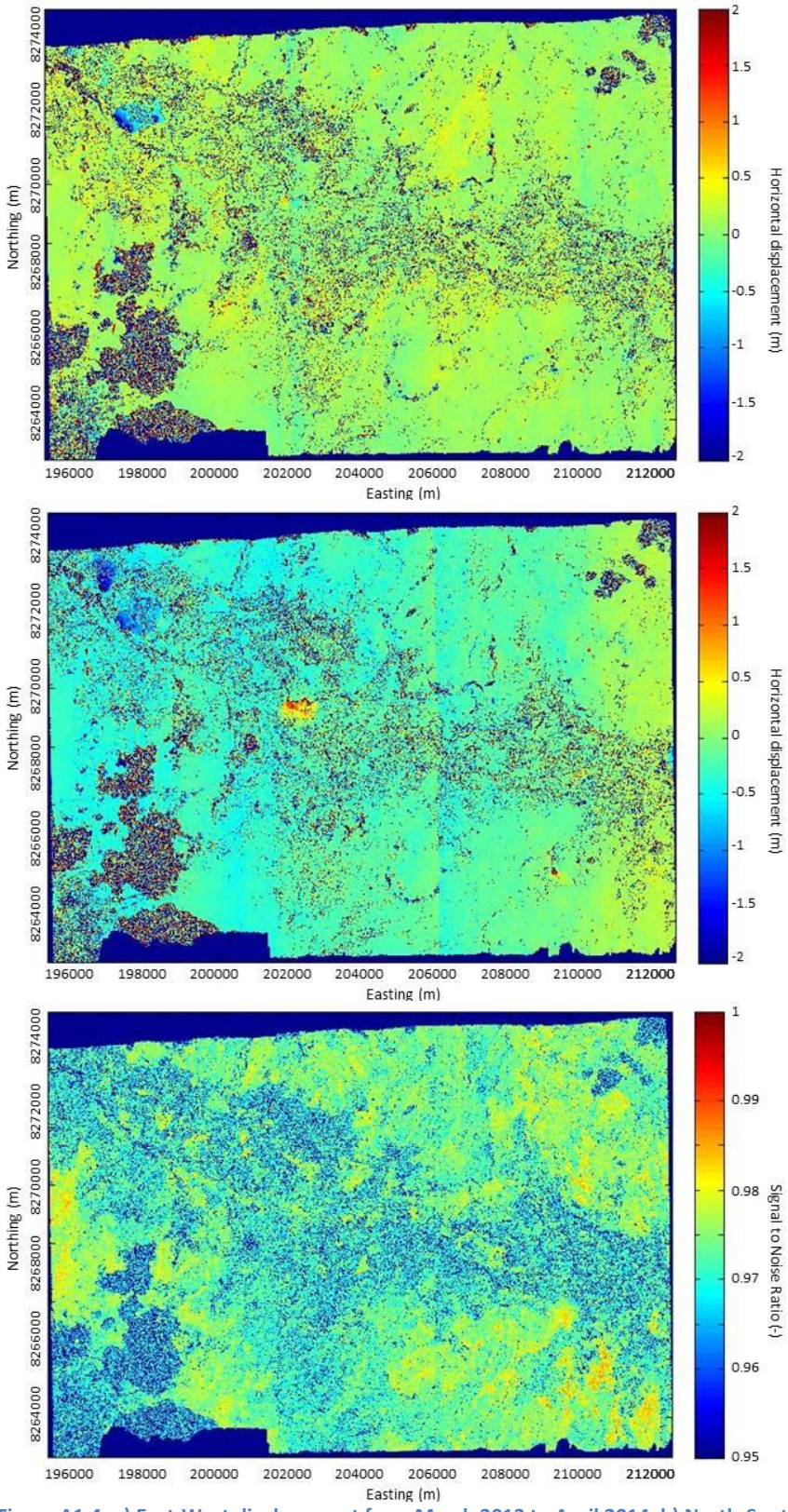

Figure A1.4: a) East-West displacement from March 2013 to April 2014, b) North-South displacement from March 2013 to April 2014, c) Signal to Noise Ratio of the displacement from March 2013 to April 2014.

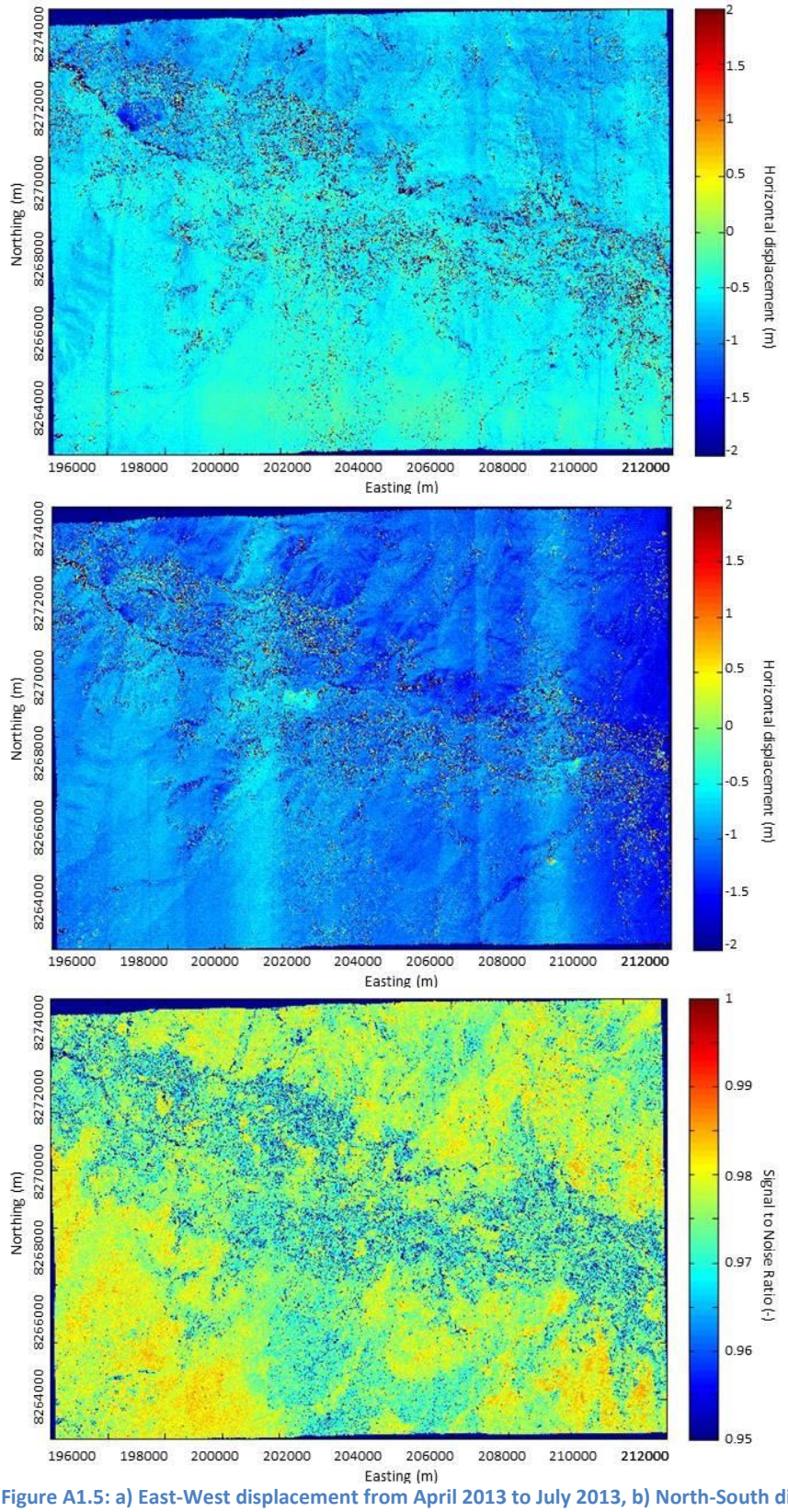

Figure A1.5: a) East-West displacement from April 2013 to July 2013, b) North-South displacement from April 2013 to July 2013, c) Signal to Noise Ratio of the displacement from April 2013 to July 2013.

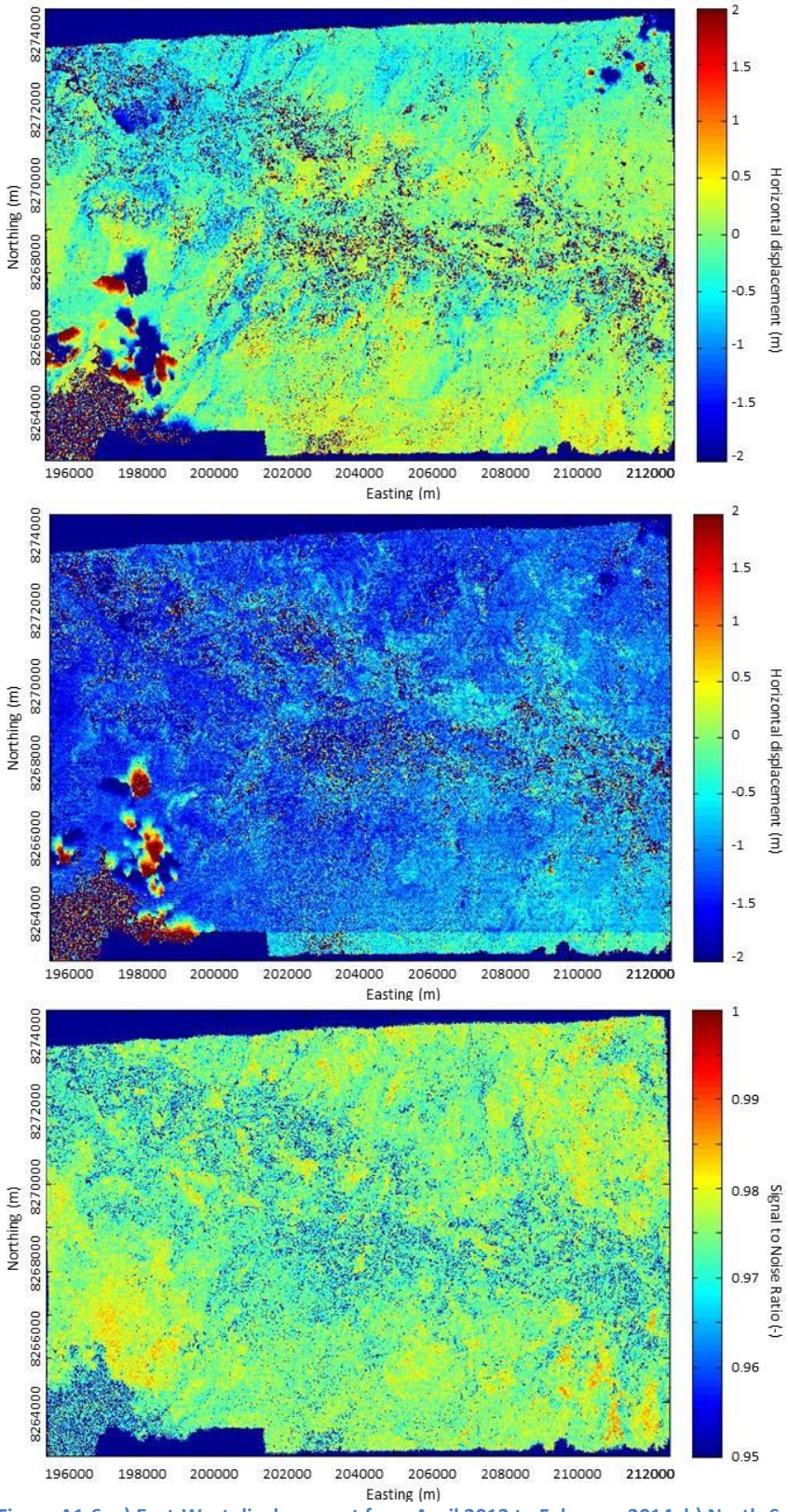

Figure A1.6: a) East-West displacement from April 2013 to February 2014, b) North-South displacement from April 2013 to February 2014, c) Signal to Noise Ratio of the displacement from April 2013 to February 2014.

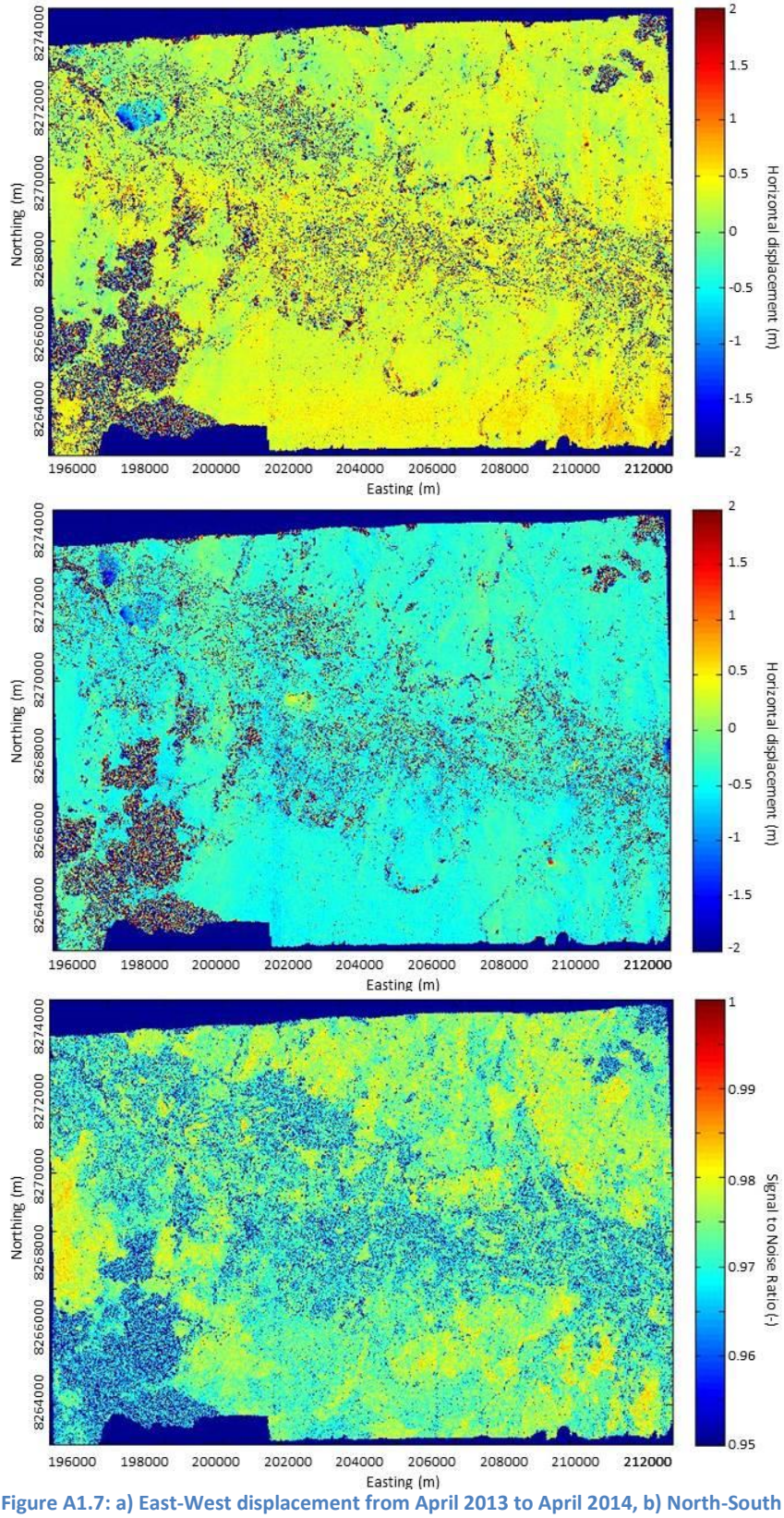

Figure A1.7: a) East-West displacement from April 2013 to April 2014, b) North-South displacement from April 2013 to April 2014, c) Signal to Noise Ratio of the displacement from April 2013 to April 2014.

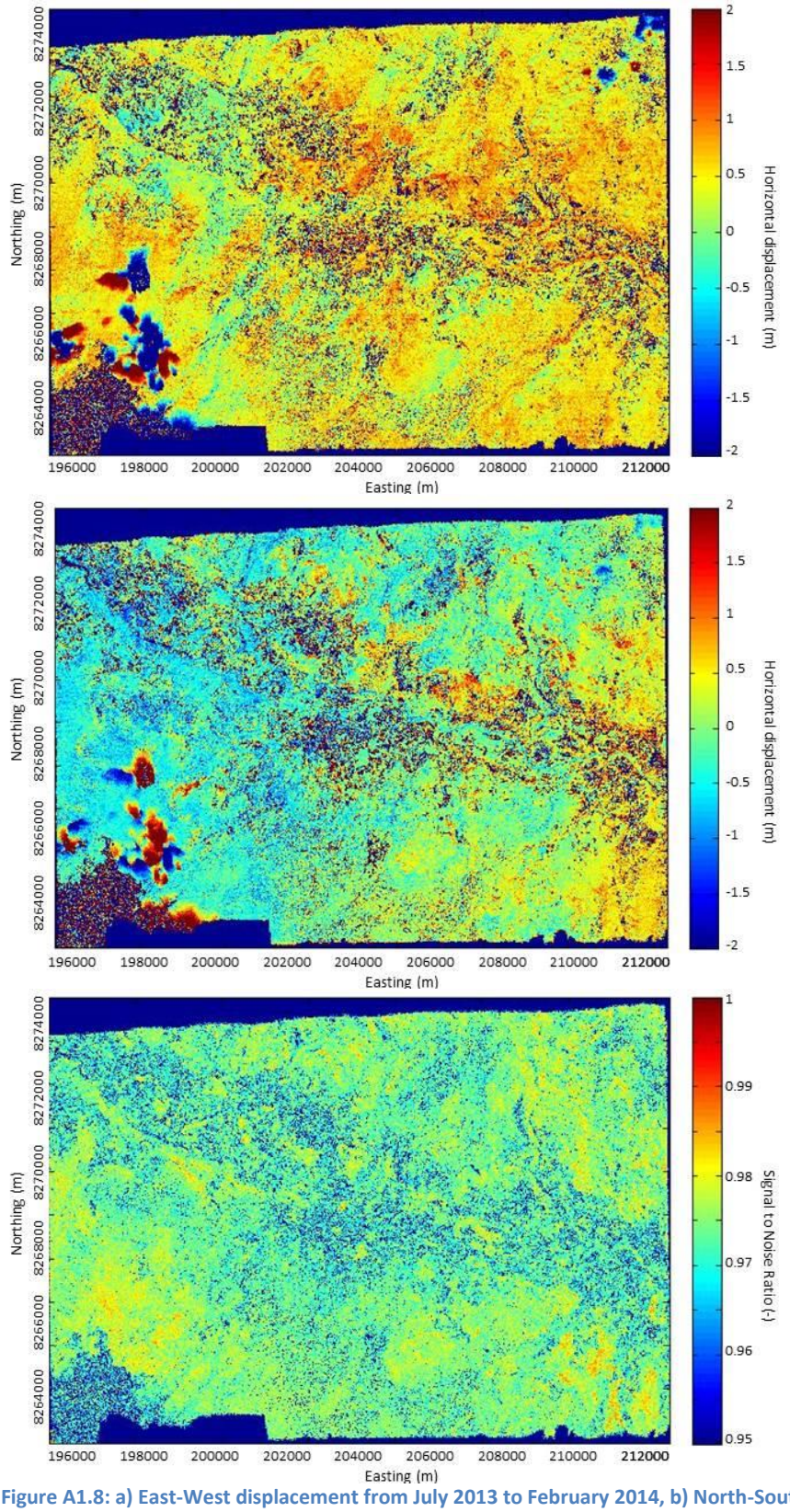

Figure A1.8: a) East-West displacement from July 2013 to February 2014, b) North-South displacement from July 2013 to February 2014, c) Signal to Noise Ratio of the displacement from July 2013 to February 2014.

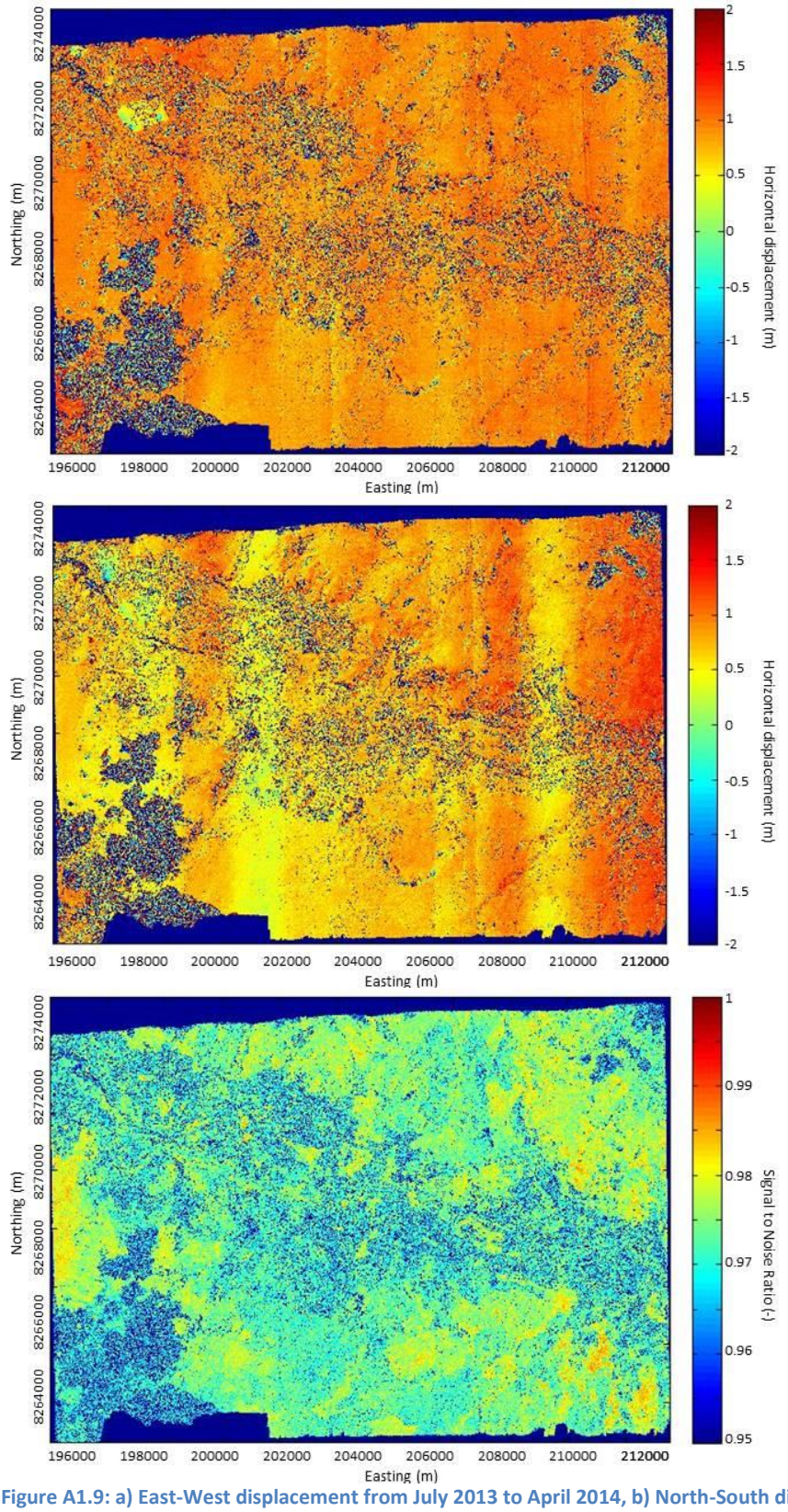

Figure A1.9: a) East-West displacement from July 2013 to April 2014, b) North-South displacement from July 2013 to April 2014, c) Signal to Noise Ratio of the displacement from July 2013 to April 2014.

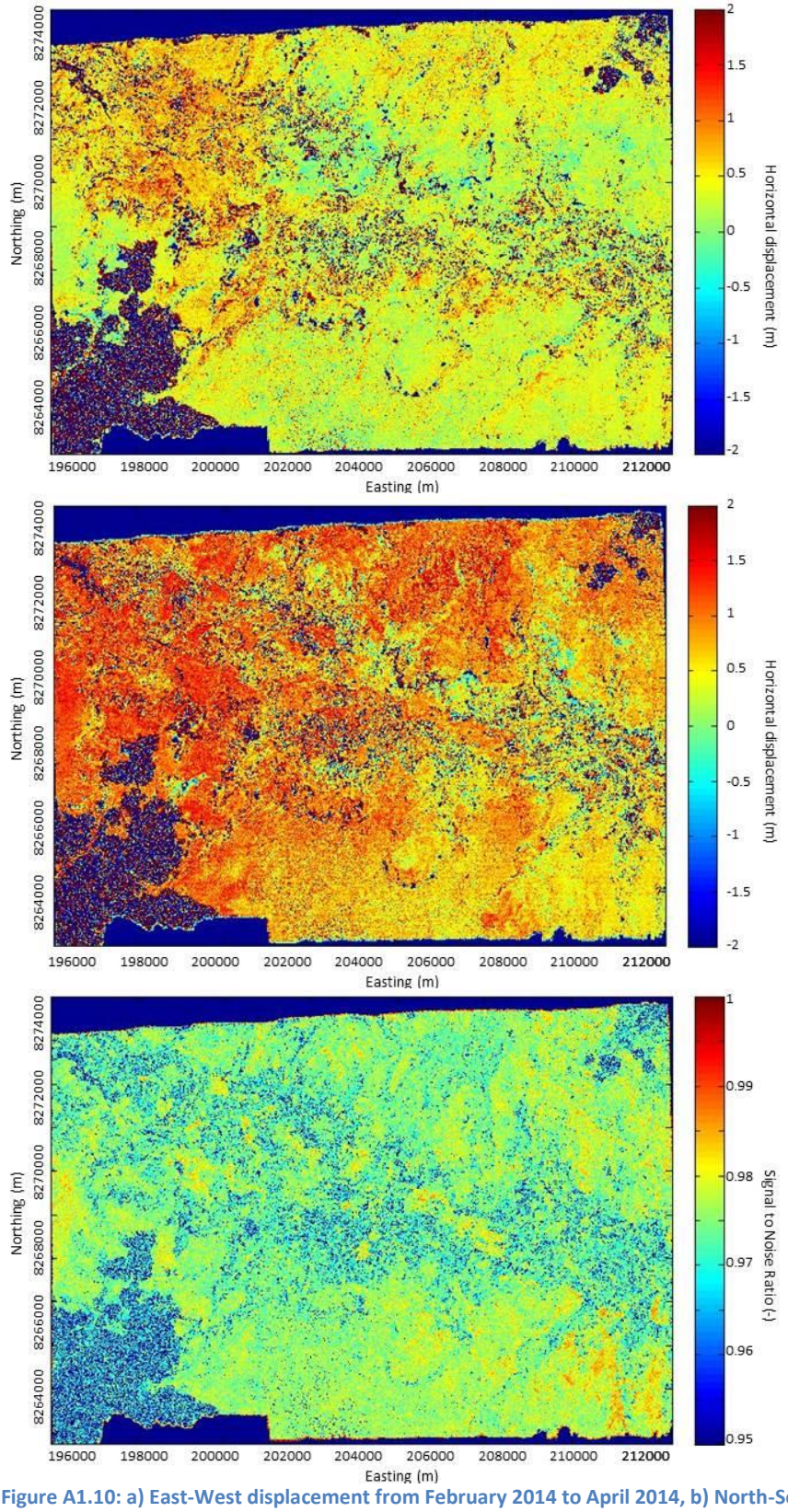

Figure A1.10: a) East-West displacement from February 2014 to April 2014, b) North-South displacement from February 2014 to April 2014, c) Signal to Noise Ratio of the displacement from February 2014 to April 2014.

Appendix 2. Corrections on displacement maps

Table A2: Median that is removed per landslide for each displacement map, in both an East-West direction and a North-South direction.

	E-W (m)	N-S (m)		E-W (m)	N-S (m)
March 2013 – April 2013			**March 2013 – July 2013**		
Achoma	-0.24	0.36	**Achoma**	0.40	-0.19
Huancane	-0.31	0.18	**Huancane**	0.38	-0.29
Maca	-0.29	0.17	**Maca**	0.42	-0.26
Madrigal	0.00	-0.07	**Madrigal**	0.39	-0.42
Rio Pina	-0.23	0.28	**Rio Pina**	0.45	-0.16
Sahuayto	0.02	0.03	**Sahuayto**	0.45	-0.55
Shutone	0.09	-0.24	**Shutone**	0.44	-0.52
March 2013 – February 2014			**March 2013 – April 2014**		
Achoma	0.91	0.05	**Achoma**	0.12	-0.08
Huancane	0.92	-0.56	**Huancane**	0.04	-0.18
Maca	0.92	-0.53	**Maca**	0.03	-0.18
Madrigal	0.54	-0.92	**Madrigal**	0.10	-0.41
Rio Pina	1.07	-0.32	**Rio Pina**	0.08	-0.08
Sahuayto	0.86	-0.87	**Sahuayto**	0.08	-0.41
Shutone	0.69	-0.83	**Shutone**	0.14	-0.54
April 2013 – July 2013			**April 2013 – February 2014**		
Achoma	-0.59	-1.08	**Achoma**	-0.15	-0.81
Huancane	-0.54	-1.04	**Huancane**	-0.06	-1.32
Maca	-0.48	-0.98	**Maca**	-0.07	-1.28
Madrigal	-0.81	-0.94	**Madrigal**	-0.69	-1.38
Rio Pina	-0.59	-0.98	**Rio Pina**	0.00	-1.05
Sahuayto	-0.81	-1.06	**Sahuayto**	-0.37	-1.33
Shutone	-0.90	-0.91	**Shutone**	-0.62	-1.12
April 2013 – April 2014			**July 2013 – February 2014**		
Achoma	0.31	-0.45	**Achoma**	0.52	0.26
Huancane	0.33	-0.39	**Huancane**	0.52	-0.29
Maca	0.32	-0.37	**Maca**	0.40	-0.23
Madrigal	0.08	-0.38	**Madrigal**	0.10	-0.50
Rio Pina	0.34	-0.37	**Rio Pina**	0.57	-0.13
Sahuayto	0.17	-0.38	**Sahuayto**	0.39	-0.31
Shutone	0.08	-0.27	**Shutone**	0.29	-0.16
July 2013 – April 2014			**February 2014 – April 2014**		
Achoma	0.95	0.70	**Achoma**	0.40	0.45
Huancane	0.91	0.71	**Huancane**	0.34	1.00
Maca	0.83	0.64	**Maca**	0.34	0.95
Madrigal	0.87	0.55	**Madrigal**	0.72	1.08
Rio Pina	0.98	0.74	**Rio Pina**	0.31	0.84
Sahuayto	0.98	0.76	**Sahuayto**	0.52	1.13
Shutone	0.98	0.61	**Shutone**	0.70	0.82

Appendix 3. Corrected and masked displacement maps for all landslides

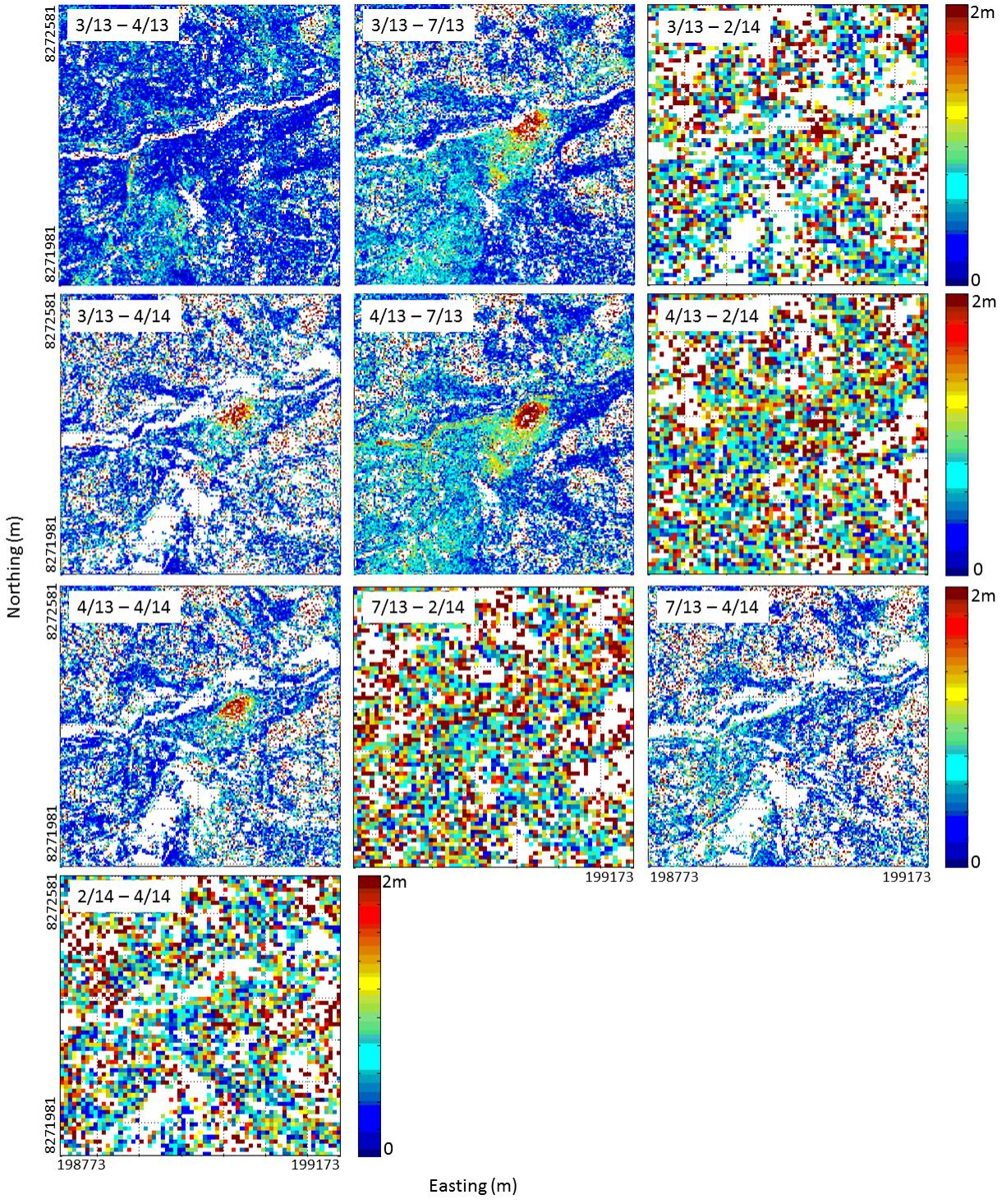

Figure A3.1: All horizontal displacement maps from the Achoma landslide.

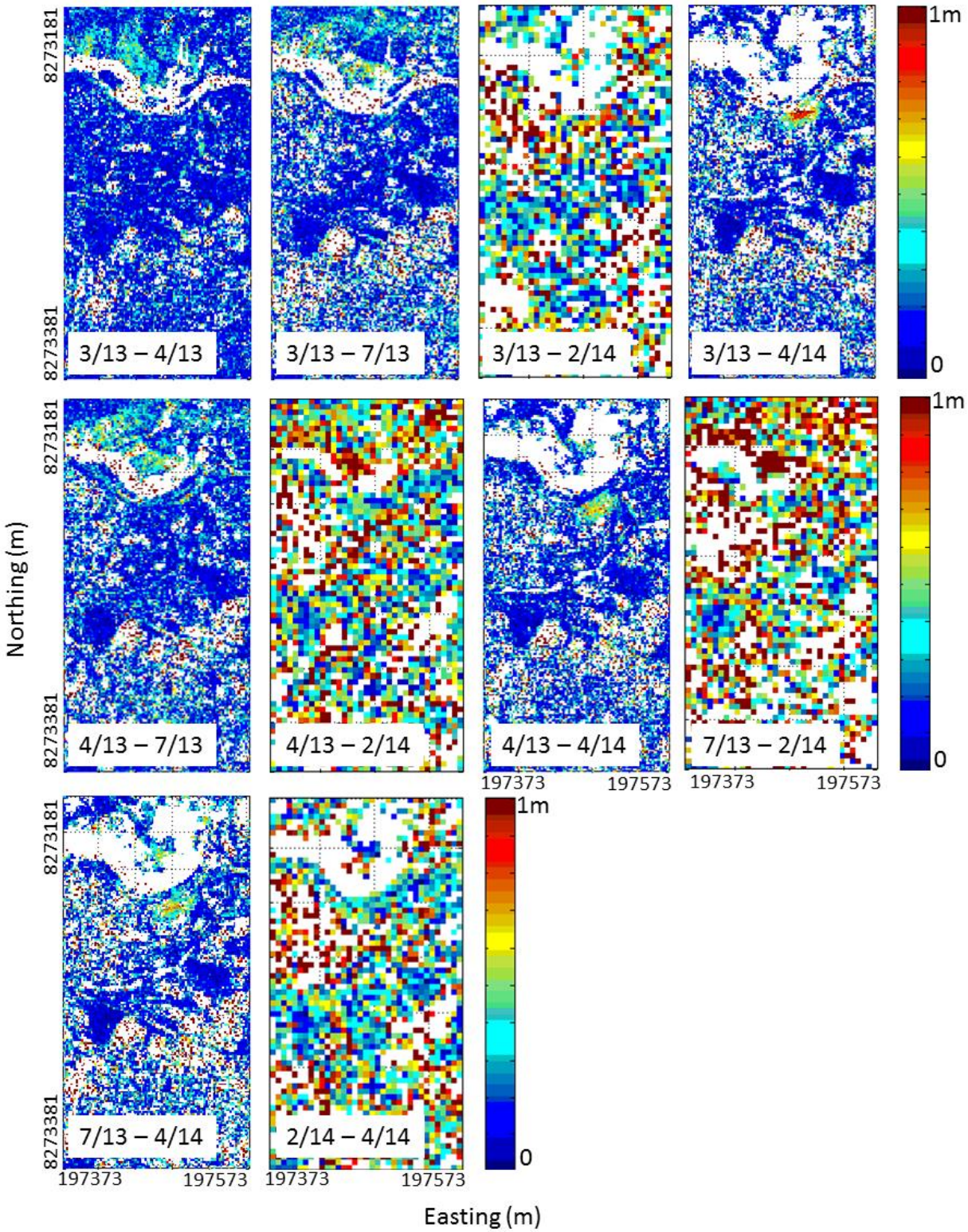

Figure A3.2: All horizontal displacement maps of the Huancane landslide.

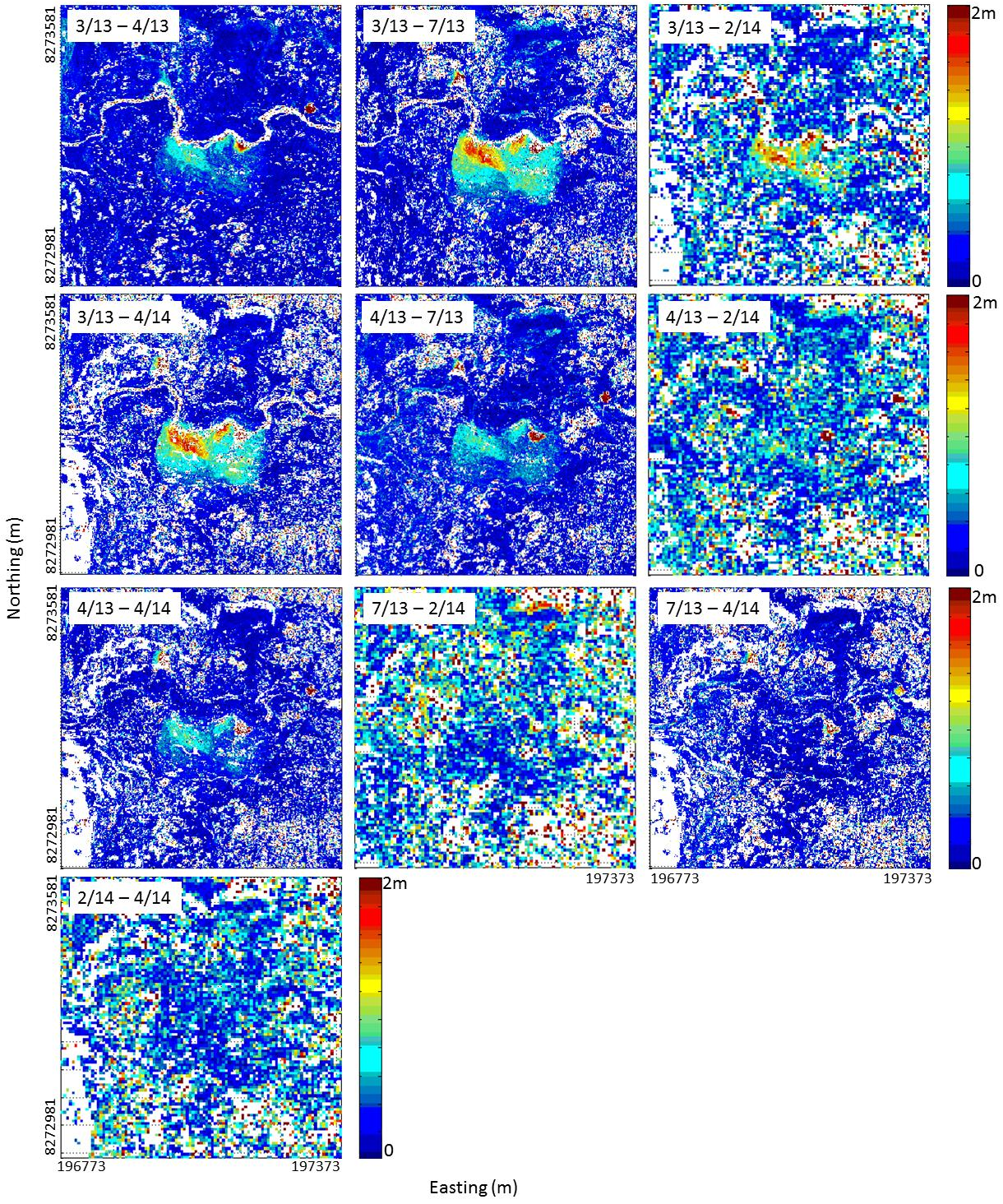

Figure A3.3: All horizontal displacement maps of the Maca landslide.

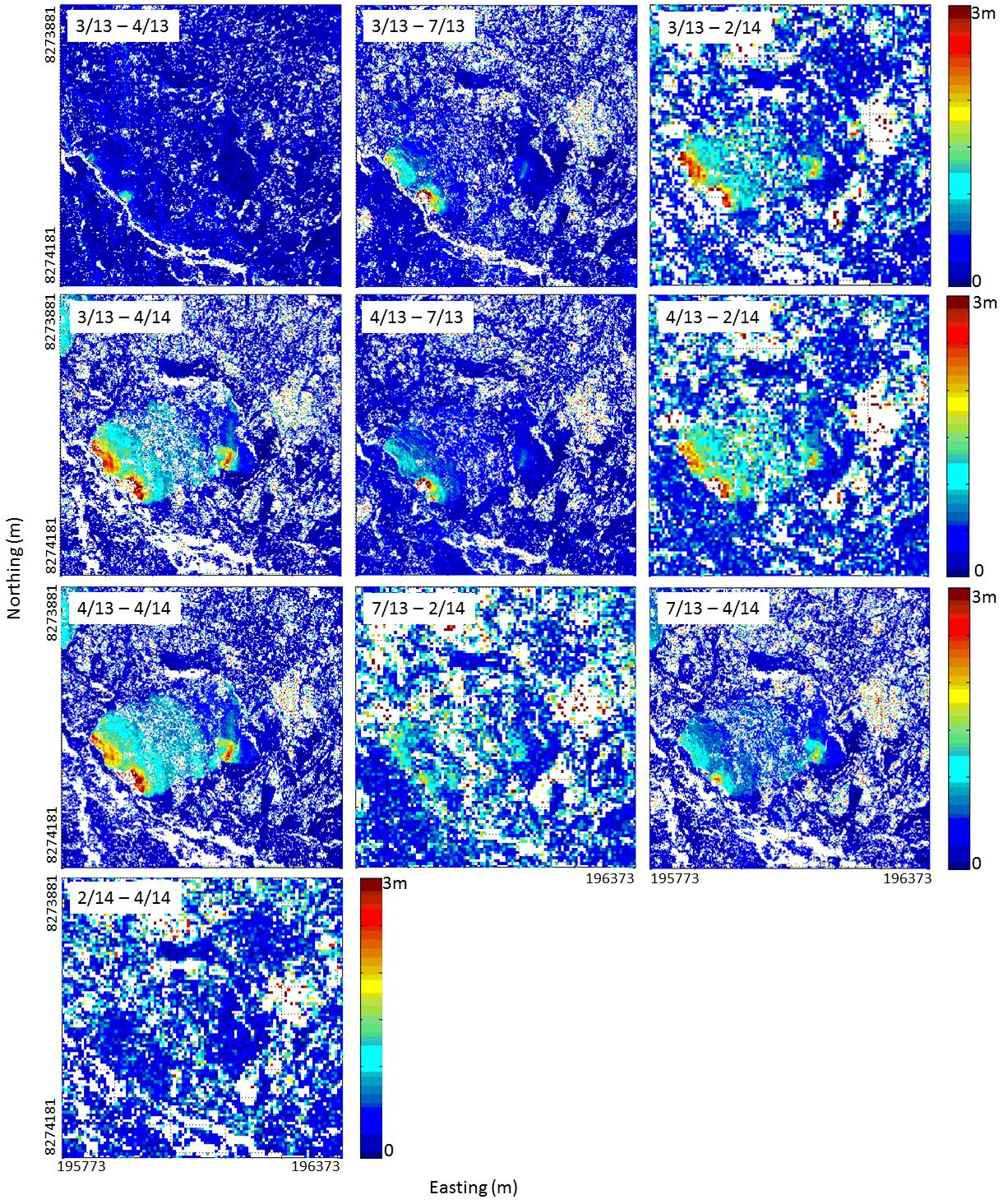

Figure A3.4: All horizontal displacement maps of the Madrigal landslide.

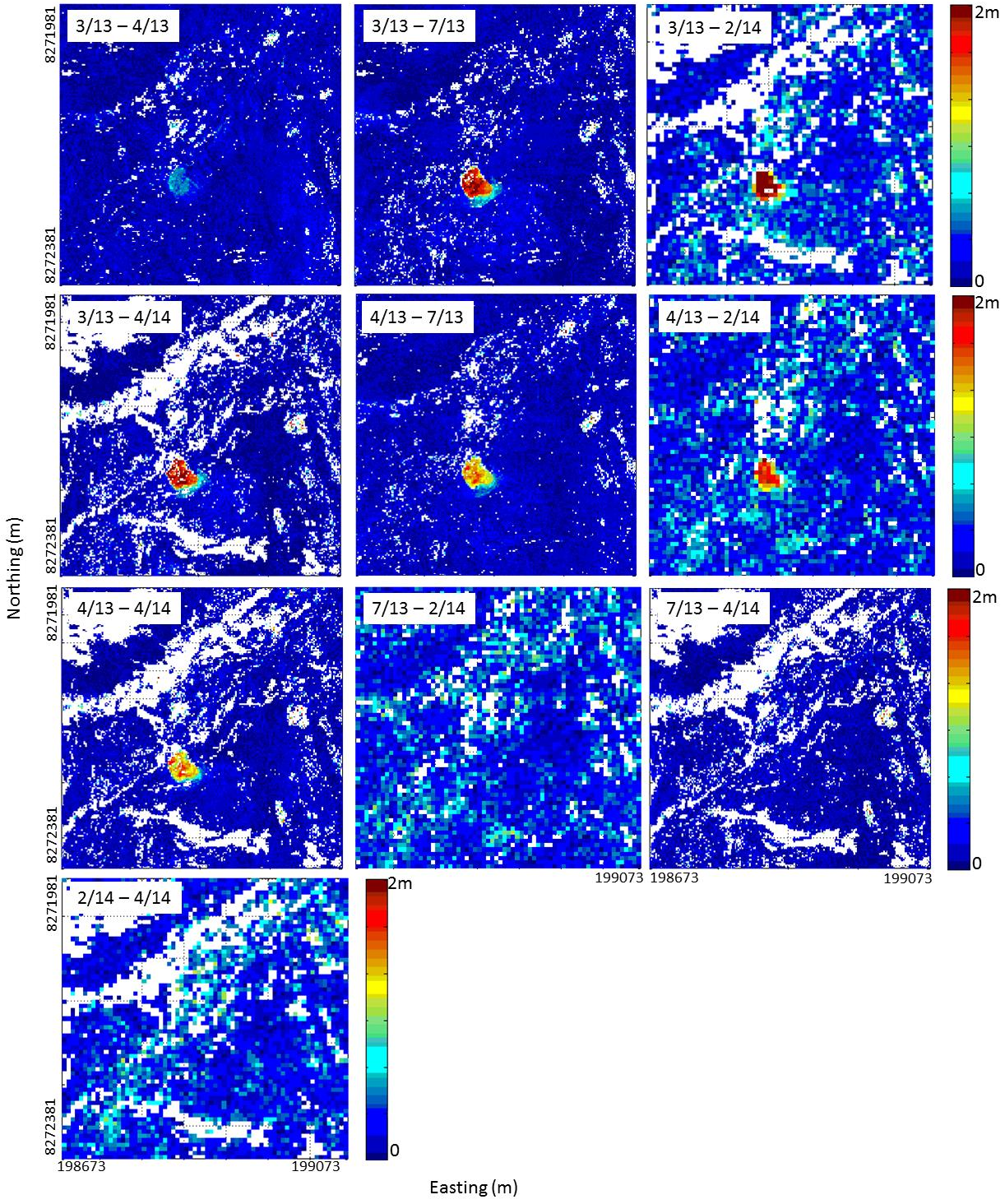

Figure A3.5: All horizontal displacement maps of the Rio Pina landslide.

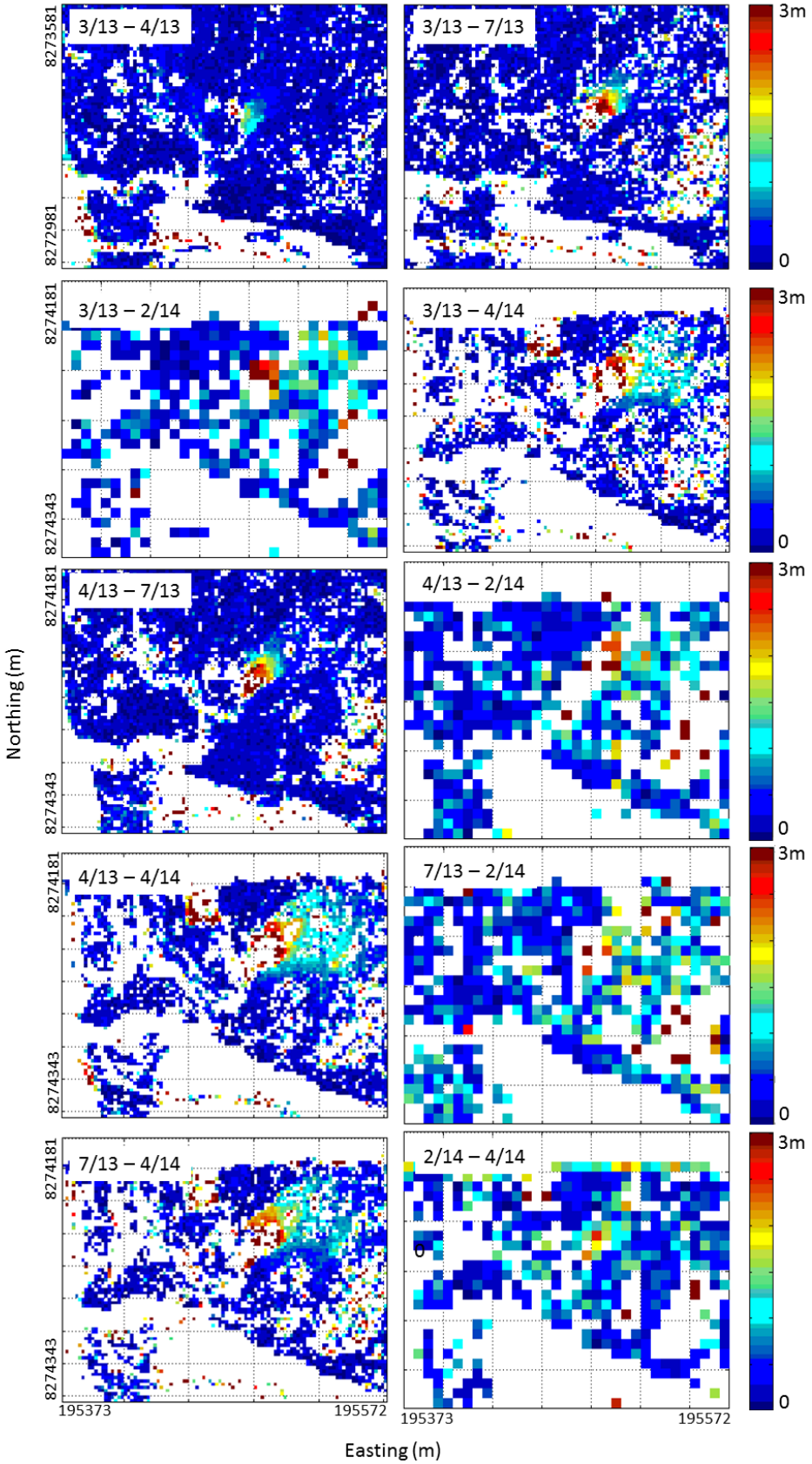

Figure A3.6: All horizontal displacement maps of the Sahuayto landslide.

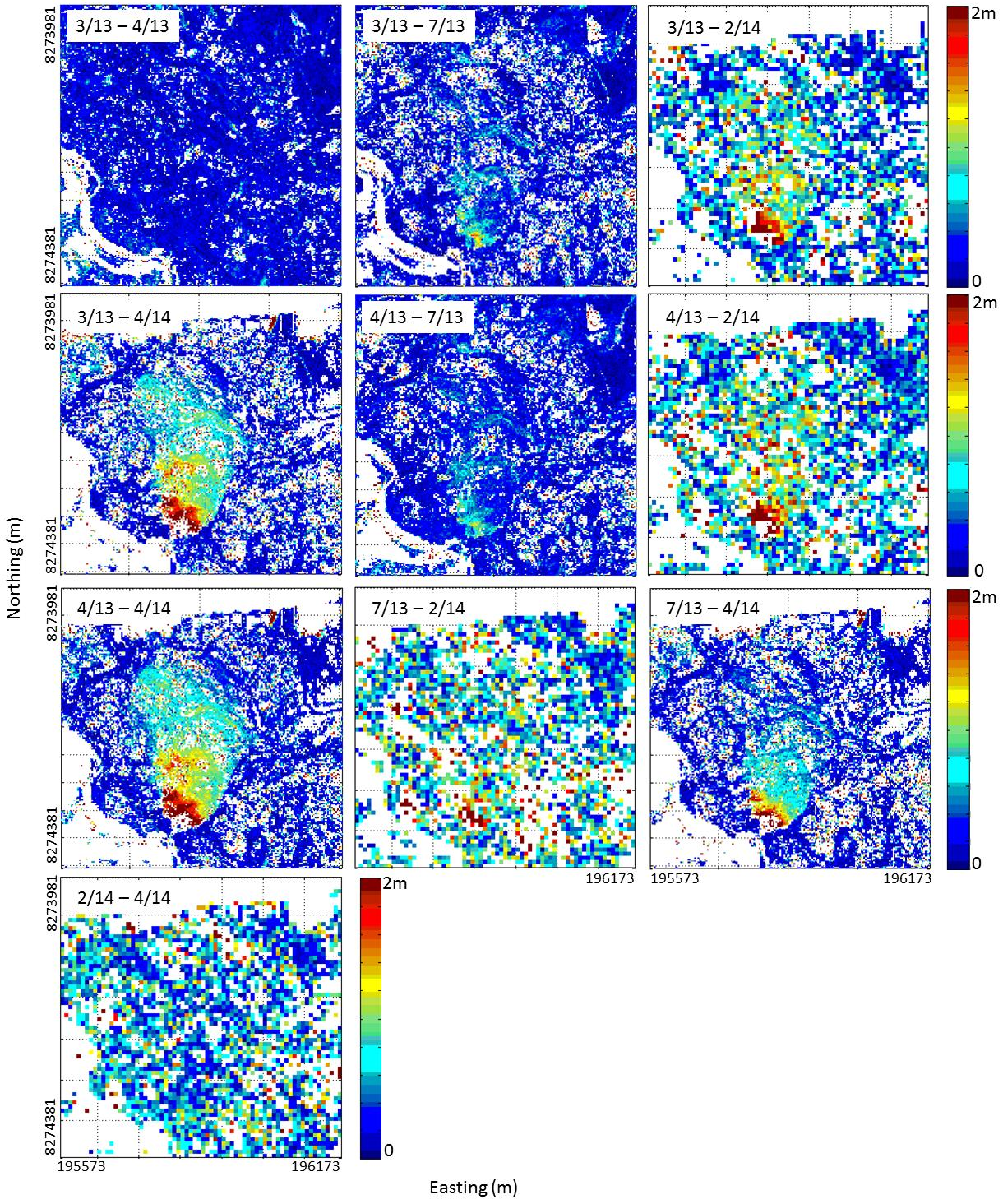

Figure A3.7: All horizontal displacement maps of the Shutone landslide.

Appendix 4. Statistics of displacements

Table A4.1: Statistics of the Achoma landslide for each time period.

Period (m/yy – m/yy)	Mean (m)	Median (m)	Standard deviation (m)	NMAD (m)
3/13 – 4/13	0.21	0.17	0.18	0.11
3/13 – 7/13	0.23	0.17	0.22	0.12
3/13 – 2/14	0.56	0.45	0.43	0.29
3/13 – 4/14	0.33	0.23	0.34	0.15
4/13 – 7/13	0.29	0.22	0.29	0.15
4/13 – 2/14	0.58	0.49	0.45	0.31
4/13 – 4/14	0.33	0.24	0.31	0.17
7/13 – 2/14	0.57	0.48	0.37	0.30
7/13 – 4/14	0.35	0.23	0.38	0.17
2/14 – 4/14	0.53	0.45	0.39	0.29

Table A4.2: Statistics of the Huancane landslide for each time period.

Period (m/yy – m/yy)	Mean (m)	Median (m)	Standard deviation (m)	NMAD (m)
3/13 – 4/13	0.18	0.14	0.19	0.09
3/13 – 7/13	0.26	0.17	0.29	0.13
3/13 – 2/14	0.54	0.43	0.44	0.29
3/13 – 4/14	0.26	0.17	0.29	0.13
4/13 – 7/13	0.25	0.18	0.29	0.12
4/13 – 2/14	0.56	0.49	0.38	0.33
4/13 – 4/14	0.26	0.18	0.29	0.13
7/13 – 2/14	0.68	0.55	0.54	0.37
7/13 – 4/14	0.33	0.20	0.43	0.15
2/14 – 4/14	0.57	0.47	0.41	0.32

Table A4.3: Statistics of the Maca landslide for each time period.

Period (m/yy – m/yy)	Mean (m)	Median (m)	Standard deviation (m)	NMAD (m)
3/13 – 4/13	0.21	0.16	0.27	0.10
3/13 – 7/13	0.34	0.21	0.45	0.14
3/13 – 2/14	0.78	0.56	0.96	0.39
3/13 – 4/14	0.41	0.22	0.58	0.16
4/13 – 7/13	0.30	0.20	0.43	0.13
4/13 – 2/14	0.76	0.61	0.69	0.43
4/13 – 4/14	0.38	0.21	0.55	0.16
7/13 – 2/14	0.97	0.75	1.01	0.54
7/13 – 4/14	0.48	0.25	0.68	0.18
2/14 – 4/14	0.76	0.58	0.79	0.40

Table A4.4: Statistics of the Madrigal landslide for each time period.

Period (m/yy – m/yy)	Mean (m)	Median (m)	Standard deviation (m)	NMAD (m)
3/13 – 4/13	0.21	0.17	0.19	0.11
3/13 – 7/13	0.31	0.20	0.38	0.15
3/13 – 2/14	0.56	0.40	0.69	0.29
3/13 – 4/14	0.33	0.20	0.42	0.15
4/13 – 7/13	0.31	0.20	0.41	0.14
4/13 – 2/14	0.62	0.45	0.68	0.34
4/13 – 4/14	0.31	0.19	0.39	0.13
7/13 – 2/14	0.68	0.51	0.67	0.38
7/13 – 4/14	0.41	0.26	0.50	0.18
2/14 – 4/14	0.56	0.42	0.50	0.29

Table A4.5: Statistics of the Rio Pina landslide for each time period.

Period (m/yy – m/yy)	Mean (m)	Median (m)	Standard deviation (m)	NMAD (m)
3/13 – 4/13	0.11	0.10	0.07	0.06
3/13 – 7/13	0.11	0.10	0.07	0.07
3/13 – 2/14	0.31	0.27	0.18	0.16
3/13 – 4/14	0.10	0.08	0.06	0.05
4/13 – 7/13	0.13	0.11	0.07	0.07
4/13 – 2/14	0.40	0.36	0.24	0.23
4/13 – 4/14	0.11	0.10	0.07	0.06
7/13 – 2/14	0.42	0.38	0.25	0.24
7/13 – 4/14	0.12	0.10	0.07	0.06
2/14 – 4/14	0.33	0.32	0.17	0.18

Table A4.6: Statistics of the Sahuayto landslide for each time period.

Period (m/yy – m/yy)	Mean (m)	Median (m)	Standard deviation (m)	NMAD (m)
3/13 – 4/13	0.28	0.22	0.26	0.15
3/13 – 7/13	0.23	0.17	0.27	0.11
3/13 – 2/14	0.40	0.35	0.27	0.22
3/13 – 4/14	0.57	0.25	0.95	0.18
4/13 – 7/13	0.26	0.19	0.36	0.12
4/13 – 2/14	0.46	0.38	0.29	0.25
4/13 – 4/14	0.50	0.26	0.85	0.18
7/13 – 2/14	0.55	0.46	0.58	0.28
7/13 – 4/14	0.52	0.21	0.89	0.16
2/14 – 4/14	0.65	0.44	0.69	0.39

Table A4.7: Statistics of the Shutone landslide for each time period.

Period (m/yy – m/yy)	Mean (m)	Median (m)	Standard deviation (m)	NMAD (m)
3/13 – 4/13	0.19	0.16	0.15	0.10
3/13 – 7/13	0.28	0.20	0.31	0.15
3/13 – 2/14	0.51	0.42	0.41	0.28
3/13 – 4/14	0.31	0.20	0.37	0.15
4/13 – 7/13	0.27	0.20	0.29	0.14
4/13 – 2/14	0.56	0.52	0.35	0.31
4/13 – 4/14	0.29	0.19	0.33	0.14
7/13 – 2/14	0.68	0.58	0.47	0.35
7/13 – 4/14	0.33	0.20	0.43	0.15
2/14 – 4/14	0.61	0.50	0.43	0.36